이학박사 학위논문

Synthesis and Catalytic/Optical Properties of Dealloying-Based Porous Nanoparticle and Plasmonic Nanogap Nanoparticle

탈합금화 반응 기반의 다공성 나노입자 및 플라즈모닉 나노갭 나노입자 합성과 이의 촉매/광학 특성

2017 년 8 월

서울대학교 대학원

화학부 무기화학

김 민 호

Abstract

Synthesis and Catalytic/Optical Properties of Dealloying-Based Porous Nanoparticle and Plasmonic Nanogap Nanoparticle

Minho Kim

Department of Chemistry

The Graduate School

Seoul National University

Nanoporous metallic structure, which are composed by a three-dimensional open-cell network of interconnected ligaments on the order of 10 to 100 nm, are very promising materials in various applications such as catalysis and sensing owing to their high surface-to-volume ratio and excellent surface reactivity. Especially, nanoporous gold (Au) structures have been attracted much attention for practical applications due to the good chemical/biological stability, unique mechanical rigidity, electrical conductivity, and high corrosion resistance. Previously, the porous materials have been made by casting into the interstices of microphase-separated block copolymers, colloidal crystal, self-assembled surfactants, and biologically formed porous skeletal structures. Recently, with the advent of

nanotechnology, a dealloying which is defined as selective dissolving of the less stable metal elements from alloy system has been used as a processing tool to fabricate the well-controllable nanoporous metallic structures. By many efforts in theoretical and experimental studies, the nanoporous metallic structures have been well-defined and precisely controlled, and their structure-dependent properties have also been investigated a lot.

For recent decades, various studies and techniques have been reported and developed for fabricating well-controlled nanoporous metallic structures, however, most of nanoporous metallic structures are mainly focused on the three- or two-dimensional structures which have limitations for specific applications such as nanomedicine, drug delivery, and labeling in biosensing. In contrast, the nanoporous metallic nanoparticles are most promising materials for biomedical and sensing applications due to their large surface which is capable for loading of drug and targeting molecule, and their tunable and unique SPR properties for enlarging the sensing signal. Furthermore, those nanoparticles are relatively easy and fast to synthesize and is also highly capable for mass production, resulting in in practical applications. However, the precise and reproducible synthesis of nanoporous metallic nanoparticle (especially in Au) is quite difficult and have rarely been reported because the fabrication of uniform alloy nanoparticles with suitable composition and size is still quite challenging due to the different chemical properties of each metal elements. Although some recent studies cover the fabrication of nanoporous metallic nanoparticle, those synthesis methods need complex route such as annealing process, and resulting products are usually not uniform in size, which cannot provide reproducibility and reliability in sensing application. Therefore, it is still highly challenging to precisely and reproducibly synthesize the uniform and pore/ligament size-controllable nanoporous metallic nanoparticles for utilizing them to a wide range of applications.

In this thesis, dealloying-based synthetic strategies to fabricate highly porous nanoparticles and plasmonic interior-nanogap nanoparticles are presented. These facile and straightforward synthetic strategies allow us to manipulate the nanoporosity and interior nanogap which highly affect to catalytic performance and optical signal enhancement. By introducing co-reduction chemistry and by adjusting the Ag to Au ratio, the atomic distribution of Au can be highly controlled in Au-Ag alloy shells, resulting in nanoporous Au nanoparticles with different porosity *via* dealloying process. Using the Au core/porous shell nanoparticles which contain networked thin ligaments, surface defects with well-controlled nanoporosity, the porosity-dependent catalytic activity is investigated. When Ag to Au ratio is further adjusted during co-reduction chemistry, Au-Ag dealloyed nanogap nanoparticles with interior nanogap can be formed despite of the absence of an interlayer, such as DNA, silica ore polymer layer *via* dealloying process. With dealloyed nanogap nanoparticles of which size of well-defined interior nanogap is as smaller as ~2 nm, quantitative studies for surface-enhanced Raman scattering (SERS) are investigated. In addition, estimation of enhancement factor and polarization-dependent SERS property are also carried out in single-particle-level. Finally, highly quantitative DNA detection and highly sensitive/selective target cell imaging is presented using the bio-functionalized interior-nanogap nanoparticles. Understanding and utilizing the relationships between dealloying-based structural changes and catalytic/optical properties in highly controlled nanostructures can give advanced insight in designing and synthesizing the desired nanostructures for the targeted applications.

The chapter 1 provides an overview and perspective of recent advances in the use of dealloying-based nanoporous Au nanostructures for various applications. Next, the mechanism of evolution of nanoporosity from Au-Ag alloy system during dealloying is introduced. Because the morphologies (*e.g.*, size or distribution of pore/ligament) of nanoporous metals obtained from dealloying

process are highly influenced by the dealloying condition, such as alloy composition, dealloying time, temperature, kinds of solutions, and intrinsic property of noble metals, the effects of dealloying conditions in adjusting structure of dealloyed nanoporous metals are also discussed. Finally, various examples of nanoporous Au structures produced by well-controlled dealloying process and their representative applications are introduced and discussed.

In chapter 2, a facile and straightforward synthetic strategy for controlling and forming Au core/porous shell nanoparticles (CPS NPs) by a selective dealloying (Ag-etching process) process of Au/Au–Ag core/alloy shell NPs (CAS NPs) is presented. The shell of CPS NPs contained networked thin ligaments, catalytically-active surface defects and ultra-high porosity throughout the shell. Using the robust CPS NPs, the porosity-dependent catalytic activity with a well-known chemistry [the reduction of 4-nitrophenol (4-NP) by sodium borohydride ($NaBH_4$) in this case] was investigated. The CPS NPs exhibited a very short induction time, high conversion rate constant, low activation energy and high turnover frequency due to their catalytically active porous shells containing networked thin ligaments, surface defects, ultra-high porosity. The CPS NPs could further enhance the catalytic reactivity due to their photothermal activation. In addition, the highly porous CPS NPs showed much better catalytic performance in comparison with galvanic replacement-based Au core/hollow shell nanoparticles (CHS NPs).

In chapter 3, a highly controllable dealloying chemistry for synthesizing Au-Ag dealloyed nanogap nanoparticles (DAG NPs) with a dealloyed interior nanogap is presented. The interior nanogap was formed as small as ~2 nm and controlled without the need for an interlayer, such as DNA, silica or polymer layer, in the gap in a high yield (~95 %). Owing to the strong electromagnetic field enhancement in the nanogap, DAG NPs facilitate generation of strong, tunable, and reproducible SERS signals with narrowly distributed enhancement factors. In addition, the SERS signal intensity from DAG NPs linearly increased as particle

concentration increased, allowing for highly reliable, quantitative SERS. Importantly, single-particle laser polarization study suggests that the SERS signals from a DAG NP are polarization-independent, which is critical in getting reproducible signals from individual particles. Finally, the bio-functionalized DAG NPs showed that they can be used as ultrasensitive, highly quantitative DNA detection probes and targeted cell imaging probes with high sensitivity and selectivity.

Key words: Dealloying, Nanoporous Gold Structure, Catalytic Reaction, Plasmonic Interior-Nanogap structure, Surface-Enhanced Raman Scattering (SERS), DNA Detection, Cell Imaging.

Student Number: 2011-30099

Contents

List of Figures

Chapter 1

Chapter 2

Chapter 3

List of Tables

Chapter 2

Chapter 3

Chapter 1

Dealloying-Based Fabrications of Nanoporous Gold Nanostructures and Their Applications

1.1. Introduction

In human history, an "alloying" played a very important role in opening the *'Bronze Age'*, and a continuous progress of alloying technology is still leading the development of mankind to this day. Also, the concept of "dealloying", which is defined as selective dissolving of the less stable metal elements from alloys, has also been well known for more than a century in the context of corrosion. In the Civil War era, however, it has been considered as a materials phenomenon to be avoided because the dezincification of brass was identified as a major failure mode.[1] Thus, dealloying remained a major corrosion problem. With the advent of "nano", however, the dealloying has much attention as a processing tool in the recent, which forms porous materials, such as nanoporous Cu, Pt, Pd, Ag, Au, *etc*.[2-6] Furthermore, the dealloyed nanoporous metallic structures, which are composed by a three-dimensional (3D) open-cell network of interconnected ligaments on the order of 10 to 100 nm (Figure 1.1), have been widely applied in the field of catalysis, sensing, optics, *etc*. due to their high surface-to-volume ratio, surface reactivity, chemical/biological stability, mechanical rigidity, electrical conductivity, and high corrosion resistance.[7-10]

Previously, the porous materials were made by casting into the interstices of microphase-separated block copolymers, colloidal crystal, self-assembled surfactants, and biologically formed porous skeletal structures.[11-14] All of these techniques can control the pore size and microstructure of the desired porous materials; however, the dynamic control of the length scale is virtually impossible. Moreover, the methods for the fabrication of metallic nanostructure are very few and are also challenge. In this respect, dealloying, which can produce a 3D porous material with bicontinuous ligament-pore structure, has attracted enormous interests and still being intensively studied.

Since 1926, the porous metallic materials obtained from the dealloying of Al-based alloys, named as RANEY® metals, have been started to use as catalysts.[15] These catalysts are widely applied in industrial processes (*e.g.*, hydrogenation reactions); however, the exact mechanism of evolution of porosity during dealloying, and the structure-related properties of the formed microstructures were less studied and understood.[16] To understand the fundamental aspects of alloy corrosion, in the 1960s, the rigorous mechanistic studies of the electrochemical dealloying (corrosion) behaviors of gold-based alloys were investigated by Pickering and Swann.[17] For the first time, they used transmission electron microscopy (TEM) to observe the resulting nanoporous structures with a feature size of ~10 nm.[17,18] By using electron microscopy, in the late of 1970s, Forty observed the detailed look of the freestanding nanoporous Au structure, which had a pore size of approximately 20 nm and was obtained from the dealloyed Au-Ag alloy in HNO_3.[2] Following this, the specific studies of the dealloying process of Au-Ag alloys were continuously investigated in the 1980s and 1990s.[19,20] With the help of modern technology and advanced techniques (*e.g.*, electrochemical scanning tunneling microscopy), two key parameters associated with dealloying were suggested: (1) "parting limit" and (2) "critical potential". The parting limit is defined as the proportion of the noble metal in an alloy above which dealloying cannot occur, which means that only alloys within a certain range of compositions can be dealloyed.[21] In case of Au-Ag alloy system, the dealloying does not occur when the composition of Ag is lower than 55 at%. When the composition of Ag within the Au-Ag alloys is lower than the parting limit, Ag atoms will not be dissolved but be passivated by Au atoms due to the higher coordination by Au atoms.[21] The critical potential is defined as a voltage threshold above which the dissolution current rises dramatically, resulting in dealloying reaction.[22-24] The critical potential is dependent on the electrolyte, additives (*e.g.*, halides), and initial composition of the alloy precursor.[22,24,25] In addition, the

advanced study of the pore formation process during dealloying was performed by using *in situ* neutron scattering.[26] In 2001, Erlebacher and co-workers successfully suggested an atomistic model which illustrated the evolution of nanoporosity during dealloying of the Au-Ag alloy by using a kinetic Monte Carlo model.[27] This pioneer work is believed as a breakthrough in the field of dealloying reaction because it could act as a bridge between the traditional electrochemistry efforts (*e.g.*, surface gilding and protection) and the most advanced nanotechnology (*e.g.*, fuel cell and catalysis). Subsequently, a series of important studies, which focused on fabricating various nanoporous metallic structures and their potential applications in sensing, catalysis, plasmonic, *etc*., have been steadily conducted until these days.[28-31]

In this chapter, mechanism of formation of nanoporosity during dealloying reaction, effects of dealloying conditions in adjusting size of pore/ligament structures, fabrications and applications of nanoporous Au nanostructures are introduced and discussed.

1.2. Evolution of Nanoporosity during Dealloying

Although much effort have been tried to understand the dealloying process, the precise mechanisms which can explain the evolution of nanoporosity during dealloying is unclear. In 2001, Erlebacher and co-workers proposed a kinetic Monte Carlo model to simulate the dealloying process of Au-Ag alloys, which was able to reproduce all relevant experimental trends characteristic of dealloying, both morphological and kinetic.[27] This model is composed with three competing processes: (1) the dissolution of the less noble element (Ag), (2) the surface diffusion of the noble element (Au), and (3) the capillary-driven surface relaxation (coarsening).[27,32] By considering a (111) facet of an Au-Ag alloy as an initial condition, the evolution of nanoporosity during dealloying can be described in the following way.

When the Au-Ag alloys are immersed in the dealloying solution (*e.g.*, nitric acid), a less noble element (Ag atom) on the topmost surface is start to be dissolved (Figure 1.2a). Once Ag atoms are dissolved, other Ag atoms that were laterally coordinated to the dissolved one have fewer bonds (*i.e.*, low-coordination site such as step edges), thus they are more susceptible to be dissolved in comparison with high-coordinated Ag atoms in the bulk state.[27,33] Consequently, the etching reaction spreads laterally on the top most layer. In here, the rate-limiting step of nanoporosity evolution is the dissolution of the Ag atom from a high-coordination site such as terrace.[34] Meanwhile, the noble element (Au atom) in the topmost terrace rapidly passivates the Ag-etched surface sites by surface diffusion, forming clusters (islands) by agglomeration (Figure 1.2b). When the next layer is etched, clusters are further agglomerated to reduce a surface energy. Eventually, a characteristic spacing, k, between Au clusters is established.[27,33] In addition, because the clusters are always presence within distance k away, Au atoms which are released onto the terrace of second layer would diffuse to the base

of the clusters formed in the first layer. As dissolution occurs layer by layer the surface-diffused Au atoms steadily passivate the low-coordination sites, which lead to the surface roughening (Figure 1.2c). As dealloying further continues, there are insufficient Au atoms to totally passivate the increasing surface area of the noble metal-passivated mounds. Eventually, the insufficient Au atoms on the surface of mounds make the mounds to be undercut and bifurcate, resulting in ligaments (Figure 1.2d). The cycle of undercutting/bifurcation leads to the generation of nanoporosity within the Au-Ag alloys, and the surface area increases as 3D nanopores/ligaments are formed (Figure 1.2e). Actually, the resulting structure is not a porous material which contains only noble gold, but rather a porous alloy whose surface at the atomic scale is comprised of steps passivated with noble element and terraces of the alloy composition (*i.e.*, the ligaments have Au-rich surfaces and Ag-rich interiors).[32] Due to the capillary-driven surface relaxation process (coarsening), the Ag-residues within the ligaments interiors are continuously exposed and dissolved *via* further dealloying, resulting in the bicontinuous nanoporous Au structure (Figure 1.2f).[35] Naturally, the dealloying reaction are stopped if the sample is transferred from the etching solution to water.[29]

1.3. Effects of Dealloying Conditions

Nanoporous metal structures obtained from dealloying process are highly dependent on the dealloying condition, such as alloy composition, dealloying time, temperature, kinds of solutions, and intrinsic property of noble metals. In addition, these dealloying conditions result in the different morphologies (*e.g.*, size or distribution of pore/ligament) of dealloyed nanoporous metal structures. To obtain the desired structure for the specific performances, it is necessary to know the effects of dealloying conditions for the formation of nanoporous metal structure. In this respect, it will be introduced how the dealloying conditions affect to the formation of nanoporous structure in this section.

Alloy composition

As mentioned in previous section, the proper composition of the noble metal element (*i.e.*, parting limit) is required to form nanoporous metal structure. When the composition of the noble metal element (*e.g.*, Au atoms in Au-Ag alloy system) is too low in the alloy system, the resulting structure would not maintain its structure due to the lack of noble metal element, resulting in collapsed by dealloying. On the other hand, if the composition of the noble metal element is too high in the alloy system, the less stable metal element (*e.g.*, Ag atoms in Au-Ag alloy system) would not be dissolved but be passivated by the higher coordination by noble metal element. For example, the composition of Au in Au-Ag alloy system should be between 20 and 45 at% to provide the uniform formation of continuous nanoporous structure.[36,37] In addition, the alloy composition highly influence to not only the initiation of dealloying but also the pore/ligament size of the dealloyed nanoporous metal structure.[38,39] It was observed that the nanoporous Au structure obtained from electrochemical dealloying of $Au_{20}Ag_{80}$ exhibited a mean pore size about twice as large as the ligament size. This result is markedly

different from the pore/ligament size of nanoporous Au structure obtained from chemical dealloying of $Au_{35}Ag_{65}$ alloy precursor.[38] Because the origin of the nanoporosity is based on the dissolving of less stable metal element within the alloy system, it can be concluded that the more Ag content within the alloy precursor would produce more vacancy in the fabricated nanoporous Au structure.

Beside the parting limit, in dealloying reaction, two important key should be satisfied to prepare uniform nanoporous metal structure: (1) The metal components within alloy system should be single phase solid solution, (2) The electrochemical potential should be far difference between metal components. If a binary alloy is not a single phase solid solution across all compositions as like Au-Ag alloy system, a two-phase or multiphase alloy system cannot generate the entirely uniform nanoporous metal structure because the corrosion rate is difference according to the alloy phase. When $Pd_{30}Al_{70}$ alloy is rapidly solidified, it is composed of Al_3Pd and Al_3Pd_2 intermetallic compounds.[40] By the chemical dealloying of this alloy in HCl or NaOH dealloying solution, the Al_3Pd_2 phase is not dealloyed while the Al_3Pd phase can be dealloyed to form nanoporous Pd structure.[40] This different tendency for the corrosion results in a composite material composed with different kinds of nanoporous structures or different pore/ligament size distributions. If the electrochemical potential between two metal elements is not far different, dealloying reaction hardly occurs even though the alloy precursor is single phase. For example, the preparation of nanoporous Pd structure from single-phase Pd-Cu alloy precursor is difficult in the aqueous electrolyte because the difference of electrochemical potential between Pd and Cu is small.

Dealloying time

To obtain complete 3D nanoporosity from dealloying reaction, it should be needed enough time for dealloying solution, which selectively dissolves less stable metal

elements, to penetrate the entire alloy precursor. Naturally, the dealloying time increases as the thickness of alloy precursor increases. For example, in case of dealloying of 100 nm-thick Au-Ag alloys, only very short dealloying time (around 3 min) is required for the complete dealloying by free corrosion in concentrated HNO_3.[41] However, the dealloying time became longer up to 10 h when the thickness of alloy precursor increased to 25 μm.[29] Because the dealloying time for the complete dissolving less stable metal elements is highly dependent on the dealloying rate, the dealloying time required is also adjusted according to the alloy systems. Interestingly, the dealloying time also affects to the size of pore/ligament of resulting nanoporous structures; in general, the longer dealloying time provides the larger pore/ligament size. Ding *et al.* reported that the pore/ligament size of nanoporous Au nanostructures obtained from dealloying of Au-Ag alloys (50 wt% of Au) in concentrated HNO_3 increased from ~8 nm to ~40 nm when dealloying time was extended from 5 min to 24 h.[29] In case of the formation of nanoporous Cu nanostructures by dealloying of $Cu_{30}Mn_{70}$ in 25 mM HCl, the pore size increased from ~15 nm to ~120 nm as the dealloying time was extended from 30 min to 32 h.[42] Even though the less noble metals were almost dissolved from alloy precursors due to the enough dealloying time, the pore and ligament size still coarsens if the resulting nanoporous structures are steadily contact with the dealloying solution. This is because the surface noble metals, which are not dissolved by the dealloying solution and are diffused on the solid/solution interface, have a tendency to reduce their surface energy by forming large-sized ligaments.[29]

Dealloying temperature

Because the mechanism of the formation of nanopore and ligaments during dealloying is highly correlated with the surface diffusivities of the noble metal element, the pore/ligament size of the dealloyed porous structure are usually

influenced by the dealloying temperature. Generally, the pore/ligament size increases as dealloying temperature increases because the high temperature would accelerate the diffusion rate of the less stable (dealloying-active) metal component dissolved and the surface diffusivity of the noble (dealloying-inactive) metal element. According to the reported literature,[43] the nanoporous Au structure with ultrafine pore/ligament structure (~7 nm) was obtained by dealloying of $Au_{35}Ag_{65}$ alloy at a low temperature (-20 °C) for 4 h in concentrated HNO_3. However, the size of pore/ligament increased to ~15 nm and ~28 nm when the dealloying temperature was changed to 0 °C and 25 °C, respectively. Based on the experimental results and the known parameters, the calculated diffusivities of Au atoms in HNO_3 at -20 °C, 0 °C, and 25°C were 9.0×10^{-22}, 1.5×10^{-20}, and 2.0×10^{-19} $m^2 \cdot s^{-1}$, respectively.[22,43] These results indicates that the diffusivity of Au atoms at alloy/electrolyte interfaces was increased up to two orders of magnitude when the dealloying temperature was slightly changed from -20 °C to 25 °C, resulting in a coarsened nanoporous structure.

Nature of noble metal

As mentioned above, the surface diffusivity of the noble metal element at alloy/electrolyte interface can influence to the pore/ligament size of the resulting dealloyed nanoporous structures. The surface diffusivity during dealloying process is not only altered by dealloying temperature but also the intrinsic diffusivity of noble metals. From the reported literature, the surface mass transfer diffusion coefficients in vacuum at room temperature (298 K) are highly dependent on the nature of noble metal; 3.6×10^{-22} for Pt, 1.1×10^{-20} for Pd, 2.2×10^{-19} for Au, and 1.1×10^{-14} $cm^2 \cdot s^{-1}$ for Cu.[44,45] In case of Ag, the surface diffusion is two orders of magnitude faster than that of Au in vacuum.[46] Therefore, the noble metals of which surface diffusion coefficient is high (Pt < Pd < Au < Ag < Cu) can generate the

large-sized pore/ligament structure in the same dealloying condition. For this reason, under the same dealloying conditions, nanoporous Pt structure obtained from dealloying of PtAl alloy exhibited the small-sized pore/ligament (less than 10 nm); however the pore/ligament size of nanoporous Au and nanoporous Ag structures obtained from dealloying of AuAl and AgAl alloys were increased to 60–80 nm and 100–120 nm, respectively.[47]

Dealloying solutions

Besides temperature of dealloying solutions and nature of noble metal, the kinds of dealloying solutions also strongly affect to the surface diffusivity of the noble metal element during dealloying. According to the reported literature,[48] the diffusivities of noble metals increase when the halogen ions (Cl^-, Br^-, and I^-) are adsorbed on the surface of alloy precursors. For this reason, the nanoporous structure obtained from the dealloying of Al-based alloys was coarsened in the presence of the halogen ions during dealloying.[48] In addition, Zhang *et al.* found that the diffusivities of Au increase in the order of I- > Br- > Cl- when the halogen ions are adsorbed during dealloying reaction.[49] Thus, the nanoporous metal structures obtained in HCl solutions usually exhibit a larger ligament size than those obtained in NaOH solutions due to the halogen ions-induced increase of diffusivities of noble metal.[47]

The conventional dealloying reaction usually occurred in the aqueous solutions; however, other solutions (*e.g.*, ionic liquid, supercritical CO_2, organic solvents, and molten metals) have also been used for the advanced dealloying reaction.[50-52] In general, the fabrication of nanoporous Pd structure from Pd-Cu alloys is difficult in the conventional aqueous electrolyte because of the small difference in the electrochemical potential between Pd and Cu. However, Li *et al.* successfully fabricated the nanoporous Pd structure from Pd-Cu alloys by

introducing ionic liquid 1-butyl-3-methylimidazolium tetrafluoroborate as a dealloying solution.[50] In the presence of ionic liquid the less stable metal element (Cu) was selectively dissolved by forming complex ions into the electrolyte, which increased the surface diffusion of noble metal element (Pd), resulting in formation of a nanoporous Pd structure with a large ligament size (~63 nm).

1.4. Fabrications of Nanoporous Gold Nanostructures

Up to date, various alloy systems have been employed to prepare nanoporous metal structure, such as Ag-Au, Ni-Au, Al-Au, Zn-Cu, Al-Cu, Mn-Cu, Ni-Cu, Al-Pt, Cu-Pt, Cu-Pd, *etc*.[53,54] Besides the binary alloy system, recently, ternary alloy systems (*e.g.*, Ni-Cu-Mn, Cu-Fe-Al, Cu-Ag-Au, Pt-Ru-Al, etc) have also been developed.[55-58] All these starting alloy materials result in nanoporous metal structures; however, some materials suffer from the non-uniform and non-stable structures due to the differences in their phase diagrams, differences in lattice constants of the alloy constituents, and the different tendencies to passivate during dealloying.[21] Among the alloy candidates as starting materials, Au-Ag alloy system, which is so-called "solid solution", have been received much attention in a various field (*e.g.*, catalysis, electrochemical/optical sensing, actuation, *etc*.) because its dealloyed structure (*i.e.*, nanoporous Au structure) exhibits many advantages, such as chemical/biological inertness, ease in fabrication, and unique catalytic/optical/mechanical properties.[7-10] In addition, nanoporous Au structures are homogenous throughout the entire materials because starting material (Au-Ag alloy) is single fcc (face-centered cubic) crystal phase regardless of the composition of the alloy, that can be dealloyed to >99%.[8] From this section, hence, the synthesis and applications of the nanoporous Au nanostructures obtained from Au-Ag alloy system will be mainly introduced.

Nanoporous Au thin films

To fabricate 2D metallic thin film structures, several techniques (*e.g.*, thermal evaporation, sputtering deposition, electrochemical plating, etc) have been widely applied.[59-61] In particular, 2D structure of single-phase Au-Ag alloy system should be needed to fabricate the nanoporous Au thin films. For example, Kim *et al.* fabricated nanoporous Au thin films on Si substrate by chemical/electrochemical

dealloying process (Figure 1.3).[62] To prepare single-phase Au-Ag alloy thin film, Au and Ag were consecutively deposited as multilayers of up to 500 nm thickness on a Si substrate by using vapor deposition technique, then the multilayer Au-Ag films were annealed at 310 to 400 °C for various times up to 96 h under air or Ar. During annealing process, multilayer Au-Ag films converted to Au-Ag alloy films as forming single-phase solid solution. Dealloying was then performed using either a chemical or a controlled electrochemical dealloying method with HNO_3 and $HClO_4$, respectively. Moreover, nanoporous Au thin films showing significantly less cracking in tens of millimeters and ligament size under 10 nm were successfully fabricated by careful control of dealloying conditions, such as chemical compositions, heat treatment, dealloying methods, and electrochemical dissolution rate.

When 2D alloy this films are dealloyed on the hard substrate (*e.g.*, Si wafer), it generally shows large densities of grain-boundary cracks and lattice defects within the nanoporous structures due to the surface tension and stress during volume shrinks. This phenomenon leads serious problems for the applications required a reproducibility and reliability. Also, the conventional vapor-deposition-based fabrication technique for the preparation of alloy precursor is incompatible with some of the polymeric substrates, thus it limits the dealloyed nanoporous thin films not to be used for wide applications. To overcome these drawbacks, Ding *et al.* discovered that a commercially available 12 carat white-gold decorative leaf (Au-Ag, 1:1 ratio by weight) can be dealloyed at room temperature by a simple chemical process (floating white-gold decorative leaf onto the concentrated HNO_3) (Figure 1.4).[29] The chemically dealloyed free-standing nanoporous Au leaf showed no surface cracks and lattice defects through large-area, thus 3D interconnected ligaments were highly conductive. In addition, a very thin free-standing porous material (~100 nm thick) is beneficial for the application in electrode because they may be attached to a variety of substrates. Moreover, as-

fabricated nanoporous Au leaf is suitable for various applications such as catalysis, sensing, and filtration owing to its excellent mechanical rigidity, chemical stability, and biocompatibility.

Nanoporous Au nanowires and nanorods

Until now, a template-based synthetic strategy has been widely used for the synthesis of nanoscale nanowires and nanorods with inherent nanoporous structures.[63-68] First of all, to fabricate nanowire or nanotube-shaped nanoporous Au structure, the starting materials (Au-Ag alloys) should be formed in the shape of nanowire and nanorod. The anodic aluminum oxide (AAO) is the most commonly used template for the preparation of Au-Ag alloy nanowire/nanorod.[66] For example, Ji *et al.* fabricated nanoporous Au nanowire by a two-step process: (1) electrochemical deposition of a single-phase binary Au-Ag alloy nanowire into a nanoporous template (AAO), (2) etching of the less noble component (Ag within Au-Ag alloy) to form nanoporous structure (Figure 1.5a). In typical, Au and Ag ions were electrochemically reduced and deposited into the Cu electrode which is attached AAO. By help of an AAO template, the nanowire-shaped Au-Ag alloy structure can be formed. The Au-Ag alloy nanowires were then stripped from the template by dissolving Cu film and AAO template in the $CuCl_2$/HCl and KOH solution, respectively. Finally, nanoporous Au nanowires were prepared by etching of the Ag atoms in concentrated nitric acid. The resulting nanoporous Au nanowire showed large surface area as high as 6.9 $m^2 \cdot g^{-1}$, and the surface morphology of the porous nanowires were controlled by the composition of Au and Ag within nanowire alloy and subsequent thermal annealing.

In addition, nanoporous Au nanotubes have also been fabricated by using Ag nanowire as templates.[69] Gu *et al.* fabricated novel metallic nanoporous nanotubes based on an effective combination of nanocrystal growth and surface

modification (Figure 1.5b-f). To synthesize the Au-Ag alloy as a starting material, firstly, Au atoms were deposited on the Ag nanowire surface with the presence of a cetyltrimethylammonium boromide and ascorbic acid as a surfactant and reducing agent, respectively. Next, as-prepared starting material underwent dealloying process to completely dissolve the Ag atoms located inner (pure Ag nanowire) and the surface (Au-Ag alloy), finally, the nanoporous Au nanotube with porous surfaces and hollow interiors was obtained. Also, the 1D nanoporous structure was modulated by controlling the dealloying steps, such as nanowire growth, surface modification, and thermal diffusion. These tubular nanoporous structures showed not only very high surface area but also distinct optical properties, which can be attractive for sensing and biomedical applications.

Nanoporous Au nanoparticles

Besides the AAO and Ag nanowires as a template for the preparation of 1D nanoporous Au nanostructures, polystyrene (PS) beads have also been used as template to form nanoporous Au nanoparticles.[70,71] For example, Nyce *et al.* reported the PS template-based synthesis of hierarchical porous Au particles (Figure 1.6a and b).[70] At first, Au atoms were deposited on PS beads (10 or 1 μm in diameter) *via* electroless deposition in the presence of stabilizer (polyvinyl (pyrrolidone), PVP), then Ag atoms were also deposited on Au-coated PS beads *via* same process. Next, Au-Ag/PS core/shell particles were heated in an inert atmosphere at 400 °C to remove the PS template and to form Au-Ag alloy shell. To begin the dealloying process, alloyed Au-Ag hollow particle was placed in a nitric acid solution, which resulted in hollow nanoporous Au shells of which dimensions are roughly 9.6 μm in diameter and 200 nm thick, and surface area are 1.48 $m^2 \cdot g^{-1}$. Recently, Zhao *et al.* synthesized monolithic nanoporous Au in the form of disks of sub-wavelength diameter and sub-100 nm thickness by following PS template-

based synthesis route: (1) formation of a monolayer of PS beads on an alloy-coated Si substrate, (2) O_2 plasma shrinkage of the PS beads and Ar sputter etching to form isolated alloy disk, (3) selective dissolution of PS beads by chloroform, and (4) formation of nanoporous Au disks by dealloying (Figure 1.6c-j).[71] In addition, same group also fabricated nanoporous Au disks with a nanoscale internal porous network produced by the combination of lithographic pattering and dealloying process. By controlling thermal annealing steps and adding halides (*e.g.*, KBr and KI) during dealloying step, the morphology and plasmonic resonance of the nanoporous Au disks were precisely controlled.[72,73] Also, Wang *et al.* fabricated an perfectly ordered 2D array of nanoporous Au nanoparticles by using a combination of a "top-down" approach (substrate-conformal imprint lithography) and tow "bottom-up" approaches (dewetting and dealloying).[74] This technique allowed for the control of particle size, particle spacing, and pore/ligament size by controlling the period of the structure, total metal layer thickness, and the thickness ratio of the as-deposited bilayers.

Recently, the template-free fabrication of nanoporous Au nanoparticles has also been realized.[75,76] Li *et al.* reported the dealloying of noble-metal (Au-Ag) alloy nanoparticles by a wet-chemistry (Figure 1.7a-e).[75] Firstly, the citrate-coated ~40 nm diameter Au-Ag alloy nanoparticles of nominal composition $Ag_{0.75}Ag_{0.25}$ were synthesized by a co-reduction of Au/Ag precursor, and then as-synthesized alloy particles were annealed at 400 °C for forming homogeneous alloy composition. Finally, single-phase Au-Ag alloy nanoparticles underwent dealloying process to yield nanoporous Au nanoparticles. Unlike the dealloying from co-reduced Au-Ag alloy nanoparticles, Au/Ag core/shell nanoparticles can be also starting materials to yield nanoporous Au nanoparticles.[76] Liu and co-workers reported a dealloying process for the fabrication of nanoporous Au-Ag alloy nanoparticles from core/shell-typed nanoparticles, which were encased in ultrathin hollow silica (Figure 1.7f-l). At first, Ag atoms were deposited on the Au core

nanoparticles, and then SiO_2 layers were formed on the Au@Ag core/shell nanoparticles. Next, these nanoparticles were then subjected to high-temperature annealing (950 °C), which converted Au@Ag core/shell into the fully alloyed ones, which is referred as AuAg alloy@SiO_2. By following the selective etching of Si layer and Ag atoms, porous Au-Ag nanoparticles encapsulated in the ultrathin hollow silica shell were formed in high yield. By help of an ultrathin hollow silica shell, these porous metal nanoparticles do not need any conventional organic capping ligands for stabilization, thus resulting materials with clean surface are beneficial to the high accessibility of the target molecules desired to attach.

1.5. Applications of Nanoporous Gold Nanostructures

Catalysis

In 2006, both groups[77,78] independently investigated the catalytic oxidation of carbon monoxide (CO) with molecular oxygen (O_2) and detected high catalytic activity of nanoporous Au structure at temperatures even below 0 °C. Previously, almost Au-based catalysts are often supported on reducible oxides (*e.g.*, TiO_2 or CeO_2)[79,80]; however, this unsupported Au nanostructure (*i.e.*, nanoporous Au) can be catalytically active by itself. In addition, the ligaments size in nanoporous Au is relatively large (30 to 40 nm), which is about ten times larger than the upper size limit of 5 nm commonly considered as being essential for catalytic activity.[79,80] It is believed that the low coordinated Au atoms are supposed to bind molecular oxygen more strongly[81] and the activation of molecular oxygen at low coordination site is the origin of the excellent catalytic activity of nanoporous Au.[1] Besides, other group suggests that while the catalytic behavior of nanoporous Au can be explained by the surface chemistry of pure Au, the small quantities of Ag can also play a crucial role in the activation of molecular oxygen.[21] Recently, Fujita *et al*. reported an atomic origins of the high catalytic activity of nanoporous Au.[7] In this study, a high density of atomic steps and kinks is observed on the curved surface of nanoporous Au structure by using spherical-aberration-corrected TEM and environmental TEM. These defects are usually observed in the small nanoparticles of which size is 3–5 nm; however, they were also clearly observed in larger-sized nanoporous Au even when its feature lengths were larger than 30 nm. This observation also provided compelling evidence that such surface defects are active sites for the catalytic oxidation of CO and residual Ag stabilizes the atomic steps by suppressing {111} faceting kinetics.

The oxidation of harmful CO to the nonhazardous CO_2 is very important in exhaust gas cleaning. To evaluate the catalytic reaction of nanoporous Au,

Bäumer's group used the CO oxidation as a test reaction (Figure 1.8a and b).[21,77,82] The catalytic reaction (CO oxidation) by using nanoporous Au structure was initially catalytically inactive; however, the reaction was activated when the nanoporous Au structure was exposed to a gas stream containing CO and O_2 at elevated temperatures (>60 °C). During the first 2 to 3 hours, the catalytic activity was gradually increased and reached a steady state (Figure 1.8a). In addition, they found that the adsorption of CO is rate limiting step, because of (1) a large number of available sites for adsorption or (2) a weak interaction caused by the low adsorption enthalpy. Similar to the reported results,[83,84] interestingly, CO oxidation was highly influenced by the Ag content within nanoporous Au: The reaction could be increased when the Ag content was increased (up to 11 at%) (Figure 1.8b). However, the Ag content was not able to affect to the kinetics even though the overall catalytic activity was modulated as Ag content increased. These findings suggest that Ag content act as a positive role for the CO oxidation but that cannot change the reaction mechanism.

Together with catalytic properties at very low temperature, nanoporous Au can also be a highly selective catalyst. Because the high selectivity of chemical reaction ensures the effective use of resources and lowers the energy consumption, the selective catalyst is very important in an industrial field. Especially, the selective oxidation of methanol is a typical reaction with great industrial relevance because it is the starting compound or a variety of bulk chemicals (*e.g.*, higher alcohols and hydrocarbons, acids and esters). It is worth noting that the nanoporous Au structures which have high surface-to-volume ratio and large fraction of low coordinated surface atoms can be a promising material for the selective oxidation of methanol, because the Au surface particularly shows weak interaction with methanol or its oxidation products *via* low adsorption enthalpies. In 2010, Bäumer's group investigated the gas-phase oxidation of methanol on the nanoporous Au structure (Figure 1.8c and d).[8] The methanol was oxidized to

methyl formate with nearly 100% selectivity, and the undesired side product CO_2 was hardly detectable (Figure 1.8c). They also suggested that the highly selective reaction is based on the combination of three elements; (1) the activation of the Au surface by atomic oxygen, (2) the high reactivity of the surface bonded aldehyde, and (3) the low desorption barrier for methyl formate. Similar to the Ag-residue effect on the CO oxidation, the amount of Ag atoms within the nanoporous Au also influenced to the activity and selectivity of the oxidation of methanol: The selectivity decreased as Ag content increased (Figure 1.8d). From this result, they conclude that Ag-residue can modulate the supply of activated oxygen on the surface, thus eventually reducing the selectivity in favor of total oxidation (*i.e.*, the nanoporous Au structure containing about 10 at% of Ag-residues showed no activity for the formation of methyl formate, resulting in only total oxidation).

Besides CO oxidation and gas phase oxidative coupling of methanol, additional catalytic applications have steadily evolved, such as for example, oxidative coupling of methanol, the liquid phase oxidation of glucose, the electro-oxidation of methanol, oxygen reduction reaction like in fuel cell applications, electrocatalytic hydrogen evolution, carbon dioxide reduction, hydrogenation, and hydrocarbon oxidation, due to the superior catalytic activity and selectivity of nanoporous Au structure.[8,28,85-90]

Electrochemical sensor

Due to the 3D nanoscale pore/ligament structure, nanoporous metallic structure usually exhibits a large specific surface area. According to the reported literature, the specific surface area of nanoporous Au structure is adjusted by a pore/ligament size: The estimated surface area of nanoporous Au structure is ~20 $m^2 \cdot g^{-1}$ for the ~10–20 nm pore size, which decrease down to ~8 and ~4 $m^2 \cdot g^{-1}$ when pore/ligament size increase to ~90 and ~150 nm, respectively.[91,92] With large

specific surface area, high electronic conductivity, excellent electrochemical activity and good biocompatibility ensure that nanoporous Au nanostructures are promising in electrochemical sensor. These outstanding features directly make nanoporous Au structures very sensitive for electrochemical determination of small molecules, such as glucose, hydrazine, NADH, H_2O_2, dopamine, *etc*.[93-98] In addition, nanoporous Au-based electrochemical sensor shows good selectivity for the detection of small molecules.[94-96]

Due to the good biocompatibility and the strong interaction between enzymes and nanoscale gold surfaces, the nanoporous Au structures can be used in enzyme-based sensor by immobilizing enzymes on the solid supports. Especially, nanoporous Au can be used for the preparation of various dehydrogenase- and oxidase-based electrochemical biosensors. By combining the biocatalytic activity of enzymes and the electrocatalytic activity of nanoporous Au structure, the enzyme-modified nanoporous Au electrodes can detect the ethanol and glucose, respectively, from the ethanol dehydrogenase coupled with glucose oxidase (GOx).[93,99] Typically, nanoporous Au-based electrochemical sensor detects the enzymatic product (H_2O_2) obtained from the GOx-induced oxidation of glucose. Besides, another kind of enzyme-based biosensor, based on the direct electron transfer (DET) between enzymes and nanoporous Au electrode, has also been developed.[100] By the unique physicochemical properties (*e.g.*, electron conductivity and nanoscale metal ligaments) of nanoporous Au structure, the DET of enzymes can be facilitated to the electrochemical sensor.

Recently, nanoporous Au structures with a high surface area, excellent catalytic activity and electron conductivity, and biocompatibility have been widely used as the substrate electrode for antibody anchoring, thus they can be also applied to the sandwich-type immunosensors.[101] Figure 1.9a shows the nanoporous Au structure-based sensitive detection of cancer antigen 15-3 (CA 15-3). First, the nanoporous Au was covered on the graphene/GCE (glassy carbon electrode) as the

substrate electrode for antibody immobilization. When liposome (~100 nm) which incorporates HRP (horseradish peroxidease) forms sandwich architecture with the antibody-immobilized nanoporous Au structure in the presence of antigen (CA 15-3), the specific signal are detected. The linear range of the immunosensor was 2×10^{-5} to 40 $U \cdot mL^{-1}$ under optimized conditions, and a detection limit was estimated as 5×10^{-5} $U \cdot mL^{-1}$ (Figure 1.9b). Besides the sandwich-type innunosensor, a nanoporous Au based label-free immunosensor has also been reported.[102,103]

Similar to the sandwich-type immunosensors, the nanoporous Au structure has also been used as a substrate electrode for the detection of DNA. In this system, a specific DNA of which sequence can capture target DNA strand is immobilized on the nanoporous Au electrode. The other part of target DNA strand is also captured by signal-giving materials of which surface are modified with a specific DNA. Figure 1.9c shows the nanoporous Au structure-based sensitive detection of target DNA strands.[104] When the DNA-immobilized nanoporous Au substrate electrode are hybridized with the DNA-functionalized Au nanoparticles in the presence of target DNA, the sandwich-type complex are formed. In here, the signal can be quantitatively detected as $Ru(NH_3)_6^{3+}$ are electrostatically adsorbed on the negatively charged single strand DNA which attached on the Au nanoparticles.

Optical sensor

When the size of the metal is much smaller than the wavelength of light, the collective oscillation of the free conductive electrons excited by visible light, called as surface plasmon resonance (SPR). Due to the SPR, generally, the metallic nanostructures show significantly different and unique optical properties in comparison with their bulk counterparts.[105] In particular, the nanoporous Au structures which have the integrated ligaments and pores exhibits unique plasmonic properties compared with other metal nanostructures, such as nanoparticles,

nanorods, *etc*. For instance, the 2D nanoporous thin film of which thickness is about 100 nm showed excitation of propagating SPR in planar metal films and localized SPR, simultaneously.[106-108] In addition, the plasmonic properties of the nanoporous Au structure can be tuned by the pore/ligament size and dielectric surroundings.[71,109-111]

Due to the unique plasmonic properties and huge surface area (*i.e.*, metal/dielectric interfaces), the nanoporous Au structures have received great attention for sensing applications. Because the SPR of nanoporous Au can enhance the surface fluorescence of small molecules such as Cy3 or the photoluminescence of silicon nanocrystals and quantum dots (QDs),[112-114] the uniform nanoporous structure and metal-enhanced fluorescence make nanoporous Au structure appropriate for fluorescence-based assays. For example, Lang *et al*. found that the nanoporous Au with a small pore size and large ligament size could remarkably improve the fluorescence intensity of Cy3 on nanoporous Au.[112] In this study, the maximum enhancement of fluorescence intensity was obtained by a factor of 191. This ultrahigh enhancement is caused by the strengthening of localized SPR by the small nanopore size and simultaneous weakening of plasmonic damping by the large ligament size. Similarly, the nanoporous Au yielded a four-fold and 100-fold enhancement in photoluminescence of Si nanocrystals and QDs, respectively.[113,114] Recently, Ahmed *et al.* reported a nanoporous Au-based optical sensor which detects influenza A virus by using antibody-modified QDs and nanoporous Au structure.[115] By help of the fluorescence enhancing effect of nanoporous Au, the detection limit (1 $ng \cdot mL^{-1}$) could be improved in two-order of magnitude compared with a commercially available rapid influenza diagnostic test.

For both fundamental science and sensing applications, the fabrication of highly surface-enhanced Raman scattering (SERS)-active metallic substrates is one of the main goal in the field of plasmonic.[116] The nanoporous Au structure is a promising material for the SERS-based optical sensing applications due to (1) the

high density of nanopore which can cause the electromagnetic field enhancement by plasmon excitation and (2) electromagnetic coupling between neighboring ligaments. For the first time, Chen *et al.* investigated the effect of pore size on the SERS property of nanoporous Au structure.[117] In this study, the SERS enhancement of nanoporous Au is highly related to its pore size: The smaller pore size exhibited the higher SERS enhancement because a smaller pore causes the stronger electromagnetic field enhancement by plasmon excitation of nanoporous Au. In addition, other study demonstrated that the surface morphology of nanoporous Au structure can also influence to the SERS enhancement, that is, the roughed ligament surface produced by the annealing contributed to the strong SERS enhancement.[118] Based on the knowledge for enhancing SERS property (*e.g.*, smaller pore size and roughen ligament structure), Chen and co-workers improved the SERS enhancement of nanoporous Au structure by fabricating a wrinkled nanoporous Au films.[119] To fabricate the wrinkled nanoporous Au films, the conventional free-standing nanoporous Au film was placed on a polymer substrate, and then was accomplished by a thermal treatment. As a result, thermal treatment induced shrinkage of the polymer substrate, and 2D flat nanoporous Au film were changed to 3D wrinkled nanoporous Au structure which contains abundant SERS-active nanogaps and fractures. The wrinkled nanoporous Au structure exhibited the average enhancement factor as high as 0.7×10^8, which is much higher than the original nanoporous Au film ($\sim 10^6$).

Because the nanoporous Au structure provides biocompatibility, excellent chemical stability, and strong optical properties, it is an ideal candidate for the SERS-based ultrasensitive/reproducible detection of small molecules. For example, Zhang *et al.* developed a nanoporous Au-based optical sensor to detect Hg^{2+} ions.[120] When Hg^{2+} is added to the Cy5-labeled aptamer on the nanoporous Au film, the SERS signals of Cy5 decreases as the distance is far from the nanoporous Au substrate by the interaction between Hg^{2+} and aptamer (Figure 1.10a-d). This

nanoporous Au substrate-based optical sensor showed an excellent detection sensitivity of 1 pM (0.2 ppt) and selectivity. Similarly, Shin *et al*. developed a label-free method to detect single stranded DNA (ssDNA) by *in situ* monitoring of DNA hybridization (Figure 1.10e-g).[9] The strong SERS signals can be obtained because of the short distance between Cy3 molecules and the nanoporous Au surface; however, the SERS signals of Cy3 molecules would decrease and even disappear due to the long distance from nanoporous Au surface as the straight and rigid DNA complex were formed in the presence of target ssDNA. Moreover, this simple and fast detection method can detect the hybridization events within 10 min after introducing only 20 pM target ssDNA molecules.

Chemical actuation

As already described, the catalytic properties of nanoporous Au is excellent due to its high surface energy caused by a low coordination number. Also, the lower coordination number of surface atoms causes a charge redistribution into in-plane surface bonds that gives rise to surface stress.[21] Owing to the surface stress is highly sensitive to changes in the surface state,[121] an adsorption of molecules on the metal surface can also influence to the surface stress. In particular, changes in the surface stress, in the case of nanoporous Au structures which have high-surface-area, can lead to macroscopically detectable strain effects.[122,123] For example, Biener *et al*. observed the macroscopic strain effect caused by the surface stress in nanoporous Au while exposing nanoporous Au alternatively to ozone and CO (Figure 1.11).[10] When ozone (O_3) is adsorbed on the Au surface, the Au surface is covered by the oxygen (O_2) *via* $O_3 + Au \rightarrow O_2 + Au–O$,[124] This oxygen then leads the change in the surface electronic structure due to its high electronegativity, which modifies the surface stress. In addition, the adsorbed oxygen can be removed by CO exposure to restore the clean Au surface, *via* $CO + Au–O \rightarrow CO_2 + Au$.

During the sequential surface reaction, the surface states is switched back and forth between the oxygen-covered surface (after exposing to O_3) and the clean surface (after exposing to CO), consequently the surface stress is changed by surface chemistry at the solid-gas interface. As a result, the difference of surface stress between two surface states induced the reversible changes in the sample length. Depending on the gases exposure time, the amplitude of strain was altered between 0.05 and 0.5%. From this work, it is worth noting that the nanoporous Au structure acts as a chemical actuation which could convert the chemical energy into mechanical work.

Moreover, this concept, which transforms chemical energy directly into mechanical work, can be applied to the gas-sensor. Because the contraction and expansion of sample is dependent on the amount of O_3, it is possible to detect the amount of O_3 by measuring the displacement of the sample surface. Based on this concept, chemical actuation-based gas sensor of which size is 10 μm detected the O_3 gas in the order of 10^{-12} mol.[10]

1.6. Conclusions and Perspectives

Although corrosion of metals is a well-know and an old fabrication technique, it provides a new class of nanomaterials with an extraordinary structural property by connecting with an advanced recent nanotechnology. Despite of the relatively short history, the dealloying-based nanoporous metallic materials, which exhibit excellent surface reactivity, chemical/biological stability, electrical conductivity, and mechanical rigidity, have produced very important and promising achievement in the wide field of applications (*e.g.*, catalysis, sensing, optics, actuator, *etc*.) In addition, many intensive efforts to understand and control the dealloying process have led to new and unexpected effects that open up new opportunities for both fundamental research and practical applications. However, surface-stabilization of microstructure of nanoporous metallic structure (especially, for metals showing fast surface diffusivities such as Cu and Ag) should be solved. For the cost-effective and practical applications, a rational design to fabricate nanoporous non-noble metal structures (*e.g.*, Ni, Fe, *etc*.) is also required. However, the dealloying-based fabrication of uniform nanoporous non-noble metal structure is still challenging because the non-noble metals are highly active to control the microstructure and single-phase alloying is relatively limited.

Until now, most of nanoporous metals are 3D or 2D structures which are not suitable for some specific applications such as drug delivery, nanomedicine, and labeling in immunosensing. Of course, some recent studies cover the fabrication of nanoporous metallic nanoparticle, however, those synthesis methods need complex route such as annealing process, and resulting products are usually not uniform in size, which cannot provide reproducibility and reliability in sensing application. As expected, nanoporous metallic nanoparticles are most promising materials for biomedical applications due to (1) their high surface are for loading of drug and targeting molecule, and (2) tunable and unique SPR properties for

enlarging the sensing signal. Nevertheless, only much less reports about the facile fabrication of uniform nanoporous metallic nanoparticles have been reported because the fabrication of uniform alloy nanoparticles with suitable composition and size is still quite challenging due to the different chemical properties of each metal elements. For these reason, the advanced synthesis technique for preparation of uniform and pore/ligament size-controllable porous metallic nanoparticles is urgent and also deserves more studies.

1.7. References

1. Ding, Y.; Chen, M. *MRS Bull.* **2009**, *34*, 569.
2. Forty, A. J. *Nature* **1979**, *282*, 597.
3. Rambert, S.; Landolt, D. *Electrochim. Acta* **1986**, *31*, 1421.
4. Rambert, S.; Landolt, D. *Electrochim. Acta* **1986**, *31*, 1433.
5. Smith, A. J.; Tran, T.; Wainwright, M. S. *J. Appl. Electrochem.* **1999**, *29*, 1085.
6. Min, U.-S.; Li, J. C. M. *J. Mater. Res.* **1994**, *9*, 2878.
7. Fujita, T.; Guan, P.; McKenna, K.; Lang, X.; Hirata, A.; Zhang, L.; Tokunaga, T.; Arai, S.; Yamamoto, Y.; Tanaka, N.; Ishikawa, Y.; Asao, N.; Yamamoto, Y.; Erlebacher, J.; Chen, M. *Nat. Mater.* **2012**, *11*, 775.
8. Wittstock, A.; Zielasek, V.; Biener, J.; Friend, C. M.; Bäumer, M. *Science* **2010**, *327*, 319.
9. Qi, J.; Zeng, J.; Zhao, F.; Lin, S. H.; Raja, B.; Strych, U.; Willson, R. C.; Shih, W.-C. *Nanoscale* **2014**, *6*, 8521.
10. Biener, J.; Wittstock, A.; Zepeda-Ruiz, L. A.; Biener, M. M.; Zielasek, V.; Kramer, D.; Viswanath, R. N.; Weissmuller, J.; Baumer, M.; Hamza, A. V. *Nat. Mater.* **2009**, *8*, 47.
11. Chan, V. Z.-H.; Hoffman, J.; Lee, V. Y.; Iatrou, H.; Avgeropoulos, A.; Hadjichristidis, N.; Miller, R. D.; Thomas, E. L. *Science* **1999**, *286*, 1716.
12. Xia, Y.; Gates, B.; Yin, Y.; Lu, Y. *Adv. Mater.* **2000**, *12*, 693.
13. Kresge, C. T.; Leonowicz, M. E.; Roth, W. J.; Vartuli, J. C.; Beck, J. S. *Nature* **1992**, *359*, 710.
14. Seshadri, R.; Meldrum, F. C. *Adv. Mater.* **2000**, *12*, 1149.
15. Raney, M. *U.S. Patent* **1927**, *1 628 190*.
16. Huber, G. W.; Shabaker, J. W.; Dumesic, J. A. *Science* **2003**, *300*, 2075.
17. Pickering, H. W.; Swann, P. R. *Corrosion* **1963**, *19*, 373.

18. Swann, P. R. *Corrosion* **1969**, *25*, 147.

19. Newman, R. C.; Sieradzki, K. *MRS Bull.* **1999**, *24*, 12.

20. Oppenheim, I. C.; Trevor, D. J.; Chidsey, C. E. D.; Trevor, P. L.; Sieradzki, K. *Science* **1991**, *254*, 687.

21. Wittstock, A.; Biener, J.; Bäumer, M. *Phys. Chem. Chem. Phys.* **2010**, *12*, 12919.

22. Dursun, A.; Pugh, D. V.; Corcoran, S. G. *J. Electrochem. Soc.* **2003**, *150*, B355.

23. Sieradzki, K.; Dimitrov, N.; Movrin, D.; McCall, C.; Vasiljevic, N.; Erlebacher, J. *J. Electrochem. Soc.* **2002**, *149*, B370.

24. Dursun, A.; Pugh, D. V.; Corcoran, S. G. *J. Electrochem. Soc.* **2005**, *152*, B65.

25. Dursun, A.; Pugh, D. V.; Corcoran, S. G. *Electrochem. Solid State Lett.* **2003**, *6*, B32.

26. Corcoran, S. G.; Wiesler, D.; Barker, J.; Sieradzki, K. *MRS Proceedings* **2011**, *376*.

27. Erlebacher, J.; Aziz, M. J.; Karma, A.; Dimitrov, N.; Sieradzki, K. *Nature* **2001**, *410*, 450.

28. Ding, Y.; Chen, M.; Erlebacher, J. *J. Am. Chem. Soc.* **2004**, *126*, 6876.

29. Ding, Y.; Kim, Y.-J.; Erlebacher, J. *Adv. Mater.* **2004**, *16*, 1897.

30. Fujita, T.; Qian, L.-H.; Inoke, K.; Erlebacher, J.; Chen, M.-W. *Appl. Phys. Lett.* **2008**, *92*, 251902.

31. Biener, J.; Hodge, A. M.; Hayes, J. R.; Volkert, C. A.; Zepeda-Ruiz, L. A.; Hamza, A. V.; Abraham, F. F. *Nano Lett.* **2006**, *6*, 2379.

32. Erlebacher, J.; Seshadri, R. *MRS Bull.* **2009**, *34*, 561.

33. Erlebacher, J.; Sieradzki, K. *Scr. Mater.* **2003**, *49*, 991.

34. Snyder, J.; Erlebacher, J. *J. Electrochem. Soc.* **2010**, *157*, C125.

35. McCue, I.; Benn, E.; Gaskey, B.; Erlebacher, J. *Ann. Rev. Mater. Res.* **2016**, *46*, 263.

36. Kertis, F.; Snyder, J.; Govada, L.; Khurshid, S.; Chayen, N.; Erlebacher, J. *JOM* **2010**, *62*, 50.

37. Artymowicz, D. M.; Erlebacher, J.; Newman, R. C. *Philos. Mag.* **2009**, *89*, 1663.

38. Rösner, H.; Parida, S.; Kramer, D.; Volkert, C. A.; Weissmüller, J. *Adv. Eng. Mater.* **2007**, *9*, 535.

39. Wang, X.; Qi, Z.; Zhao, C.; Wang, W.; Zhang, Z. *J. Phys. Chem. C* **2009**, *113*, 13139.

40. Wang, X.; Wang, W.; Qi, Z.; Zhao, C.; Ji, H.; Zhang, Z. *J. Alloy. Compd.* **2010**, *508*, 463.

41. Qiu, H.-J.; Peng, L.; Li, X.; Xu, H. T.; Wang, Y. *Corrosion Sci.* **2015**, *92*, 16.

42. Chen, L.-Y.; Yu, J.-S.; Fujita, T.; Chen, M.-W. *Adv. Funct. Mater.* **2009**, *19*, 1221.

43. Qian, L. H.; Chen, M. W. *Appl. Phys. Lett.* **2007**, *91*, 083105.

44. Seebauer, E. G.; Allen, C. E. *Prog. Surf. Sci.* **1995**, *49*, 265.

45. Beszeda, I.; Gontier-Moya, E. G.; Beke, D. L. *Surf. Sci.* **2003**, *547*, 229.

46. Hirai, N.; Tanaka, H.; Hara, S. *Appl. Surf. Sci.* **1998**, *130–132*, 506.

47. Zhang, Z.; Wang, Y.; Qi, Z.; Zhang, W.; Qin, J.; Frenzel, J. *J. Phys. Chem. C* **2009**, *113*, 12629.

48. Newman, R. C.; Sieradzki, K. *Science* **1994**, *263*, 1708.

49. Zhang, Z.; Zhang, C.; Sun, J.; Kou, T. *RSC Adv.* **2012**, *2*, 4481.

50. Li, W.; Ma, H.; Huang, L.; Ding, Y. *Phys. Chem. Chem. Phys.* **2011**, *13*, 5565.

51. Morrish, R.; Muscat, A. J. *Chem. Mat.* **2009**, *21*, 3865.

52. Wada, T.; Yubuta, K.; Inoue, A.; Kato, H. *Mater. Lett.* **2011**, *65*, 1076.

53. Pugh, D. V.; Dursun, A.; Corcoran, S. G. *J. Mater. Res.* **2003**, *18*, 216.

54. Cortie, M. B.; Maaroof, A. I.; Smith, G. B. *Gold Bull.* **2005**, *38*, 14.

55. Snyder, J.; Asanithi, P.; Dalton, A. B.; Erlebacher, J. *Adv. Mater.* **2008**, *20*, 4883.

56. Qiu, H.-J.; Ito, Y.; Chen, M. W. *Scr. Mater.* **2014**, *89*, 69.

57. Qi, Z.; Gong, Y.; Zhang, C.; Xu, J.; Wang, X.; Zhao, C.; Ji, H.; Zhang, Z. *J. Mater. Chem.* **2011**, *21*, 9716.

58. Wei, Q.; Zhao, Y.; Du, B.; Wu, D.; Cai, Y.; Mao, K.; Li, H.; Xu, C. *Adv. Funct. Mater.* **2011**, *21*, 4193.

59. Reichelt, K.; Jiang, X. *Thin Solid Films* **1990**, *191*, 91.

60. Lu, X.; Balk, T. J.; Spolenak, R.; Arzt, E. *Thin Solid Films* **2007**, *515*, 7122.

61. Stiger, R. M.; Gorer, S.; Craft, B.; Penner, R. M. *Langmuir* **1999**, *15*, 790.

62. Kim, M.; Ha, W.-J.; Anh, J.-W.; Kim, H.-S.; Park, S.-W.; Lee, D. *J. Alloy. Compd.* **2009**, *484*, 28.

63. Liu, L.; Pippel, E.; Scholz, R.; Gösele, U. *Nano Lett.* **2009**, *9*, 4352.

64. Liu, L.; Scholz, R.; Pippel, E.; Gösele, U. *J. Mater. Chem.* **2010**, *20*, 5621.

65. Du, C.; Chen, M.; Wang, W.; Yin, G. *ACS Appl. Mater. Interfaces* **2011**, *3*, 105.

66. Ji, C.; Searson, P. C. *J. Phys. Chem. B* **2003**, *107*, 4494.

67. Shin, T.-Y.; Yoo, S.-H.; Park, S. *Chem. Mat.* **2008**, *20*, 5682.

68. Yoo, S.-H.; Park, S. *Adv. Mater.* **2007**, *19*, 1612.

69. Gu, X.; Xu, L.; Tian, F.; Ding, Y. *Nano Res.* **2009**, *2*, 386.

70. Nyce, G. W.; Hayes, J. R.; Hamza, A. V.; Satcher, J. H. *Chem. Mat.* **2007**, *19*, 344.

71. Zhao, F.; Zeng, J.; Parvez Arnob, M. M.; Sun, P.; Qi, J.; Motwani, P.; Gheewala, M.; Li, C.-H.; Paterson, A.; Strych, U.; Raja, B.; Willson, R. C.; Wolfe, J. C.; Lee, T. R.; Shih, W.-C. *Nanoscale* **2014**, *6*, 8199.

72. Zeng, J.; Zhao, F.; Qi, J.; Li, Y.; Li, C.-H.; Yao, Y.; Lee, T. R.; Shih, W.-C. *RSC Adv.* **2014**, *4*, 36682.

73. Zeng, J.; Zhao, F.; Li, M.; Li, C.-H.; Lee, T. R.; Shih, W.-C. *J. Mater. Chem. C* **2015**, *3*, 247.

74. Wang, D.; Ji, R.; Albrecht, A.; Schaaf, P. *Beilstein J. Nanotechnol.* **2012**, *3*, 651.

75. Li, X.; Chen, Q.; McCue, I.; Snyder, J.; Crozier, P.; Erlebacher, J.; Sieradzki, K. *Nano Lett.* **2014**, *14*, 2569.

76. Liu, K.; Bai, Y.; Zhang, L.; Yang, Z.; Fan, Q.; Zheng, H.; Yin, Y.; Gao, C. *Nano Lett.* **2016**, *16*, 3675.

77. Zielasek, V.; Jürgens, B.; Schulz, C.; Biener, J.; Biener, M. M.; Hamza, A. V.; Bäumer, M. *Angew. Chem.-Int. Edit.* **2006**, *45*, 8241.

78. Xu, C.; Su, J.; Xu, X.; Liu, P.; Zhao, H.; Tian, F.; Ding, Y. *J. Am. Chem. Soc.* **2007**, *129*, 42.

79. Bond, G. C.; Thompson, D. T. *Gold Bull.* **2000**, *33*, 41.

80. Bond, G. C.; Thompson, D. T. *Catal. Rev.-Sci. Eng.* **1999**, *41*, 319.

81. Falsig, H.; Hvolbæk, B.; Kristensen, I. S.; Jiang, T.; Bligaard, T.; Christensen, C. H.; Nørskov, J. K. *Angew. Chem.-Int. Edit.* **2008**, *47*, 4835.

82. Wittstock, A.; Neumann, B.; Schaefer, A.; Dumbuya, K.; Kübel, C.; Biener, M. M.; Zielasek, V.; Steinrück, H.-P.; Gottfried, J. M.; Biener, J.; Hamza, A.; Bäumer, M. *J. Phys. Chem. C* **2009**, *113*, 5593.

83. Iizuka, Y.; Miyamae, T.; Miura, T.; Okumura, M.; Daté, M.; Haruta, M. *J. Catal.* **2009**, *262*, 280.

84. Iizuka, Y.; Kawamoto, A.; Akita, K.; Daté, M.; Tsubota, S.; Okumura, M.; Haruta, M. *Catal. Lett.* **2004**, *97*, 203.

85. Yin, H.; Zhou, C.; Xu, C.; Liu, P.; Xu, X.; Ding, Y. *J. Phys. Chem. C* **2008**, *112*, 9673.

86. Jia, C.; Yin, H.; Ma, H.; Wang, R.; Ge, X.; Zhou, A.; Xu, X.; Ding, Y. *J. Phys. Chem. C* **2009**, *113*, 16138.

87. Zhang, J.; Liu, P.; Ma, H.; Ding, Y. *J. Phys. Chem. C* **2007**, *111*, 10382.

88. Zeis, R.; Lei, T.; Sieradzki, K.; Snyder, J.; Erlebacher, J. *J. Catal.* **2008**, *253*, 132.

89. Tappan, B. C.; Steiner, S. A.; Luther, E. P. *Angew. Chem.-Int. Edit.* **2010**, *49*, 4544.

90. Zhang, J.; Li, C. M. *Chem. Soc. Rev.* **2012**, *41*, 7016.

91. Qiu, H.; Xu, C.; Huang, X.; Ding, Y.; Qu, Y.; Gao, P. *J. Phys. Chem. C* **2008**, *112*, 14781.

92. Tan, Y. H.; Davis, J. A.; Fujikawa, K.; Ganesh, N. V.; Demchenko, A. V.; Stine, K. J. *J. Mater. Chem.* **2012**, *22*, 6733.

93. Qiu, H.; Xue, L.; Ji, G.; Zhou, G.; Huang, X.; Qu, Y.; Gao, P. *Biosens. Bioelectron.* **2009**, *24*, 3014.

94. Chen, L. Y.; Lang, X. Y.; Fujita, T.; Chen, M. W. *Scr. Mater.* **2011**, *65*, 17.

95. Liu, Z.; Du, J.; Qiu, C.; Huang, L.; Ma, H.; Shen, D.; Ding, Y. *Electrochem. Commun.* **2009**, *11*, 1365.

96. Qiu, H.-J.; Zhou, G.-P.; Ji, G.-L.; Zhang, Y.; Huang, X.-R.; Ding, Y. *Colloid Surf. B-Biointerfaces* **2009**, *69*, 105.

97. Yan, X.; Meng, F.; Cui, S.; Liu, J.; Gu, J.; Zou, Z. *J. Electroanal. Chem.* **2011**, *661*, 44.

98. Jia, F.; Yu, C.; Ai, Z.; Zhang, L. *Chem. Mat.* **2007**, *19*, 3648.

99. Chen, L. Y.; Fujita, T.; Chen, M. W. *Electrochim. Acta* **2012**, *67*, 1.

100. Zhu, A.; Tian, Y.; Liu, H.; Luo, Y. *Biomaterials* **2009**, *30*, 3183.

101. Ge, S.; Jiao, X.; Chen, D. *Analyst* **2012**, *137*, 4440.

102. Wei, Q.; Zhao, Y.; Xu, C.; Wu, D.; Cai, Y.; He, J.; Li, H.; Du, B.; Yang, M. *Biosens. Bioelectron.* **2011**, *26*, 3714.

103. Shulga, O. V.; Zhou, D.; Demchenko, A. V.; Stine, K. J. *Analyst* **2008**, *133*, 319.

104. Hu, K.; Lan, D.; Li, X.; Zhang, S. *Anal. Chem.* **2008**, *80*, 9124.

105. Eustis, S.; El-Sayed, M. A. *Chem. Soc. Rev.* **2006**, *35*, 209.

106. Dixon, M. C.; Daniel, T. A.; Hieda, M.; Smilgies, D. M.; Chan, M. H. W.; Allara, D. L. *Langmuir* **2007**, *23*, 2414.

107. Yu, F.; Ahl, S.; Caminade, A.-M.; Majoral, J.-P.; Knoll, W.; Erlebacher, J. *Anal. Chem.* **2006**, *78*, 7346.

108. Ahl, S.; Cameron, P. J.; Liu, J.; Knoll, W.; Erlebacher, J.; Yu, F. *Plasmonics* **2008**, *3*, 13.

109. Lang, X.; Qian, L.; Guan, P.; Zi, J.; Chen, M. *Appl. Phys. Lett.* **2011**, *98*, 093701.

110. Qian, L.; Shen, B.; Qin, G. W.; Das, B. *J. Chem. Phys.* **2011**, *134*, 014707.

111. Qian, L.; Shen, W.; Das, B.; Shen, B.; Qin, G. W. *Chem. Phys. Lett.* **2009**, *479*, 259.

112. Lang, X. Y.; Guan, P. F.; Fujita, T.; Chen, M. W. *Phys. Chem. Chem. Phys.* **2011**, *13*, 3795.

113. Biteen, J. S.; Pacifici, D.; Lewis, N. S.; Atwater, H. A. *Nano Lett.* **2005**, *5*, 1768.

114. Zhang, L.; Song, Y.; Fujita, T.; Zhang, Y.; Chen, M.; Wang, T.-H. *Adv. Mater.* **2014**, *26*, 1289.

115. Ahmed, S. R.; Hossain, M. A.; Park, J. Y.; Kim, S.-H.; Lee, D.; Suzuki, T.; Lee, J.; Park, E. Y. *Biosens. Bioelectron.* **2014**, *58*, 33.

116. Liu, H.; Zhang, L.; Lang, X.; Yamaguchi, Y.; Iwasaki, H.; Inouye, Y.; Xue, Q.; Chen, M. *Sci. Rep.* **2011**, *1*, 112.

117. Qian, L. H.; Yan, X. Q.; Fujita, T.; Inoue, A.; Chen, M. W. *Appl. Phys. Lett.* **2007**, *90*, 153120.

118. Kucheyev, S. O.; Hayes, J. R.; Biener, J.; Huser, T.; Talley, C. E.; Hamza, A. V. *Appl. Phys. Lett.* **2006**, *89*, 053102.

119. Zhang, L.; Lang, X.; Hirata, A.; Chen, M. *ACS Nano* **2011**, *5*, 4407.

120. Zhang, L.; Chang, H.; Hirata, A.; Wu, H.; Xue, Q.-K.; Chen, M. *ACS Nano* **2013**, *7*, 4595.

121. Bach, C. E.; Giesen, M.; Ibach, H.; Einstein, T. L. *Phys. Rev. Lett.* **1997**, *78*, 4225.

122. Biener, J.; Wittstock, A.; Baumann, T.; Weissmüller, J.; Bäumer, M.; Hamza, A. *Materials* **2009**, *2*, 2404.

123. Kramer, D.; Viswanath, R. N.; Weissmüller, J. *Nano Lett.* **2004**, *4*, 793.

124. Saliba, N.; Parker, D. H.; Koel, B. E. *Surf. Sci.* **1998**, *410*, 270.

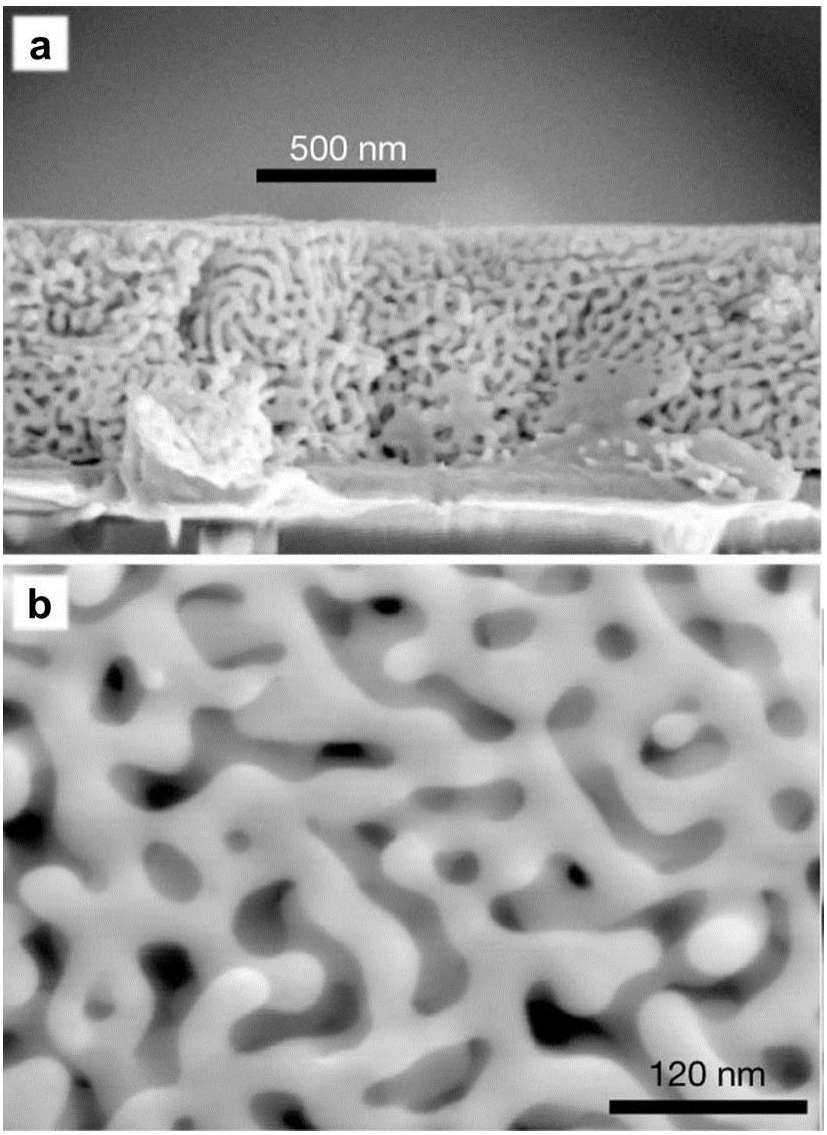

Figure 1.1. Scanning electron microcopy (SEM) images of nanoporous Au produced by removal of Ag from Au-Ag alloys. (a) Cross-sectional SEM image of nanoporous Au thin film obtained from dealloying of $Au_{0.32}Ag_{0.68}$ (at%) alloys. (b) SEM images of nanoporous Au thin film of which ligament spacing is the order of 10 nm. Images were reproduced with permission from ref 27, Copyright 2001 Nature Publishing Group.

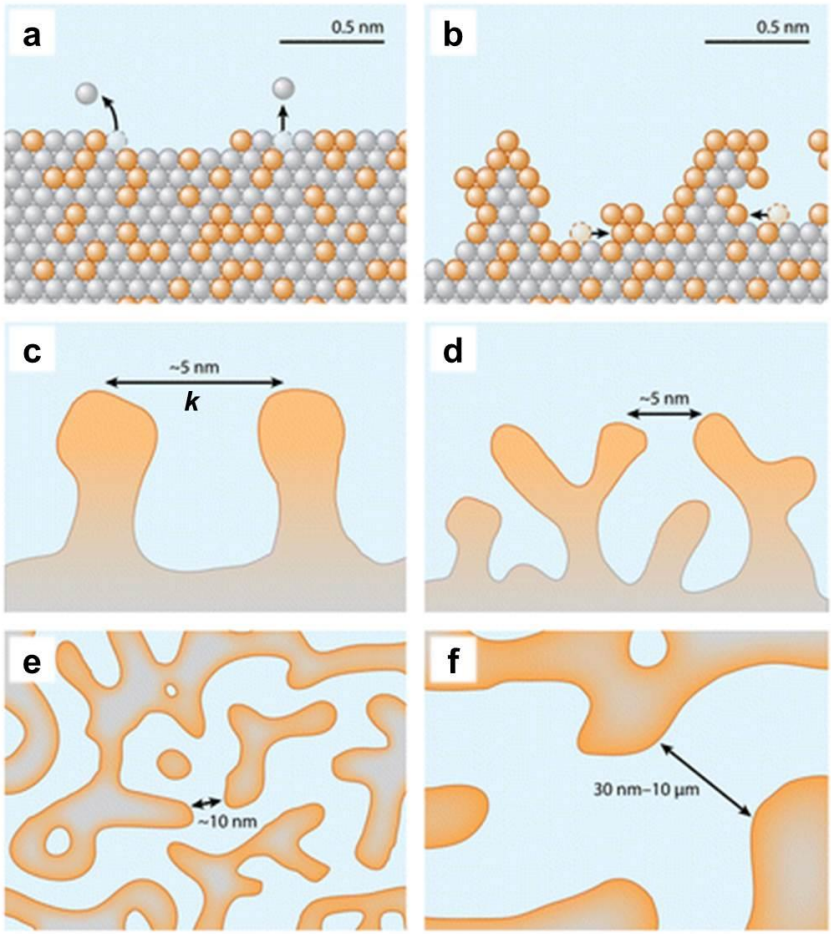

Figure 1.2. Mechanism of evolution of nanoporosity from Au-Ag alloy system during dealloying. Gray and orange color indicate Ag and Au atom, respectively. (a) Selective dissolution of less stable elements (Ag atoms) by dealloying solution. (b) Surface diffusion of noble metals (Au atoms) and passivation of Ag-etched surface sites. (c) Formation of clusters by agglomeration of surface-diffused Au atoms. (d) Undercutting and bifurcation of ligaments. (e) Generation of nanoporosity composed by ligaments which have Au-rich surfaces and Ag-rich interiors. (f) Capillary-driven surface relaxation process (coarsening) to form bicontinuous nanoporous Au structure. Images were reproduced with permission from ref 35, Copyright 2016 Annual Reviews.

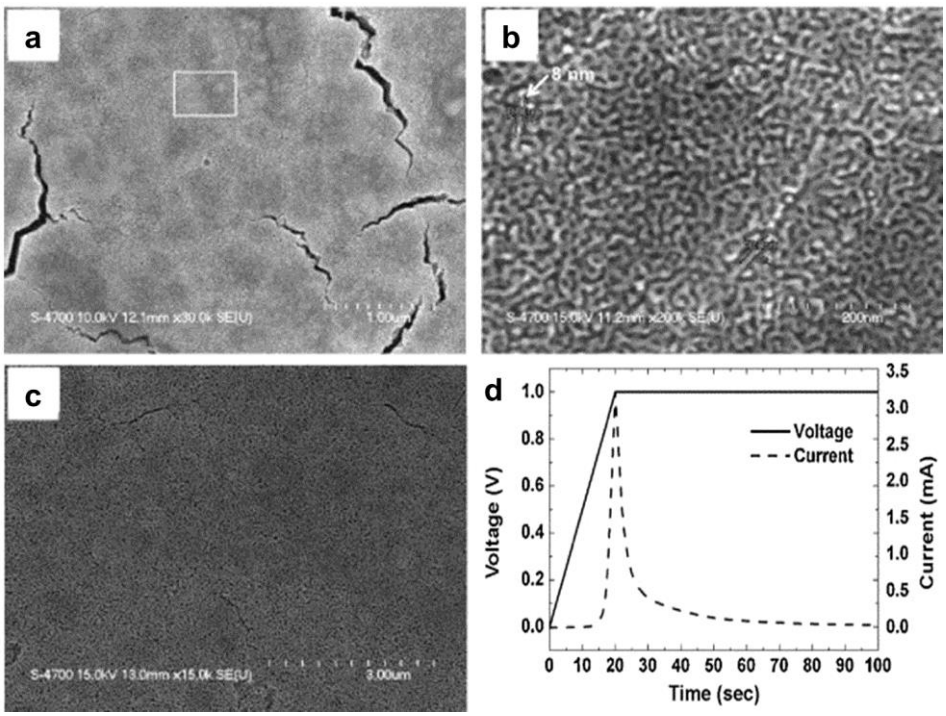

Figure 1.3. SEM images of nanoporous Au structure obtained by electrochemical dealloying process of 2D Au-Ag alloy thin films. (a) Surface morphology of a nanoporous Au thin film (Au 30 at%) annealed at 400 °C for 2 h in Ar. The electrochemical dealloying was performed in 0.8 M $HClO_4$ at 1 V with stepwise increase of applied voltage (50 $mV \cdot s^{-1}$). (b) An enlarged SEM image of white box part in (a). The resulting nanoporous Au structure showed extremely reduced ligament sizes. (c) Surface morphology of a nanoporous Au thin film (Au 21.5 at%). The electrochemical dealloying was performed in 0.8 M $HClO_4$ at 1 V with stepwise increase of applied voltage (12.5 $mV \cdot s^{-1}$). (d) Plot of the current and voltage applied during electrochemical dealloying as a function of time. Images were reproduced with permission from ref 62, Copyright 2009 Elsevier.

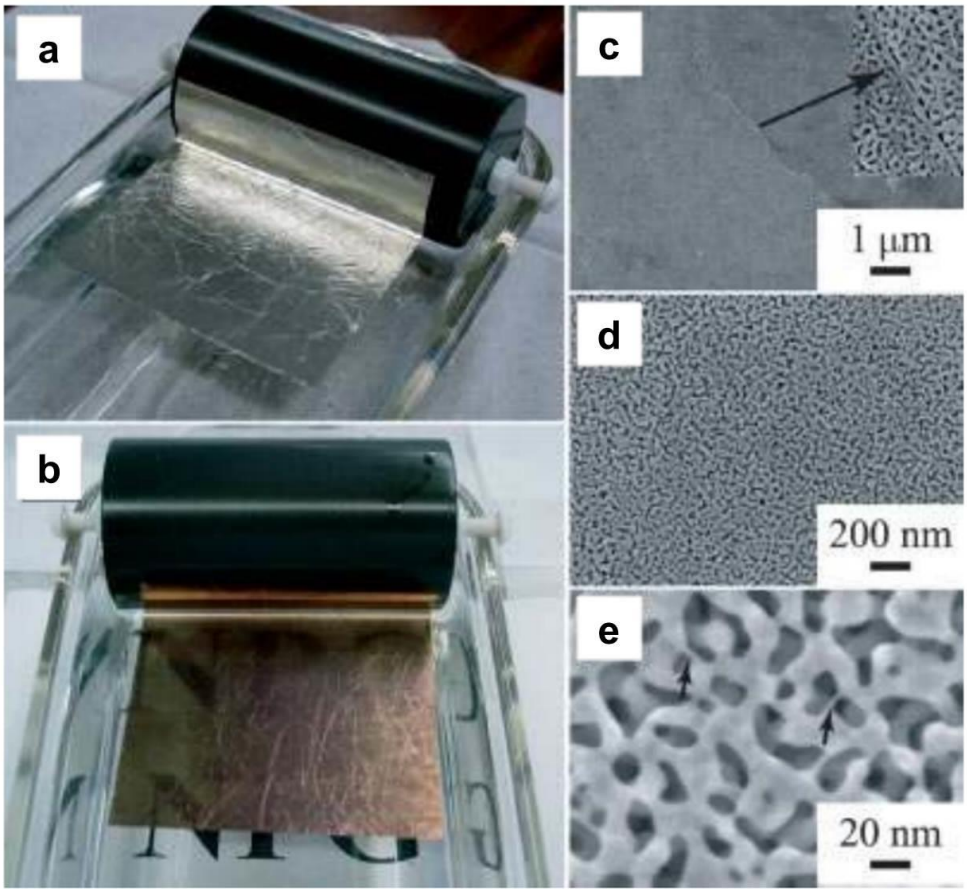

Figure 1.4. Free-standing nanoporous Au structure obtained from a chemical dealloying process using a commercially available 12 carat white-gold decorative leaf (Au-Ag alloys of which composition is 1:1 by weight). (a, b) Optical images of white-Au leaf before (a) and after (b) dealloying in HNO_3 for 15 min. (c-e) SEM images of the chemically dealloyed free-standing nanoporous Au leaf. The inset image in (c) indicates a solid grain boundary. Black arrows in (e) indicate very thin Au ligaments of which diameters are smaller than 2 nm. Images were reproduced with permission from ref 29, Copyright 2004 WILEY-VCH.

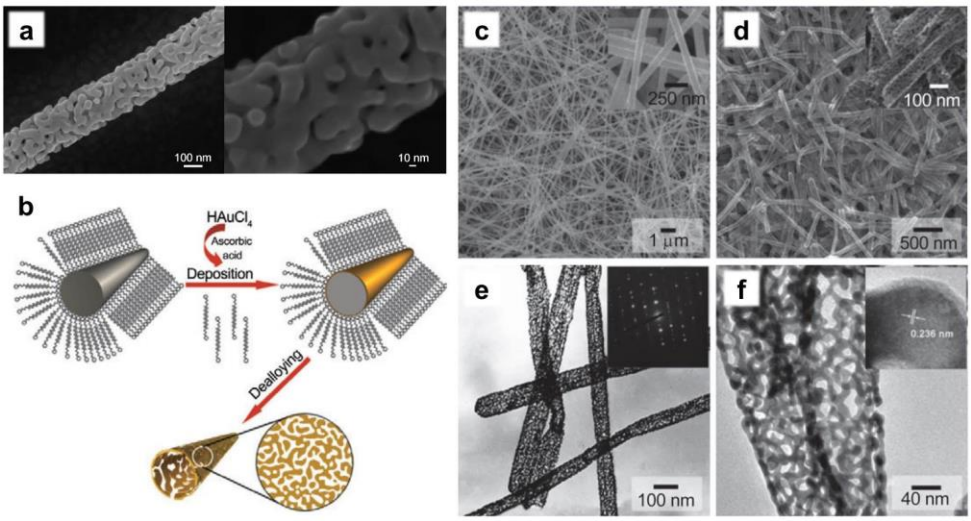

Figure 1.5. Template-based synthesis of nanoporous Au nanowires/nanotubes prepared by chemical dealloying process. (a) SEM images of nanoporous Au nanowire obtained from the etching of $Au_{0.32}Ag_{0.68}$ alloy nanowires. The starting material, Au-Ag alloy nanowire, is prepared by using an anodic aluminum oxide (AAO) template. (b) Schematic illustration of the synthesis process of Au-Ag alloy nanoporous nanotube (NPNT). The Ag nanowire plays a role as a template for preparation of hollow-type nanoporous structure. (c-f) SEM and TEM images of Ag nanowire template (c) and Au-Ag NPNTs (d-f). The insets of each images indicates a higher magnification images, selected-area electron diffraction pattern, and high-resolution TEM image. Images were reproduced with permission from (a) ref 66, Copyright 2003 American Chemical Society; (b-f) ref 69, Copyright 2009 Tsinghua University Press and Springer.

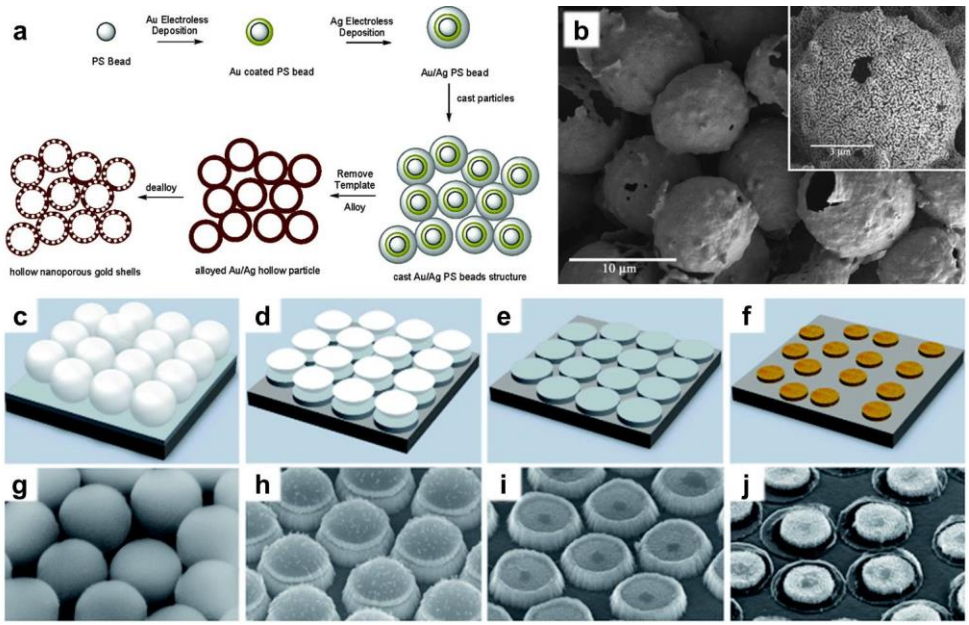

Figure 1.6. Polystyrene (PS) template-based synthesis of hierarchical porous Au shells and disks. (a) Schematic illustration of the synthesis process of hollow nanoporous Au shells. (b) SEM image of hollow $Au_{0.15}Ag_{0.85}$ alloy shells. Inset shows SEM image of dealloyed nanoporous Au shell. (c-j) Schematic illustration of the fabrication process of nanoporous Au disks (c-f) and SEM images at each process step (g-j). The fabrication of nanoporous Au disks is performed by following process: (c) formation of a monolayer of PS beads on an alloy-coated Si substrate; (d) O_2 plasma shrinkage of the PS beads and Ar sputter etching to form isolated alloy disk; (e) selective dissolution of PS beads by chloroform; and (f) formation of nanoporous Au disks by dealloying. Images were reproduced with permission from (a, b) ref 70, Copyright 2007 American Chemical Society; (c-j) ref 71, Copyright 2014 Royal Society of Chemistry.

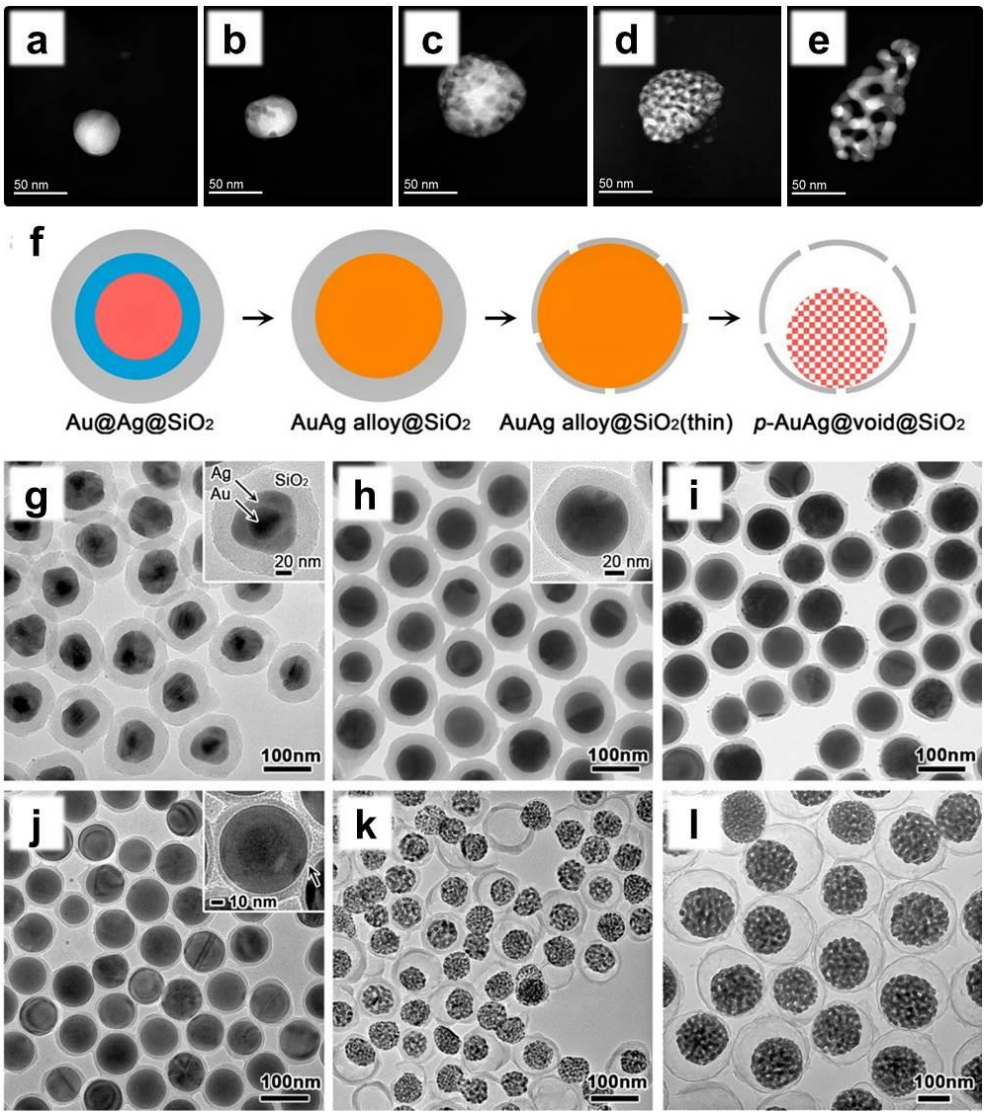

Figure 1.7. Template-free fabrication of nanoporous Au nanoparticles using wet-chemistry. (a-e) Representative high-angle annular dark-field images of $Au_{0.73}Au_{0.27}$ nanoparticles dealloyed at the indicated potential, time: (a) undealloyed particle; (b) 0.54 V, 6 h; (c) 0.74 V, 6 V; (d) 0.94 V, 2 min; and (e) 0.94 V, 6 h. (f-l) Synthesis of nanoporous SiO_2/Au-Ag alloy yolk/shell nanoparticles by a dealloying method. (f) Schematic illustration of the synthesis route for formation of nanoporous nanoparticles. (g-l) TEM images of the products during whole synthesis route: (g) Au@Ag@SiO_2 nanoparticles; (h-j) AuAg

alloy@SiO_2 nanoparticles with different silica shell thickness (thick to thin); (k) nanoporous AuAg@void@SiO_2 nanoparticles dealloyed at 0 °C (~61 nm of the size). Black arrow in the inset of (j) shows a defect in the thin silica shell. (l) Nanoporous AuAg@void@SiO_2 nanoparticles contain large size of nanoporous Au-Ag alloy nanoparticle (~160 nm). Images were reproduced with permission from (a-e) ref 75, Copyright 2014 American Chemical Society; (f-l) ref 76, Copyright 2016 American Chemical Society.

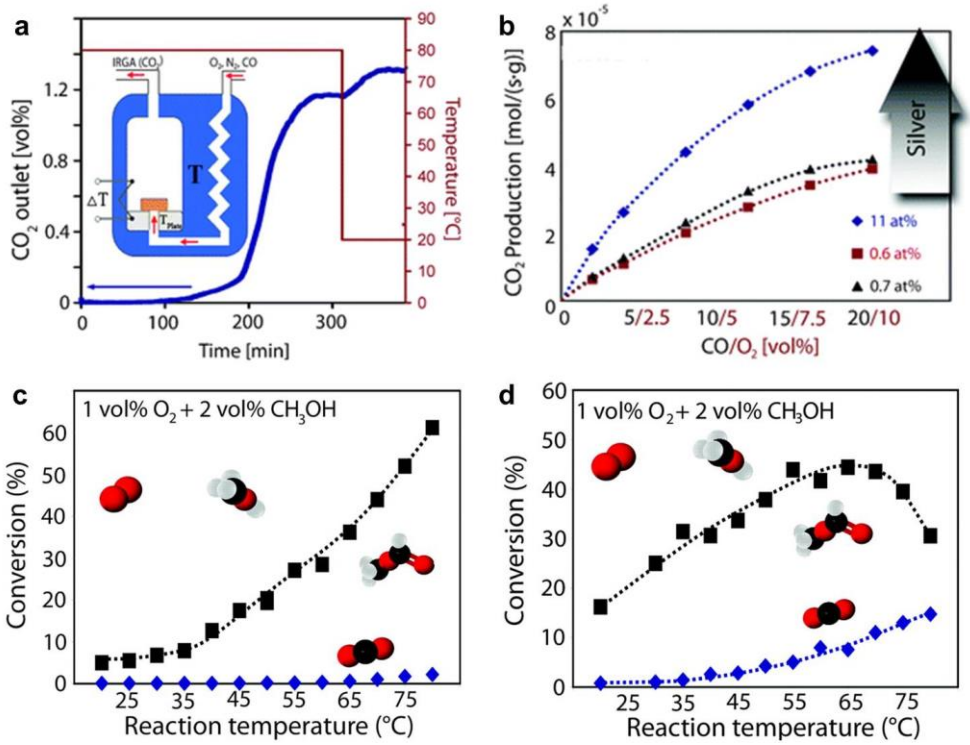

Figure 1.8. Catalytic oxidation of carbon monoxoide (CO) and methanol on nanoporous Au structure. (a, b) Catalytic oxidation of CO on nanoporous Au. (a) Catalytic activity (CO oxidation) of nanoporous Au structure as a function of reaction time. Inset indicates a continuous flow reactor for the CO oxidation. (b) CO oxidation activity of nanoporous Au containing different amount of Ag-residues. In case of nanoporous Au containing high amount of Ag-residue (11.4 at%, blue diamonds), the catalytic activity is increased by a factor of two in comparison with nanoporous Au containing 0.6 at% (red squares) and 0.7 at% (black triangles) of Ag-residues, respectively. (c, d) Catalytic oxidation of methanol on nanoporous Au. (c) Catalytic activity of methanol on nanoporous Au containing different composition of Ag-residues; (c) <1.0 at% and (d) 2.5 at%. Black squares and blue diamonds refer conversion of methanol to methyl formate (partial oxidation) and carbon dioxide (total oxidation), respectively. The catalytic reaction increases with temperature. When the composition of Ag-residue within the nanoporous Au, the methanol is oxidized to methyl formate with nearly 100%

selectivity; however, the undesired side product (carbon dioxide) is detected in case of nanoporous Au containing the relatively higher amount of Ag-residue, showing low selectivity in catalytic reaction. Images were reproduced with permission from (a, b) ref 21, Copyright 2010 Royal Society of Chemistry; (c, d) ref 8, Copyright 2010 American Association for the Advancement of Science.

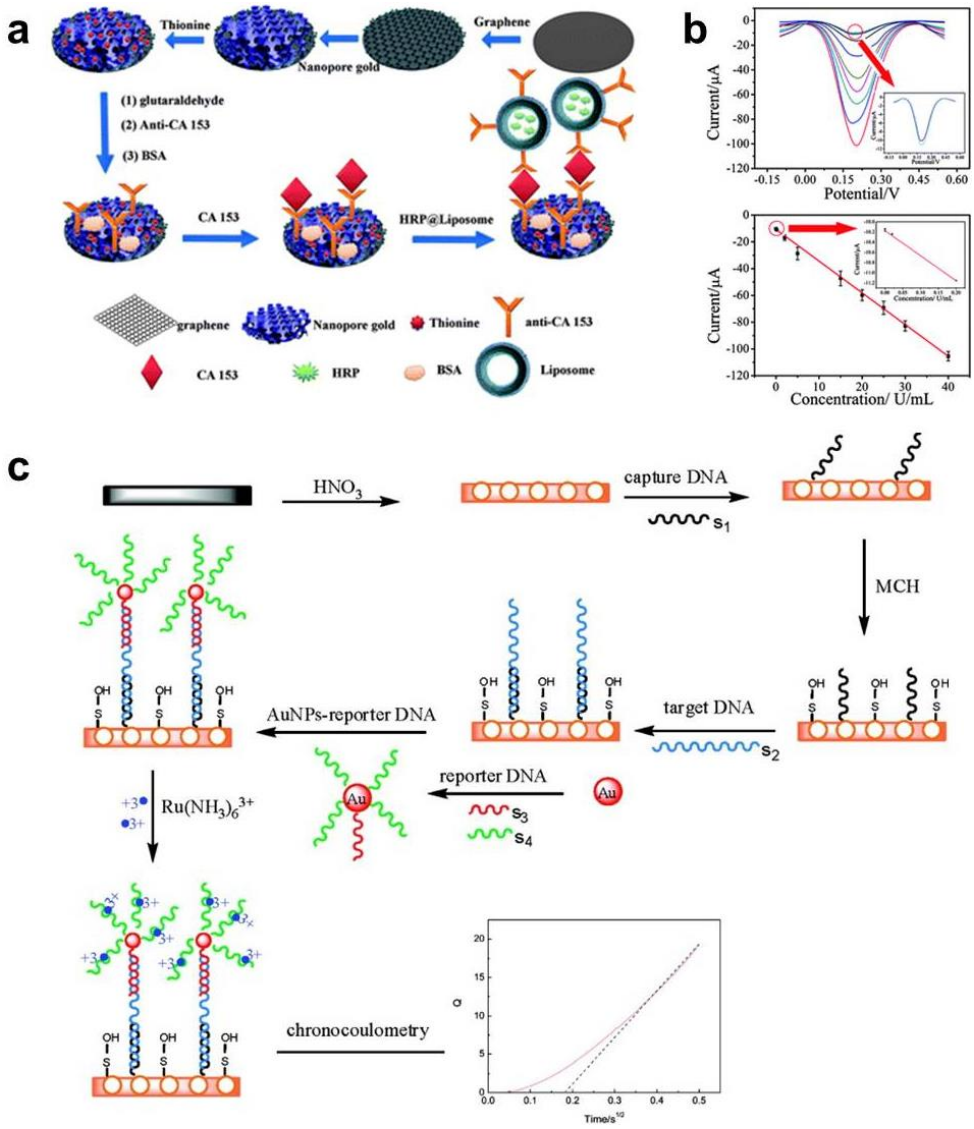

Figure 1.9. Nanoporous Au substrate-based electrochemical sensor for detection of antigen and DNA. (a) Schematic illustration of the immunosensing of cancer antigen 15-3 (CA 15-3). (b) Differential pulse voltammetric response of the immunosensor with different target concentration (top), and calibration curve for CA 15-3 immunoassay (bottom). (c) Schematic illustration of the chronocoulometric determination of DNA hybridization through two steps of amplification. Images were reproduced with permission from (a, b) ref 101,

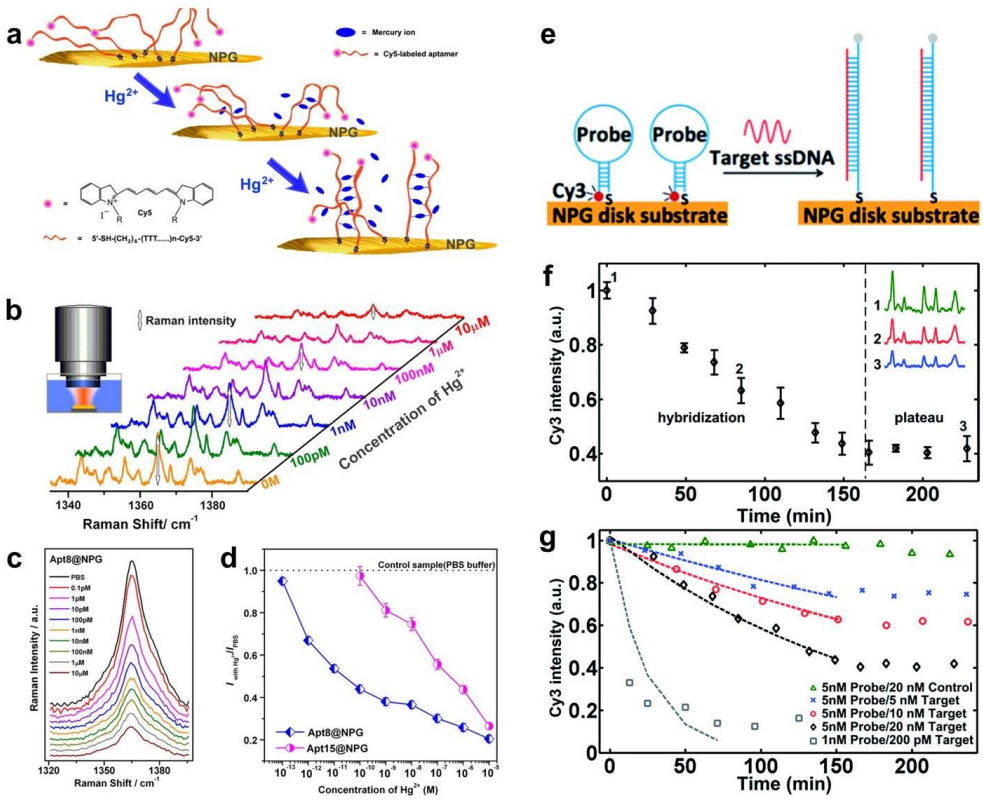

Figure 1.10. Nanoporous Au substrate-based optical sensor for detection of mercury ion (Hg^{2+}) and DNA. (a) Schematic illustration of SERS sensing of Hg^{2+} using the aptamer-modified nanoporous Au structure. (b) Quantitative SERS spectra with different concentration of Hg^{2+}. (c) Mercury ion concentration-dependent SERS spectra of the sensing platform by measuring the most prominent peak of Cy5, at 1365 cm^{-1}. (d) The normalized SERS intensity at 1365 cm^{-1} with different concentration of Hg^{2+} and with PBS buffer only. (e) Schematic illustration of SERS sensing of DNA based on the molecular sentinel (MS) oligonucleotides-immobilized nanoporous Au structure. (f, g) *In situ* monitoring of DNA hybridization using SERS line-spectra in certain conditions: (f) 5 nM MS probe with 20 nm target, (g) 5 nM MS probe with 5, 10, 20 nM target (blue crosses, red circles, and black diamonds) and 20 nM non-complementary DNA (green triangles), and 1 nM MS probe with 200 pM target (gray squares). Images were

reproduced with permission from (a-d) ref 120, Copyright 2013 American Chemical Society; (e-g) ref 9, Copyright 2014 Royal Society of Chemistry.

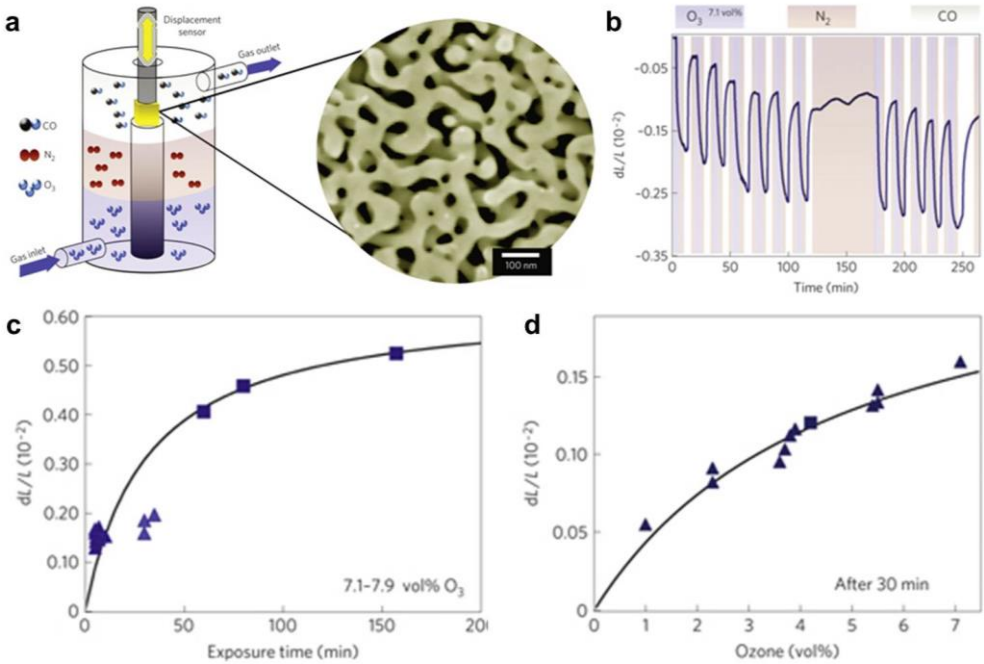

Figure 1.11. Performance of a surface-chemistry-driven actuation based on the nanoporous Au structure. (a) Schematic illustration of the nanoporous Au structure-based actuator in a viscous-flow reactor. (b) Strain changes of nanoporous Au-based actuator as a function of time after exposed to a mixture of ~7% ozone (O_3) in oxygen (O_2) and pure carbon monoxide (CO). When O_3 is exposed the actuator is contracted, whereas it is restored to the original sample dimension in the presence of CO. (c) Changes in an elastic strain of actuator as a function of O_3 exposure time for a mixture of ~7% O_3 in O_2. (d) Changes in an elastic strain of actuator as a function of O_3 concentration for 30 min exposure. From different samples (squares and triangles), it is clearly shown a good reproducibility. Images were reproduced with permission from ref 10, Copyright 2008 Nature Publishing Group.

Chapter 2

Dealloying-Based Synthesis and Highly Catalytic Properties of Au Core/Porous Shell Nanoparticles

2.1. Introduction

Noble metal nanoparticles (NPs) have received enormous attention because of their unique, useful chemical and physical properties and fascinating applications in a variety of fields including catalysis,[1,2] plasmonics,[3,4] surface-enhanced Raman scattering (SERS),[5-7] drug delivery,[8] biomedical imaging/diagnostics,[9] and sensing.[10,11] In particular, Au NPs have been widely studied and applied due to their chemical inertness, high surface reactivity, precisely controllable sizes and morphologies, diverse surface functionalization, tunable plasmonic properties, and photothermal effect.[12,13] Since the high reactivity of Au nanoclusters for CO oxidation and propylene epoxidation has been demonstrated,[14] Au-based heterogeneous catalysts have been heavily investigated, particularly for low-temperature CO oxidation, epoxidation, water-gas shift reaction, and selective oxidation.[15] Recently, investigations have been extended to study of the size- or structure-dependent catalytic performance of Au nanostructures,[16,17] and their synergistic effect-based superior catalytic performances by forming metal-metal oxide nanocomposites have been reported.[18-20]

It is well known that smaller NPs (<10 nm) show higher catalytic activity due to their high surface-to-volume ratio and the low-coordination number of the surface atoms, which induces high surface reactivity.21 In accordance with the size dependent catalytic performance,[22,23] many studies have focused on investigating the catalytic activity of small Au NPs. Small NPs, however, exhibit severe limitations such as difficulty in isolation (and purification) after use, incongruity when tuning optical/physicochemical properties, and vulnerability to structural modification.

Because of the structural drawbacks, small Au NPs also suffer from low shape stability due to the low melting point of Au, and, hence, their catalytic lifetimes are generally short.[24] For these reasons, it would be beneficial if one could use

relatively large NPs for catalytic reactions while minimizing the effects of size mentioned above. To generate a catalytically active site, enhanced surface reactivity, and a large surface area in larger NPs, researchers have focused on the synthesis of porous or hollow nanostructures because these structures can provide a large surface/volume ratio and a catalytically active surface.[25,26] Typically, the galvanic replacement reaction has been widely employed to synthesize porous/hollow nanostructures; however, the structures generated by this method did not greatly enhance catalytic performance because the reduced atoms only occupy the outermost region of a nanostructure due to the nature of the replacement reaction mechanism,[27,28] which means catalytically active metal atoms cannot be uniformly distributed through the entire region.

Herein, we present a facile and straightforward synthetic strategy for controlling and forming Au core/porous shell nanoparticles (CPS NPs) by a selective dealloying (Ag-etching process) process of Au/Au-Ag core/alloy shell NPs (CAS NPs) (Figure 2.1). The shell of CPS NPs contains networked thin ligaments, catalytically-active surface defects and ultra-high porosity throughout the shell. Using the robust CPS NPs, we investigated the porosity-dependent catalytic activity with a well-known chemistry [the reduction of 4-nitrophenol (4-NP) by sodium borohydride ($NaBH_4$) in this case]. We also compared the catalytic performance of the highly porous CPS NPs to galvanic replacement-based Au core/hollow shell nanoparticles (CHS NPs) with the same amount of metal precursors, and it was shown that the CPS NPs have the best catalytic activity among the reported porous/hollow Au nanostructures. Finally, we showed that the photothermal activation of the CPS NPs can further enhance their catalytic reactivity.

2.2. Experimental Section

Reagents and materials

Gold nanoparticles (diameter = 40 nm) were purchased from Ted Pella, Inc. (Redding, CA, USA). Gold(III) chloride trihydrate ($HAuCl_4 \cdot 3H_2O$, ≥99.9%), silver nitrate ($AgNO_3$, 99.9999%), polyvinylpyrrolidone (PVP, Mw ≈ 40000), ammonium hydroxide solution (NH_4OH, 28.0-30.0% NH_3 basis), L-ascorbic acid (AA, ≥99.0%), iron(III) nitrate nonahydrate ($Fe(NO_3)_3 \cdot 9H_2O$, ≥98.0%), trisodium citrate dihydrate ($Na_3C_6H_5O_7 \cdot 2H_2O$, meets USP testing specifications), and 4-nitrophenol (4-NP, ≥99.0%) were purchased from Sigma-Aldrich (St Louis, MO, USA). Sodium borohydride ($NaBH_4$, 97.0%) was purchased from DAEJUNG Chemicals & Metals Co. (Siheung, Gyeonggi, Korea), and nitric acid (HNO_3, 60.0%) was purchased from Samchun Pure Chemical Co. (Pyungtack, Gyeonggi, Korea). All the chemical reagents were used as received without further purification. Nanopure water (Millipore, Milli-Q 18.2 MΩ·cm) was used throughout the experiments.

Synthesis of Au/Au-Ag core/alloy shell nanoparticles

The Ag/Au molar ratio in the shell region was adjusted by changing the number of Ag atoms added to a constant number of Au atoms in the synthesis. Typically, 50 pM solution of Au nanoparticles (500 μL) and 2 wt% PVP solution (500 μL) were gently mixed, then 0.5 mM solution of $AgNO_3$ (250, 750, or 1750 μL, according to the desired Ag/Au ratio) was injected. Next, NH_4OH solution (50 μL) and 0.5 mM $HAuCl_4$ solution (250 μL) were added to the mixture, then 10 mM AA solution (500 μL) was immediately injected with gentle shaking. The resulting mixture was mildly shaken for 1 h at room temperature. Finally, the solution was washed twice with distilled water by centrifugation at 6000 rpm for 10 min, and redispersed in distilled water.

Synthesis of Au core/porous shell nanoparticles

CPS NPs were synthesized by introducing $Fe(NO_3)_3$ as a Ag-etchant into the prepared CAS NPs. Typically, 12.5 pM solution of the CAS NPs (425 μL) was mixed with 2 wt% PVP solution (425 μL), then 50 mM $Fe(NO_3)_3$ solution (50 μL) was injected with gentle shaking. The resulting mixture was mildly shaken for 30 min at room temperature, then washed twice with distilled water by centrifugation at 6000 rpm for 10 min, and redispersed in distilled water.

Synthesis of galvanic replacement-based Au core/hollow shell nanoparticles (CHS NPs)

CHS NPs were synthesized by a modified galvanic replacement reaction.[27] Typically, 50 pM solution of Au nanoparticles (500 μL), 2 wt% PVP solution (500 μL), 0.5 mM $AgNO_3$ solution (1750 μL), and NH_4OH solution (50 μL) were added sequentially to the reaction vessel with gentle shaking. Then, 10 mM AA solution (500 μL) was injected immediately into the reaction mixture. After 1 h, the resulting mixture (Au/Ag core/shell nanoparticles) was washed twice with distilled water by centrifugation at 6000 rpm for 10 min, and redispersed in distilled water for further use. Subsequently, 12.5 pM solution of the as-synthesized Au/Ag core/shell nanoparticles (1.6 mL) and 2 wt% PVP solution (1 mL) were diluted with distilled water (7 mL) in a round-bottomed flask and heated to 80 °C. Then, 0.1 mM $HAuCl_4$ solution (1 mL) was added dropwise to the flask via a syringe pump (Legato 110, KD Scientific) at a rate of 10 $mL \cdot h^{-1}$ under magnetic stirring. After the addition of $HAuCl_4$ was complete, the resulting solution was heated for 10 min until the color of the solution was stable, and the reaction was cooled to room temperature under ambient conditions. Finally, the resulting solution was washed twice with distilled water by centrifugation at 6000 rpm for 10 min, and redispersed in distilled water.

Synthesis of Au-Ag alloy nanoparticles

We synthesized Au-Ag alloy nanoparticles based on the following literature procedures with a minor modification.[31] Typically, a solution containing 18.5 mL distilled water and 0.5 mM $AgNO_3$ aqueous solution was boiled at 100 °C for 10 min under magnetic stirring, 0.5 mM $HAuCl_4$ aqueous solution was then added to the mixture, and the resulting solution was boiled for 10 min. In this step, we adjusted the Au/Ag ratio of Au-Ag alloy nanoparticles by controlling the added volume of precursors (0.25 mL of $AgNO_3$ and 0.25 mL of $HAuCl_4$ solution for $Au_{50}Ag_{50}$ alloy nanoparticles; 0.375 mL of $AgNO_3$ and 0.125 mL of $HAuCl_4$ solution for $Au_{25}Ag_{75}$ alloy nanoparticles). Subsequently, freshly prepared 1 wt% trisodium citrate dihydrate solution (1 mL) was injected, and the resulting mixture was boiled for 30 min additionally. Finally, the solution was cooled to room temperature under ambient condition, and washed twice with distilled water by centrifugation at 7000 rpm for 10 min.

Dealloying reaction of Au-Ag alloy nanoparticles

Dealloying reaction was carried out by introducing $Fe(NO_3)_3$ solution and HNO_3 solution as a Ag etchant into the prepared Au-Ag alloy nanoparticles. In a typical synthesis, the Au-Ag alloy nanoparticle solution (250 μL) was mixed with 2 wt% PVP solution (250 μL), then 50 mM $Fe(NO_3)_3$ aqueous solution (25, 100, and 500 μL) or HNO_3 solution (60.0 %, 100 μL) was injected with gentle shaking. The resulting solution was mildly shaken for 30 min at room temperature, then washed twice with distilled water by centrifugation at 7000 rpm for 10 min, and redispersed in distilled water.

Catalytic reaction studies

The reduction of 4-NP by $NaBH_4$ was used as a model system to evaluate the catalytic activity of the as-synthesized nanocatalysts. Typically, distilled water (1.0 mL) was mixed with 0.4 mM 4-NP solution (0.75 mL) in a quartz cuvette, and a freshly prepared 480 mM $NaBH_4$ solution (0.25 mL) was quickly added. Finally, the nanocatalyst (0.5 mL; 6.25 pM) was injected rapidly into the system. In this system, the final concentrations of 4-NP and $NaBH_4$ were 0.12 mM and 48 mM, respectively. The UV-Vis spectrum was continuously recorded as a function of time to monitor the decrease of the extinction intensity at λ = 400 nm, which indicates the reduction of 4-NP to 4-AP. The change of extinction intensity was directly estimated by calculating the ratio of extinction at each time point ($\boldsymbol{A_t}$) relative to its initial value ($\boldsymbol{A_0}$) and, for accuracy, all extinction intensities were compensated by subtracting the natural extinction intensity of the appropriate nanocatalyst in solution.

Characterization

The morphology of the samples was characterized by transmission electron microscopy (TEM; JEM-2100, JEOL) and high-resolution transmission electron microscopy (HR-TEM; JEM-3000F, JEOL). Elemental mapping and line-scan profile were performed by energy-dispersive X-ray spectroscopy (EDX; INCA, Oxford Instruments) coupled with HR-TEM. The samples for the above characterization were prepared by dropping the compound to be analyzed onto a formvar/carbon-coated copper grid (Ted Pella, Inc., Redding, CA, USA). The surface states of the nanocatalysts were measured by X-ray photoelectron spectroscopy (XPS; SIGMA PROBE, Thermo Scientific) with a monochromatic Al X-ray source. The UV-Vis spectra were obtained with a UV-Vis spectrophotometer (HP 8453, Agilent Technologies). To monitor the time-dependent UV-Vis spectral

changes, we preset the cycle time as 1 s under the kinetics mode during the formation of Au/Au-Ag core/alloy shell NPs. The same technique was also applied to monitor the catalytic reaction by presetting 10 or 30 s as the cycle times.

2.3. Results and Discussion

Synthesis of Au/Au-Ag core/alloy shell nanoparticles

First, we introduced Au nanoparticles (40 nm in diameter) as a core and formed the Au-Ag alloy shell on the core. We performed a co-reduction process by simultaneous reduction of $HAuCl_4$ and $AgNO_3$ on the Au NPs to synthesize the CAS NPs. The Ag/Au composition in the shell region can be adjusted by controlling the amount of added Ag while keeping the amount of Au constant (see details in Experimental section). It should be noted that the presence of the Au core is necessary to form highly porous, stable nanostructures in a high yield. Without the Au core resulting in small-size nanostructures, Ag atoms in the alloy particles were not efficiently etched away (Figure 2.2a-d), and it was not possible to form highly porous Au NPs in a high yield. In addition, the UV-Vis spectra were not affected even after the amount of Ag-etchant was largely increased (Figure 2.2e and f). According to the reported literature,[29-31] for the Au-Ag alloy NPs usually synthesized by sub-10 nm or up to 20 nm in their size, there are not sufficient volumes to form porous structures after the dealloying processes. In Figure 2.2, the Ag-etched Au-Ag alloy NPs do not show highly porous structures. We assume that this comes from an insufficient volume to form porous structures and high surface tension or pressure resulting in volume shrinkage during surface diffusion and reorganization of Au atoms (the Au atoms localized in a small volume tend to agglomerate by forming clusters rather than ligament structures). For this reason, the relatively small-sized alloy nanoparticles could not generate highly porous structures from dealloying reactions. When a stronger Ag-etchant was used, unstable nanostructures were formed in an uncontrollable fashion, which means the rapid dealloying did not give sufficient time for the diffusion of Au atoms to form stable Au nanostructures. The fast and uncontrollable reaction results in collapsed, unstable dealloyed nanostructures (Figure 2.2g and h).

Figure 2.3a-c show the morphology and elemental distribution of CAS NPs obtained at different Ag/Au ratios: 1, 3, and 7. As the Ag/Au ratio increased from 1 to 3 to 7, the average size of each NP increased to 68.0, 83.2, and 106.6 nm for CAS(1), CAS(3), and CAS(7) NPs, respectively (the number in the parenthesis represents a Ag/Au ratio in the shell region of CAS NPs), and the atomic compositions of the shell regions were estimated as $Au_{48.2}Ag_{51.8}$, $Au_{27.9}Ag_{72.1}$, and $Au_{13.3}Ag_{86.7}$ for CAS(1), CAS(3), and CAS(7) NPs, respectively. The synthetic yield for CAS NPs was >90% (Figure 2.4). The energy-dispersive X-ray (EDX) elemental mapping clearly shows the chemical distribution of Ag and Au in the shell region (Figure 2.3a-c, black background). In general, Au and Ag atoms were well distributed throughout the shell region rather than forming largely localized clusters indicated by their close lattice constants: 0.408 nm for Au and 0.409 nm for Ag;[32] however, in the case of the lowest Ag/Au ratio, the Au atoms formed a relatively thick wall at the outermost shell region, and the proportion of Au at the outermost shell region decreased as the Ag/Au ratio increased. To examine this phenomenon in more detail, we acquired EDX line-scan profiles across the alloy shell region by integrating the X-ray intensity of Au-Lα and Ag-Lα (Figure 2.3a-c, right). In the case of CAS(1) NPs, Au atoms were predominantly present near the shell surface and the Au/Ag ratio rapidly increased toward the shell surface, indicating a relatively thick Au shell at the outermost region. On the other hand, in CAS(7) NPs, Au and Ag atoms were more evenly distributed over the entire shell region compared to CAS(1) and CAS(3) NPs. Basically, the Au precursor is reduced slightly faster than the Ag precursor due to a high standard reduction potential ($AuCl_4^-$/Au = 0.99 V and Ag^+/Ag = 0.8 V versus SHE);[33] however, the reduction rate of the Ag precursor is somewhat increased by the higher affinity between Ag and the pyrrolidone groups of polyvinylpyrrolidone.[34,35] For this reason, the extinction peak was rapidly blue-shifted at the early stage of alloy shell formation indicating more reduction of the Ag atoms (and, simultaneously, less

reduction of the Au atoms). Then, the extinction peak gradually red-shifted, with increasing peak intensity, as thicker alloy shell structures were formed (Figure 2.5). When a small amount of Ag precursor was used during alloy shell formation, there was not sufficient area to make Au atoms disperse evenly, thus Au atoms form a thick Au wall in the shell region in the case of CAS(1) NPs. However, the Au atoms could be dispersed evenly through a large area of the shell region in the case of CAS(7) NPs when plenty of Ag precursor was used during the synthesis. Hence, we can easily control the distribution of a constant number of Au atoms within the alloy shell region by changing the Ag/Au ratio during alloy shell formation.

Dealloying-based synthesis and characterization of Au core/porous shell nanoparticles

To synthesize Au CPS NPs from CAS NPs, we introduced ferric nitrate into the as-synthesized CAS NPs to selectively remove Ag atoms. In entirely mixed bimetallic structures, less stable elements (silver in our case) are removed from the outermost surface, and stable elements (gold in our case) diffuse on the surface and interconnect with each other, forming clusters. By repeating this reaction from the outer to inner surface, less stable elements were continuously dissolved and the remaining stable elements form ligaments through the whole alloy region, thus fabricating a porous structure.[36] Analogously, our CAS NPs formed porous structures after the selective removal of Ag atoms (Figure 2.3d and 2.6). The CPS NPs were synthesized in >90% yield (Figure 2.3f). In particular, the porosity of the dealloyed particles varied with the initial Ag/Au ratio in the alloy shell region. When the Ag/Au ratio was high and more silver atoms were removed, many pores were formed and the evenly distributed Au atoms were interconnected with each other to fabricate thin ligaments through the whole shell region. For this reason, CPS(7) NPs had higher porosity and thinner ligaments (≤5 nm) than CPS(1) and

CPS(3) NPs, and showed a higher loading capacity over other CPS NPs [8.3 and 4.7 times higher than CPS(1) and CPS(3) NPs, respectively (Figure 2.7 and Table 2.1)]. The *d*-spacing of 0.235 nm for adjacent lattice fringes matched well with that of the (111) planes of a face-centered cubic (fcc) structure (Figure 2.3g, left), and the selected-area electron diffraction (SAED) pattern of CPS(7) NPs clearly shows a ring shape, which demonstrates polycrystallinity (Figure 2.3g, right). Particularly, stepped surface-like defects were shown at the surface of ligaments of CPS(7) NPs (Figure 2.3h). These surface defects could stem from the low-coordination number of surface atoms due to thin ligaments, and the presence of surface defects could enhance the catalytic performance of these nanostructures. We characterized the surface state of CPS(7) NPs using the XPS (Figure 2.8). The Au 4f scan shows a doublet at 87.0 and 83.3 eV separated by 3.7 eV, which indicates the presence of metallic Au (zero-valent Au) on the surface of porous nanostructures.[37] The result confirms that the metal ions were efficiently reduced during the synthetic process, and similar XPS results were reported for other porous nanostructures.[38-40]

In addition, two distinct extinction peaks were clearly seen as the porous structure formed (Figure 2.9a-c). In the case of CAS NPs, the UV-Vis spectra showed one extinction peak around λ = 540 nm (λ = 538, 540, and 551 nm for CAS(1), CAS(3), and CAS(7) NPs, respectively); however, a new extinction peak appeared around the near-IR region after Ag etching (λ = 810, 852, and 968 nm for CPS(1), CPS(3), and CPS(7) NPs, respectively), indicating the formation of porous and hollow structures. Interestingly, the extinction peak around the near-IR region became dominant and shifted toward the longer-wavelength region as the product had higher porosity. This evidence clearly demonstrates the formation of porous structures after the dealloying process and the creation of higher porosity (larger empty space) as the Au atoms interconnected and formed thin ligaments.

Next, we compared the final products from the dealloying reaction of CAS(7) NPs to the products from the galvanic replacement reaction of the Ag shell

[CHS(7) NPs]. As mentioned above, CPS(7) NPs showed thin, networked ligaments and had high porosity throughout the shell while the galvanic replacement reaction generated a hollow nanostructure with a thick shell, localized ligaments and much fewer pores (Figure 2.3d and e). Despite use of the same amount of precursor, the final products showed completely different distributions of the Au atoms in the shell region. In the case of the galvanic replacement reaction, most Au atoms were deposited near the outer shell region, forming a thick shell structure; however, in our system, the Au atoms dispersed evenly throughout the whole shell region, which generated thin ligaments and high porosity. In addition to the morphological differences, the UV-Vis spectra also differed (Figure 2.9d). Unlike the two distinct extinction peaks seen in the spectrum of CPS(7) NPs, only one broad peak near λ = 640 nm was observed in the spectrum of the hollow shell structure [CHS(7) NPs] from the galvanic replacement reaction. The clear difference in the spectra further shows the synthesized nanostructures with our approach and the galvanic replacement reaction have different porosities and Au-cluster morphologies.

Catalytic performance of core/alloy shell and core/porous shell nanoparticles

Among many techniques in evaluating the catalytic performance of nanostructures,[41-49] we used the reduction reaction of 4-nitrophenol (4-NP) to 4-aminophenol (4-AP) by $NaBH_4$ in the presence of nanocatalysts according to the Langmuir-Hinshelwood mechanism[50] as a model reaction using the UV-Vis spectrophotometer (Figure 2.10). We focused on the decrease of extinction of reactant (4-NP) at λ = 400 nm over time to monitor the chemical conversion and evaluate the catalytic performance of nanocatalysts. Figure 2.11 shows the catalytic reduction curve of 4-NP, which reacted at 26.0 °C in the presence of nanocatalysts,

and compares the catalytic conversion features between CAS and CPS NPs. Due to the large excess of $NaBH_4$ relative to 4-NP in our system ([$NaBH_4$]/[4-NP] = 400), we can assume that the concentration of $NaBH_4$ is constant during the reaction and the conversion reaction kinetics was dependent on 4-NP. We plotted the logarithm of relative extinction intensity at λ = 400 nm ($-\ln(\boldsymbol{A_t}/\boldsymbol{A_0})$) versus the reaction time (t) to calculate the conversion rate constant ($\boldsymbol{k}$) under pseudo-first-order kinetics [equation (1): $-\ln(\boldsymbol{A_t}/\boldsymbol{A_0}) = \boldsymbol{k}t$]. In this plot, the induction time ($\boldsymbol{t_{ind}}$), the amount of time until the conversion reaction is initiated by generating a surface-hydrogen species on the nanocatalyst, can be clearly seen and we directly calculated $\boldsymbol{k}$ from the slope of the plot after $\boldsymbol{t_{ind}}$. In Figure 2.11, all the porous shell nanostructures (CPS NPs) showed higher $\boldsymbol{k}$ values and shorter $\boldsymbol{t_{ind}}$ than their corresponding alloy form (CAS NPs). The CPS NPs with an extensively larger surface area could generate surface-hydrogen species faster, enhance collision efficiency between the nanocatalyst surface and the reactant, and facilitate better diffusion of the reactant 4-NP and product 4-AP inward/outward to the nanocatalysts during the conversion reaction than their alloy forms. Interestingly, the $\boldsymbol{k}$ values of CAS(1) and CPS(1) NPs were similar ($\boldsymbol{k}_{\mathrm{CAS(1)\ NPs}}$ = 0.202 $\mathrm{min^{-1}}$ and $\boldsymbol{k}_{\mathrm{CPS(1)\ NPs}}$ = 0.219 $\mathrm{min^{-1}}$). In the case of CAS(1) NPs, many Au atoms occupied the outermost shell surface, rather than being spread across the whole shell region, and this thick Au shell remained after Ag etching. With this structural configuration, the catalytic conversion occurred mainly at the thick outermost shell surface and the reactant was disturbed in order to penetrate toward the interior of the porous shell. Consequently, $\boldsymbol{k}$ was fairly consistent between alloy and porous structures. However, it should be noticed that CPS(1) showed a much faster induction time than CAS(1), and this could be mainly because CPS(1) NPs possessed higher surface-energy structures than CAS(1) NPs. In contrast, the $\boldsymbol{k}$ values differed significantly in the case of CAS(7) and CPS(7) NPs (nearly 6 times higher for CPS(7) NPs; $\boldsymbol{k}_{\mathrm{CAS(7)\ NPs}}$ = 0.124 $\mathrm{min^{-1}}$ and $\boldsymbol{k}_{\mathrm{CPS(7)\ NPs}}$ = 0.708 $\mathrm{min^{-1}}$), and the induction time was also significantly faster

for CPS(7) NPs. As mentioned above, the Au atoms in CAS(7) NPs were evenly distributed throughout the shell volume and the Ag-etched products showed higher porosity and had networked thin ligaments within the structure. In the case of CPS(7) NPs, this feature provides a remarkably large catalytic surface area and high-energy surface structures containing stepped surface-like defects, originating from the low-coordination number of surface atoms. Thus, the changes in conversion rate constant and induction time between the alloy and porous shell structures get larger as the Ag/Au ratio of CAS NPs increased from 1 to 3 to 7 (Figure 2.11d). We summarized each set of data in the Table 2.2.

Porosity and temperature-dependent catalytic properties of core/porous shell nanoparticles

Additionally, we examined the porosity and temperature-dependent catalytic performance using CPS(1), CPS(3), and CPS(7) NPs at 13.5, 26.0, and 44.0 °C, respectively (Figure 2.12). Although they contain the same number of Au atoms, the conversion reaction occurred earlier (short $\boldsymbol{t_{ind}}$) and faster (high $\boldsymbol{k}$) as the porosity of the shell region increased. As expected, the conversion reaction also occurred earlier and faster at increased reaction temperatures due to the higher collision frequency (Table 2.2). Based on the temperature-dependent catalytic activity of our particles, we plotted ln $\boldsymbol{k}$ versus one thousand times the inverse of the absolute temperature (1000/T) to calculate the activation energy ($\boldsymbol{E_a}$) and the pre-exponential factor ($\boldsymbol{A}$) from the Arrhenius equation [equation (2): $\ln \boldsymbol{k} = \ln \boldsymbol{A} - \boldsymbol{E_a}/RT$], where R is the gas constant; Figure 2.13a. We calculated the activation energy from the slope ($-\boldsymbol{E_a}/R$) of the linear fit. Noticeably, the $\boldsymbol{E_a}$ value with CPS(7) NPs (22.69 ± 1.35 kJ mol^{-1}) was much lower than with CPS(1) (38.78 ± 1.46 kJ mol^{-1}) and CPS(3) NPs (32.63 ± 1.68 kJ mol^{-1}), and the lower $\boldsymbol{E_a}$ with CPS(7) NPs can be attributed to the larger surface area, high-energy surface structures, surface

defects of thin ligaments, and higher porosity throughout the overall shell region. We would like to point out that the $\boldsymbol{E_a}$ value with CPS(7) NPs is lower than the previously reported results in the literature with Au-based nanostructures.[26,51-53] Although the overall size of CPS(7) NPs is relatively large, they show excellent catalytic activity in terms of the size effect because of the very thin interconnecting ligaments throughout the shell region, which acts like small nanoparticles. In addition, the $\boldsymbol{A}$ value (calculated from the intercept of the linear fit, Figure 2.13a) obtained from equation (2) showed the same tendency as $\boldsymbol{E_a}$: the lowest values for CPS(7) NPs and the highest values for CPS(1) NPs. We have summarized each set of data in the Table 2.3.

Fundamentally, $\boldsymbol{k}$ is determined by considering the values of both $\boldsymbol{A}$ and $\boldsymbol{E_a}$. It can be seen that either increasing $\boldsymbol{A}$ or decreasing $\boldsymbol{E_a}$ will result in an increased rate of the conversion reaction. This leads to a concomitant change in the $\boldsymbol{E_a}$ and $\boldsymbol{A}$ values for the overall reaction, which acts to compensate factors influencing $\boldsymbol{k}$.[54] In particular, this effect can be shown by the linear relationship between ln $\boldsymbol{A}$ and $\boldsymbol{E_a}$, which is referred to as the compensation effect or the Meyer-Neldel rule.[55] Figure 2.13b shows the plot of ln $\boldsymbol{A}$ versus $\boldsymbol{E_a}$ obtained for our catalytic system. It clearly shows a linear relationship between ln $\boldsymbol{A}$ and $\boldsymbol{E_a}$, which means that our system displays the compensation effect,[56,57] *i.e.*, the catalytic conversion reaction takes place validly with our nanocatalysts. For the quantitative analysis of the catalytic activity, we calculated the turnover frequency ($TOF_{50\%}$) values of the as-synthesized nanocatalysts (Figure 2.13c). The $TOF_{50\%}$ values were defined as the moles of reduced 4-NP per mole of Au atoms in the shell region per hour when the catalytic reaction reached 50% after the reaction initiated. The CPS(7) NPs showed the highest $TOF_{50\%}$ values (588.3 ± 7.48 h^{-1}) over other nanocatalysts; 182.0 ± 4.15 h^{-1} for CPS(1) NPs and 285.0 ± 2.49 h^{-1} for CPS(3) NPs. The results could be directly interpreted as porous shell morphology-dependent catalytic activity.

Photothermal catalytic enhancement

The plasmon-induced properties such as enhanced electromagnetic field, photothermal effect and hot-electron injection can affect the catalytic activities of nanostructures and have been extensively studied recently.[58-61] Once surface plasmon electrons of metallic nanostructures are excited with light, they follow the relaxation process by transferring their absorbed energy to the metallic lattice and the surrounding medium in the form of thermal energy, known as the photothermal effect, and the photothermal effect could enhance chemical reactivity.[62] We examined the photothermal effect-based enhancement in catalytic performance with our porous nanocatalysts (Figure 2.13d). Solution temperature rapidly increased upon laser irradiation in the presence of CPS(7) NPs (Figure 2.13e). The reaction temperature differed about 6.2 °C (32.2 ± 0.64 °C with laser and 26.0 ± 0.17 °C without laser). Importantly, the reaction initiated earlier ($\boldsymbol{t}_{\mathbf{ind},\ \text{laser ON}}$ = 1.11 ± 0.01 min; $\boldsymbol{t}_{\mathbf{ind},\ \text{laser OFF}}$ = 1.73 ± 0.01 min) and proceeded faster ($\boldsymbol{k}_{\text{laser ON}}$ = 0.812 ± 0.014 min^{-1}; $\boldsymbol{k}_{\text{laser OFF}}$ = 0.708 ± 0.009 min^{-1}) under laser irradiation (Figure 2.13f). The laser-irradiated CPS(7) NPs [L-CPS(7) NPs] showed a 14.7% increase in the $\text{TOF}_{50\%}$ value (674.8 ± 11.63 h^{-1}) over the CPS(7) NPs without laser irradiation (Figure 2.13c). For CAS(7) NPs, no noticeable changes were observed with laser irradiation (Figure 2.14). It should be noticed that a very small part of a whole sample was activated with the laser beam, and particle concentration and other conditions were not optimized in this proof-of-concept experiment. The results, even without optimization, confirm that the catalytic performance of CPS(7) NPs can be further enhanced by using their photothermal property.

Comparison between Au nanocatalysts

Finally, we compared the catalytic activities of different Au nanocatalysts including CPS(7) NPs (Figure 2.3d, right) and galvanic replacement-based CHS(7)

NPs (Figure 2.3e). As shown in Figure 2.13a, $\boldsymbol{E_a}$ of CHS(7) NPs (41.45 ± 1.96 kJ mol^{-1}) is much higher than that of CPS(7) NPs (22.69 ± 1.35 kJ mol^{-1}), and the $\boldsymbol{k}$ value of CHS(7) NPs was significantly lower than that of CPS (7) NPs at varying reaction temperatures (Table 2.2). Furthermore, the CPS(7) NPs showed a two-fold higher $TOF_{50\%}$ value than CHS(7) NPs (Figure 2.13c and Table 2.3). These results suggest that the thicker outer layer, lack of ligaments and small, poorly distributed pores of CHS(7) NPs are unfavorable for an efficient conversion reaction and lead to insufficient diffusion of the reactant and product. When one includes the photothermal effect [L-CPS(7) NPs], the $\boldsymbol{k}$, $\boldsymbol{t_{ind}}$ and $TOF_{50\%}$ values were further improved [all these values were >2-fold improved over the CHS(7) NPs case]. We can conclude that the catalytic activities of CPS(7) NPs for the reaction of 4-NP to 4-AP by $NaBH_4$ is the best ever among the reported results with the same reaction.

2.4. Conclusions

We report the facile synthesis of Au-based porous shell nanoparticles by a highly controllable selective Ag-etching-based dealloying process from Au-Ag alloy shell nanostructures. It was shown that the porosity and ligament thickness of Ag-etched porous nanostructures could be controlled by changing the initial composition of Ag/Au in the alloy shell region. This dealloying method provides structures with more densely and uniformly distributed nanopores throughout than the conventional galvanic replacement method, and the Au core/porous shell nanostructures are more structurally robust and controllable than other porous/hollow nanostructures. The Ag-etched porous shell structures exhibited better catalytic activity than non-etched Au-Ag alloy shell structures, and, in particular, the porous shell structures containing larger pores and thinner ligaments exhibited excellent catalytic performance due to their large surface area and abundance of active sites as a result. Our porous nanocatalysts also showed better catalytic performances than other hollow/porous catalytic nanostructures obtained by the widely used galvanic replacement reaction. The photothermal property of the plasmonic CPS NPs can further boost the catalytic activity, and the Au CPS NPs are more catalytic than any other Au nanocatalysts with respect to induction time, rate constant, activation energy and turnover frequency. The results suggest that our synthetic strategy can control and generate highly porous, catalytically active nanostructures with densely and thoroughly distributed pores, and our method opens avenues for designing and synthesizing highly porous nanostructures and utilizing them as highly catalytic porous Au nanostructures in a straightforward and reliable manner. The porous nanostructures can be also applied in a variety of biomedical and photocatalytic applications.[63,64]

2.5. References

1. Gross, E.; Liu, J. H.-C.; Toste, F. D.; Somorjai, G. A. *Nat. Chem.* **2012**, *4*, 947.
2. Kang, S. W.; Lee, Y. W.; Park, Y.; Choi, B.-S.; Hong, J. W.; Park, K.-H.; Han, S. W. *ACS Nano* **2013**, *7*, 7945.
3. Prodan, E.; Radloff, C.; Halas, N. J.; Nordlander, P. *Science* **2003**, *302*, 419.
4. Halas, N. J.; Lal, S.; Chang, W. S.; Link, S.; Nordlander, P. *Chem. Rev.* **2011**, *111*, 3913.
5. Banholzer, M. J.; Millstone, J. E.; Qin, L.; Mirkin, C. A. *Chem. Soc. Rev.* **2008**, *37*, 885.
6. Ling, X. Y.; Yan, R.; Lo, S.; Hoang, D. T.; Liu, C.; Fardy, M. A.; Khan, S. B.; Asiri, A. M.; Bawaked, S. M.; Yang, P. *Nano Res.* **2014**, *7*, 132.
7. Liusman, C.; Li, H.; Lu, G.; Wu, J.; Boey, F.; Li, S.; Zhang, H. *J. Phys. Chem. C* **2012**, *116*, 10390.
8. Paciotti, G. F.; Myer, L.; Weinreich, D.; Goia, D.; Pavel, N.; McLaughlin, R. E.; Tamarkin, L. *Drug Deliv.* **2004**, *11*, 169.
9. Rosi, N. L.; Mirkin, C. A. *Chem. Rev.* **2005**, *105*, 1547.
10. Xie, X.; Xu, W.; Liu, X. *Acc. Chem. Res.* **2012**, *45*, 1511.
11. Xu, W.; Xue, X.; Li, T.; Zeng, H.; Liu, X. *Angew. Chem.-Int. Edit.* **2009**, *48*, 6849.
12. Tao, A. R.; Habas, S.; Yang, P. *Small* **2008**, *4*, 310.
13. Dickerson, E. B.; Dreaden, E. C.; Huang, X.; El-Sayed, I. H.; Chu, H.; Pushpanketh, S.; McDonald, J. F.; El-Sayed, M. A. *Cancer Lett.* **2008**, *269*, 57.
14. Haruta, M.; Yamada, N.; Kobayashi, T.; Iijima, S. *J. Catal.* **1989**, *115*, 301.
15. Bond, G. C.; Thompson, D. T. *Catal. Rev.* **1999**, *41*, 319.

16. Panigrahi, S.; Basu, S.; Praharaj, S.; Pande, S.; Jana, S.; Pal, A.; Ghosh, S. K.; Pal, T. *J. Phys. Chem. C* **2007**, *111*, 4596.

17. Zhang, Q.; Wang, H. *ACS Catal.* **2014**, *4*, 4027.

18. Qi, J.; Chen, J.; Li, G.; Li, S.; Gao, Y.; Tang, Z. *Energy Environ. Sci.* **2012**, *5*, 8937.

19. Xu, P.; Yu, R.; Ren, H.; Zong, L.; Chen, J.; Xing, X. *Chem. Sci.* **2014**, *5*, 4221.

20. Zhao, K.; Qi, J.; Zhao, S.; Tang, H.; Yin, H.; Zong, L.; Chang, L.; Gao, Y.; Yu, R.; Tang, Z. *Chin. J. Catal.* **2015**, *36*, 261.

21. Hvolbaek, B.; Janssens, T. V. W.; Clausen, B. S.; Falsig, H.; Christensen, C. H.; Norskov, J. K. *Nano Today* **2007**, *2*, 14.

22. Daniel, M. C.; Astruc, D. *Chem. Rev.* **2004**, *104*, 293.

23. Valden, M.; Lai, X.; Goodman, D. W. *Science* **1998**, *281*, 1647.

24. Haruta, M. *Catal. Today* **1997**, *36*, 153.

25. Xia, B. Y.; Wu, H. B.; Wang, X.; Lou, X. W. *J. Am. Chem. Soc.* **2012**, *134*, 13934.

26. Zeng, J.; Zhang, Q.; Chen, J.; Xia, Y. *Nano Lett.* **2010**, *10*, 30.

27. Sun, Y.; Xia, Y. *J. Am. Chem. Soc.* **2004**, *126*, 3892.

28. Oh, M. H.; Yu, T.; Yu, S.-H.; Lim, B.; Ko, K.-T.; Willinger, M.-G.; Seo, D.-H.; Kim, B. H.; Cho, M. G.; Park, J.-H.; Kang, K.; Sung, Y.-E.; Pinna, N.; Hyeon, T. *Science* **2013**, *340*, 964.

29. Mallin, M. P.; Murphy, C. J. *Nano Lett.* **2002**, *2*, 1235.

30. Raveendran, P.; Fu, J.; Wallen, S. L. *Green Chem.* **2006**, *8*, 34.

31. Link, S.; Wang, Z. L.; El-Sayed, M. A. *J. Phys. Chem. B* **1999**, *103*, 3529.

32. Di Vece, M.; Young, N. P.; Li, Z.; Chen, Y.; Palmer, R. E. *Small* **2006**, *2*, 1270.

33. Sun, Y. G.; Mayers, B.; Xia, Y. N. *Adv. Mater.* **2003**, *15*, 641.

34. Silvert, P.-Y.; Herrera-Urbina, R.; Tekaia-Elhsissen, K. *J. Mater. Chem.* **1997**, *7*, 293.

35. Carotenuto, G.; Pepe, G. P.; Nicolais, L. *Eur. Phys. J. B* **2000**, *16*, 11.

36. Erlebacher, J.; Aziz, M. J.; Karma, A.; Dimitrov, N.; Sieradzki, K. *Nature* **2001**, *410*, 450.

37. Liang, X.; Wang, Z.-J.; Liu, C.-J. *Nanoscale Res. Lett.* **2010**, *5*, 124.

38. Pedireddy, S.; Lee, H. K.; Tjiu, W. W.; Phang, I. Y.; Tan, H. R.; Chua, S. Q.; Troadec, C.; Ling, X. Y. *Nat. Commun.* **2014**, *5*, 4947.

39. Chew, W. S.; Pedireddy, S.; Lee, Y. H.; Tjiu, W. W.; Liu, Y.; Yang, Z.; Ling, X. Y. *Chem. Mater.* **2015**, *27*, 7827.

40. Zeng, J.; Zhao, F.; Qi, J.; Li, Y.; Li, C.-H.; Yao, Y.; Lee, T. R.; Shih, W.-C. *RSC Adv.* **2014**, *4*, 36682.

41. Karunadasa, H. I.; Chang, C. J.; Long, J. R. *Nature* **2010**, *464*, 1329.

42. Karunadasa, H. I.; Montalvo, E.; Sun, Y.; Majda, M.; Long, J. R.; Chang, C. J. *Science* **2012**, *335*, 698.

43. van Schrojenstein Lantman, E. M.; Deckert-Gaudig, T.; Mank, A. J. G.; Deckert, V.; Weckhuysen, B. M. *Nature Nanotechnol.* **2012**, *7*, 583.

44. Han, K. S.; Liu, G.; Zhou, X.; Medina, R. E.; Chen, P. *Nano Lett.* **2012**, *12*, 1253.

45. Lee, J.; Park, J. C.; Song, H. *Adv. Mater.* **2008**, *20*, 1523.

46. Chen, C.; Kang, Y.; Huo, Z.; Zhu, Z.; Huang, W.; Xin, H. L.; Snyder, J. D.; Li, D.; Herron, J. A.; Mavrikakis, M.; Chi, M.; More, K. L.; Li, Y.; Markovic, N. M.; Somorjai, G. A.; Yang, P.; Stamenkovic, V. R. *Science* **2014**, *343*, 1339.

47. Larsson, E. M.; Langhammer, C.; Zoric, I.; Kasemo, B. *Science* **2009**, *326*, 1091.

48. Fu, Q.; Saltsburg, H.; Flytzani-Stephanopoulos, M. *Science* **2003**, *301*, 935.

49. Aditya, T.; Pal, A.; Pal, T. *Chem. Commun.* **2015**, *51*, 9410.

50. Herves, P.; Pérez-Lorenzo, M.; Liz-Marzán, L. M.; Dzubiella, J.; Lu, Y.; Ballauff, M. *Chem. Soc. Rev.* **2012**, *41*, 5577.

51. Chang, Y.-C.; Chen, D.-H. *J. Hazard. Mater.* **2009**, *165*, 664.

52. Lam, E.; Hrapovic, S.; Majid, E.; Chong, J. H.; Luong, J. H. T. *Nanoscale* **2012**, *4*, 997.

53. Qiu, Y.; Ma, Z.; Hu, P. *J. Mater. Chem. A* **2014**, *2*, 13471.

54. Bligaard, T.; Honkala, K.; Logadottir, A.; Norskov, J. K.; Dahl, S.; Jacobsen, C. J. H. *J. Phys. Chem. B* **2003**, *107*, 9325.

55. Yelon, A.; Movaghar, B. *Phys. Rev. Lett.* **1990**, *65*, 618.

56. Wilson, M. C.; Galwey, A. K. *Nature* **1973**, *243*, 402.

57. Loukova, G. V.; Mikhailov, A. I.; Shilov, A. E. *Kinet. Catal.* **2002**, *43*, 746.

58. Clavero, C. *Nature Photonics* **2014**, *8*, 95.

59. Ma, X.; Zhao, K.; Tang, H.; Chen, Y.; Lu, C.; Liu, W.; Gao, Y.; Zhao, H.; Tang, Z. *Small* **2014**, *10*, 4664.

60. Du, J.; Qi, J.; Wang, D.; Tang, Z. *Energy Environ. Sci.* **2012**, *5*, 6914.

61. Liu, X.; He, L.; Zheng, J.; Guo, J.; Bi, F.; Ma, X.; Zhao, K.; Liu, Y.; Song, R.; Tang, Z. *Adv. Mater.* **2015**, *27*, 3273.

62. Link, S.; El-Sayed, M. A. *Int. Rev. Phys. Chem.* **2000**, *19*, 409.

63. Nicewicz, D. A.; MacMillan, D. W. C. *Science* **2008**, *322*, 77.

64. Chen, J.; Saeki, F.; Wiley, B. J.; Cang, H.; Cobb, M. J.; Li, Z. Y.; Au, L.; Zhang, H.; Kimmey, M. B.; Li, X. D.; Xia, Y. N. *Nano Lett.* **2005**, *5*, 473.

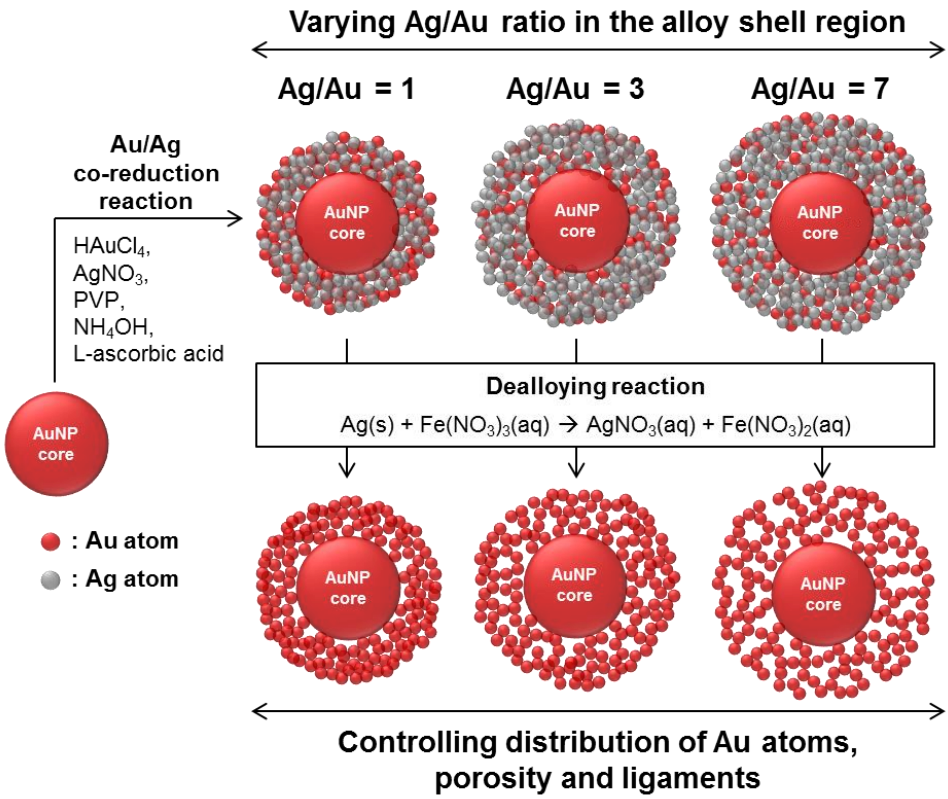

Figure 2.1. Schematic illustration of the dealloying-based synthetic strategy for Au/Au-Ag core/alloy shell nanoparticles (CAS NPs) and Au core/porous shell nanoparticles (CPS NPs).

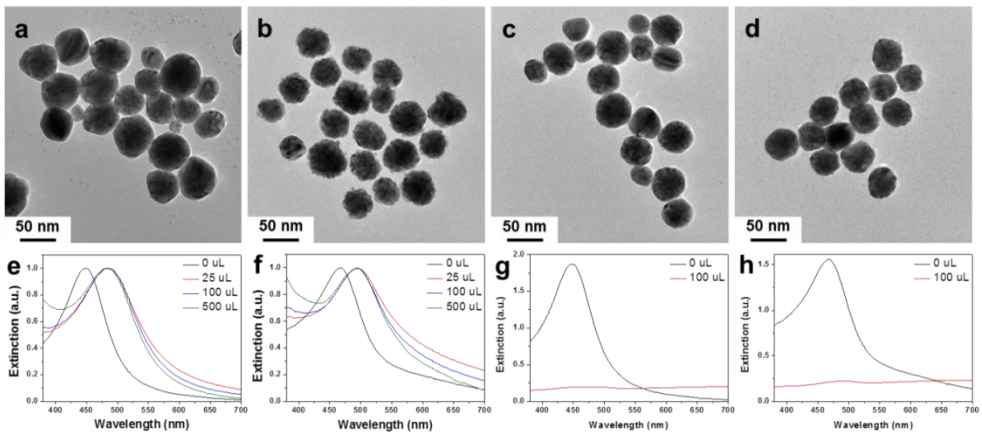

Figure 2.2. The TEM images and UV-Vis spectra of Au-Ag alloy nanoparticles and their dealloyed structures. (a-d) TEM images of Au-Ag alloy and Au dealloyed nanoparticles: (a) $Au_{25}Ag_{75}$ alloy nanoparticles, (b) Dealloyed structures of $Au_{25}Ag_{75}$ alloy nanoparticles, (c) $Au_{50}Ag_{50}$ alloy nanoparticles, (d) Dealloyed structures of $Au_{50}Ag_{50}$ alloy nanoparticles. (e, f) The UV-Vis spectra of Au-Ag alloy nanoparticles and their corresponding dealloyed structures using $Fe(NO_3)_3$ as a Ag etchant: (e) $Au_{25}Ag_{75}$ alloy nanoparticles, (f) $Au_{50}Ag_{50}$ alloy nanoparticles. The single UV-Vis peak (black line) clearly demonstrates that as-synthesized nanoparticles composed of Au-Ag alloy nanoparticles only rather than a mixture of Au and Ag nanoparticles. As the added amount of Ag etchant [$Fe(NO_3)_3$] increased from 25 to 100 to 500 μL, the UV-Vis spectra were not shifted nor changed. (g, h) The UV-Vis spectra of Au-Ag alloy nanoparticles and their dealloyed structures using concentrated HNO_3 solution as a stronger Ag etchant: (g) $Au_{25}Ag_{75}$ alloy nanoparticles. (h) $Au_{50}Ag_{50}$ alloy nanoparticles. The UV-Vis peak disappeared after dealloying reaction, indicating collapse of nanostructures.

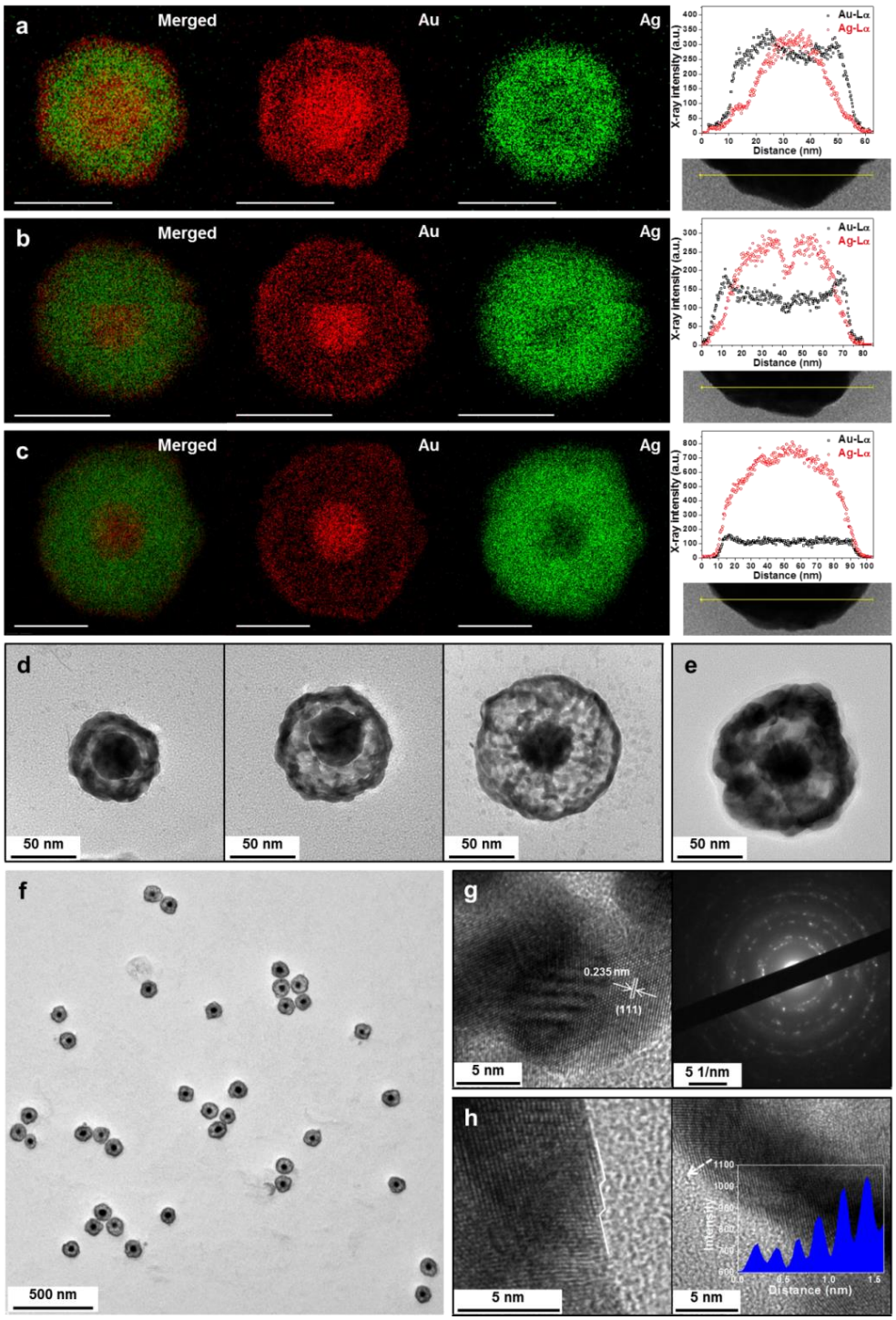

Figure 2.3. Syntheses and characterization of Au/Au-Ag CAS NPs and Au CPS NPs. (a-c) The EDX elemental mapping images (left, black background) of CAS NPs and the EDX line-scan profiles (right) across the shell region (a yellow line in

the STEM image) of CAS NPs with different Ag/Au ratios: (a) CAS(1) NPs, (b) CAS(3) NPs, (c) CAS(7) NPs. The number in parenthesis represents the Ag/Au ratio in the shell region of CAS NPs. The atomic compositions of the shell regions were estimated as $Au_{48.2}Ag_{51.8}$, $Au_{27.9}Ag_{72.1}$, and $Au_{13.3}Ag_{86.7}$ for CAS(1), CAS(3), and CAS(7) NPs, respectively. Scale bar = 50 nm. (d) The TEM images of CPS NPs derived from different CAS NPs: (left) CPS(1) NPs, (middle) CPS(3) NPs, (right) CPS(7) NPs. (e) The core/hollow shell nanoparticle, obtained by the galvanic replacement reaction [CHS(7) NPs]. (f) The TEM image of the synthesized CPS(7) NPs, showing a high-yield synthesis of the targeted nanostructures. (g) The HR-TEM images of the ligaments of CPS(7) NPs. The *d*-spacing of 0.235 nm for adjacent lattice fringes matches well with that of the (111) planes of the face-centered cubic structure (left). The ring shape in the SAED pattern demonstrates that CPS(7) NPs are polycrystalline structures composed of randomly oriented crystallites (right). (h) A stepped surface is shown at the surface of the shell (left). The intensity profile (right), obtained from the dotted arrow region, indicates that the shell surface has stepped surface defect sites.

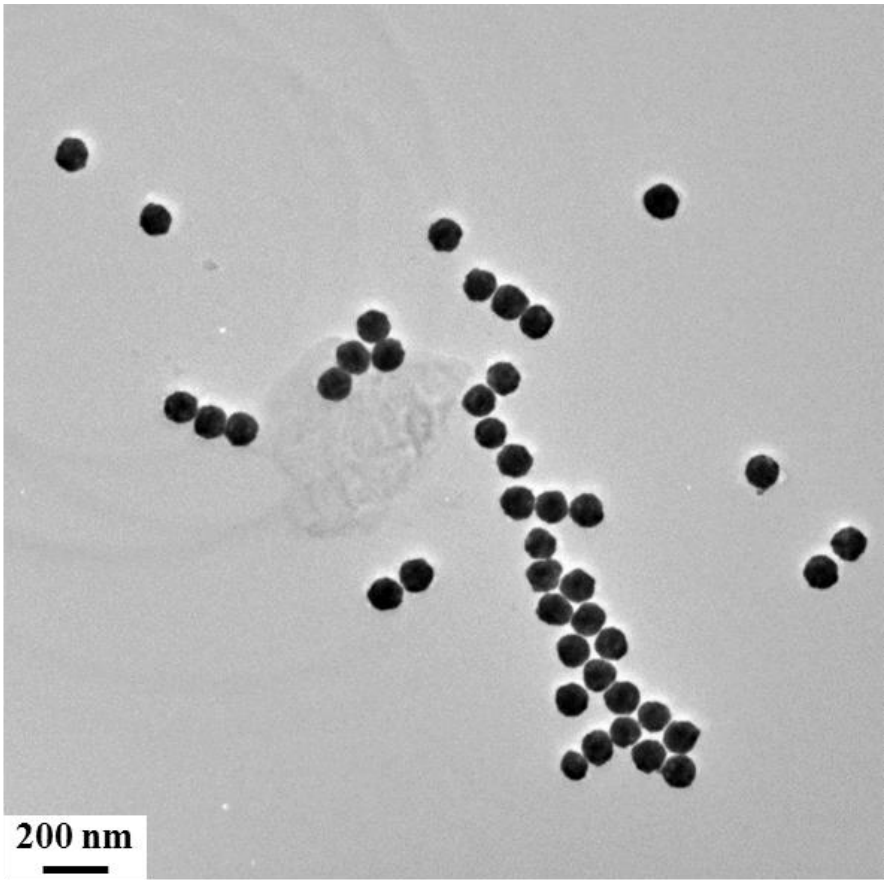

Figure 2.4. The TEM image of CAS(7) NPs, showing a high-yield synthesis of the targeted structures.

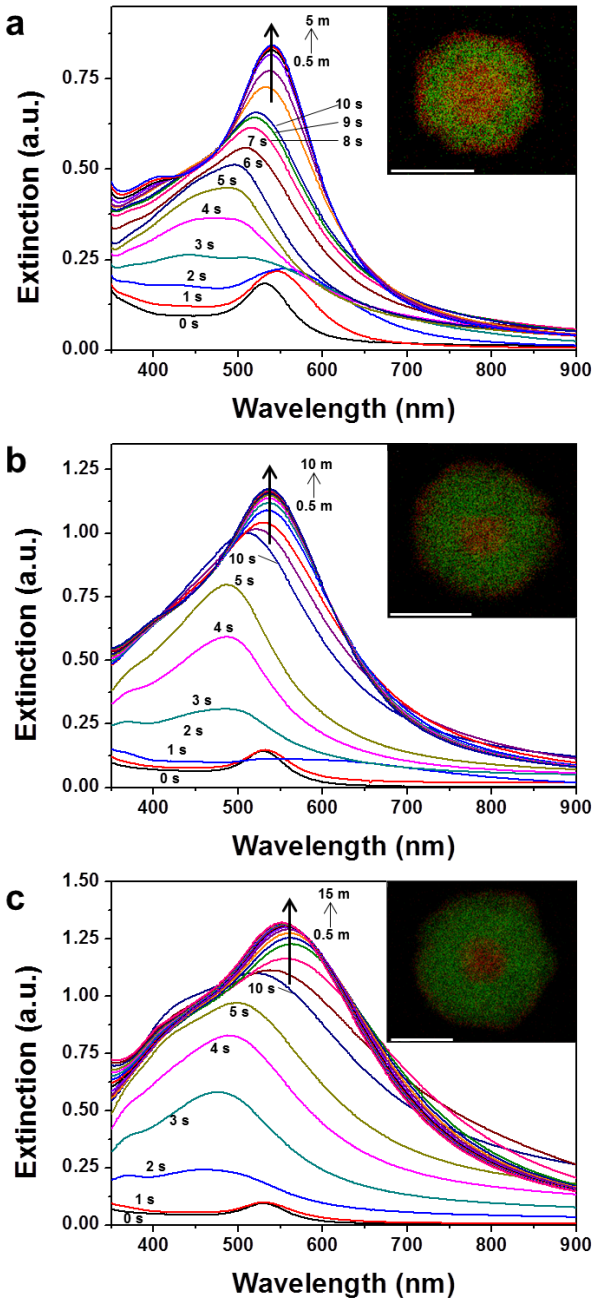

Figure 2.5. The time-dependent UV-Vis spectral changes of the Au/Au-Ag core/alloy shell nanoparticles reaction mixture: (a) CAS(1) NPs, (b) CAS(3) NPs, (c) CAS(7) NPs. Insets represent corresponding EDX elemental mapping of CAS NPs. Scale bar = 50 nm.

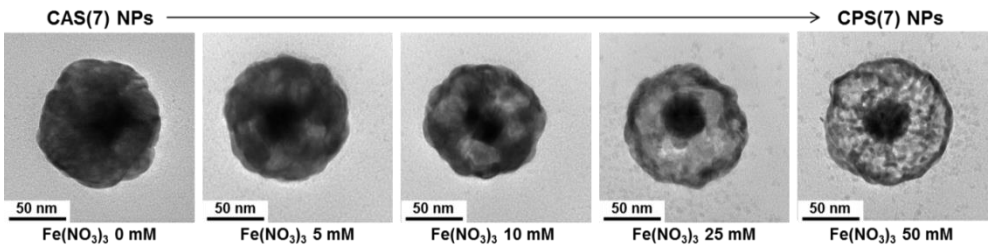

Figure 2.6. The structural changes of CAS(7) NPs to CPS(7) NPs under dealloying reaction while increasing the amount of added $Fe(NO_3)_3$. Iron(III) nitrate acts as an Ag etchant ($Ag(s) + Fe(NO_3)_3(aq) \rightarrow AgNO_3(aq) + Fe(NO_3)_2(aq)$). We propose a synthetic mechanism of CPS NPs as below. At the beginning of dealloying reaction, particles showed pinhole-like vacancies due to the dissolving Ag atoms in the Au-Ag alloy shell. As the reaction progressed, the number of dissolved Ag atoms increased, and Au and Ag atoms diffused outward during vacant areas diffused inward owing to the nanometer-scale Kirkendall effect. Because of difference in the diffusion rates of Au and Ag atoms in the Au-Ag alloy system (Ag atoms diffuse faster than Au atoms), the residual Ag atoms diffused outward and were continuously consumed by an Ag etchant. The Au atoms located in the alloy shell region diffused and were interconnected with each other to form thin ligaments [CPS(7) NPs].

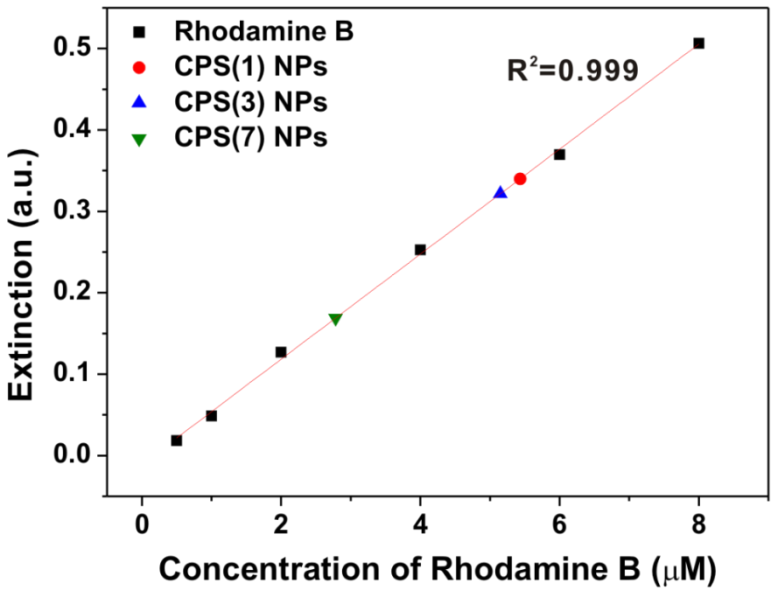

Figure 2.7. The UV-Vis extinction standard curve of rhodamine B solution (black dots) for three CPS NPs. The UV-Vis extinction intensities of rhodamine B unattached after reaction with CPS NPs (red, blue, and green dots) were spotted on the standard curve. To obtain the concentration of unattached rhodamine B, first, the 225 pM CPS NP solution (200 μL) was mixed with 17.4 μM rhodamine B aqueous solution (100 μL), and the resulting solution was shaken for 2 hour at room temperature (the final concentration of CPS NPs and rhodamine B were 150 pM and 5.8 μM, respectively). Then, the UV-Vis extinction intensities of unattached rhodamine B (red, blue, and green dots) were measured from the supernatant of each mixture after centrifugation, and the concentration of unattached rhodamine B was calculated by fitting (the red line). From these results, the concentrations of rhodamine B loaded for each CPS NP were determined by subtracting from the initial concentration of rhodamine B (5.8 μM), and divided by the concentration of CPS NPs (150 pM) to obtain the loading capacity of each CPS NP. The data are summarized in Table 2.1.

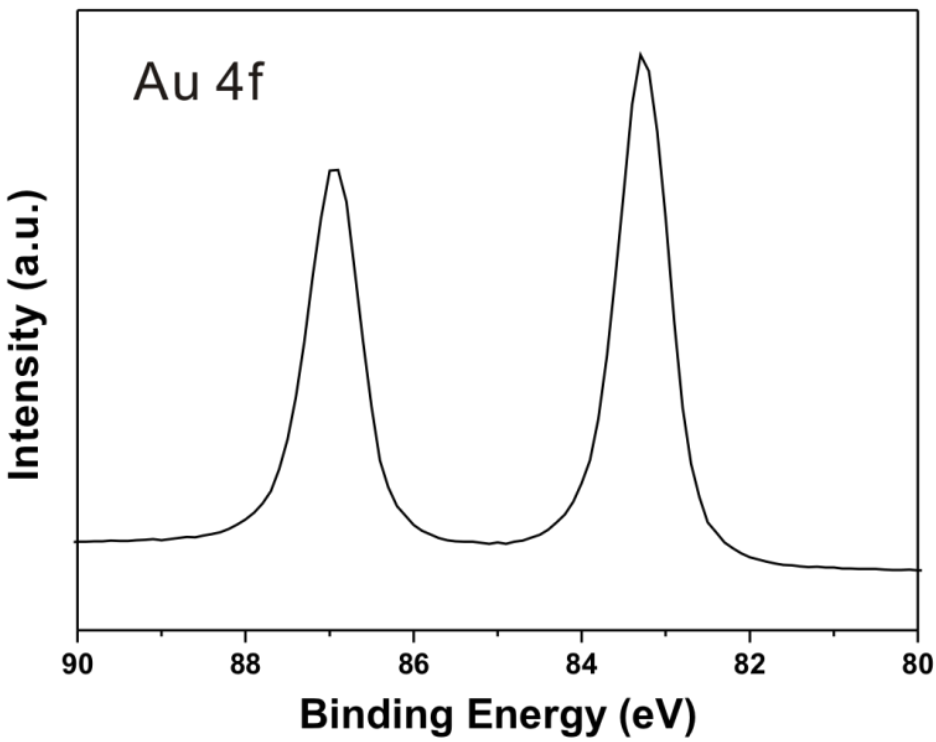

Figure 2.8. The X-ray photoelectron spectroscopy (XPS) spectra of the CPS(7) NPs. The two peaks of Au 4f at 87.0 and 83.3 eV (separated by 3.7 eV) indicate the well reduced metallic Au surface.

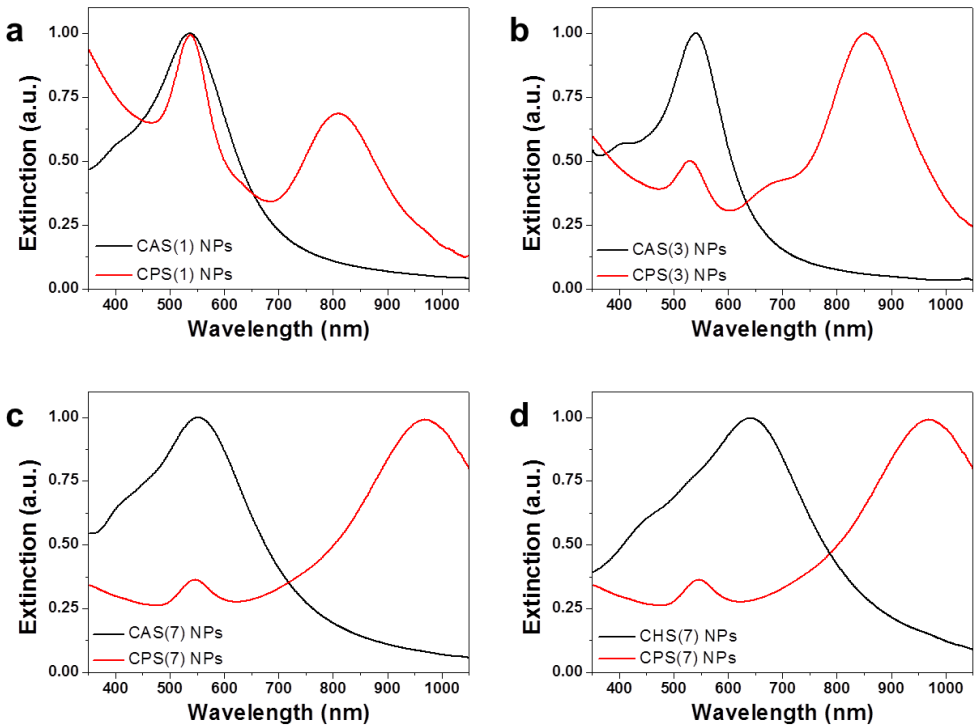

Figure 2.9. The UV-Vis spectra of as-synthesized nanoparticles. (a-c) The UV-Vis spectra of Au/Au-Ag core/alloy shell nanoparticles (CAS NPs, black line) and the corresponding Au-based core/porous shell nanoparticles (CPS NPs, red line): (a) Ag/Au = 1, (b) Ag/Au = 3, (c) Ag/Au = 7. (d) The UV-Vis spectra of porous/hollow shell nanoparticles obtained by the galvanic replacement reaction (CHS(7) NPs, black line) and dealloying reaction (CPS(7) NPs, red line).

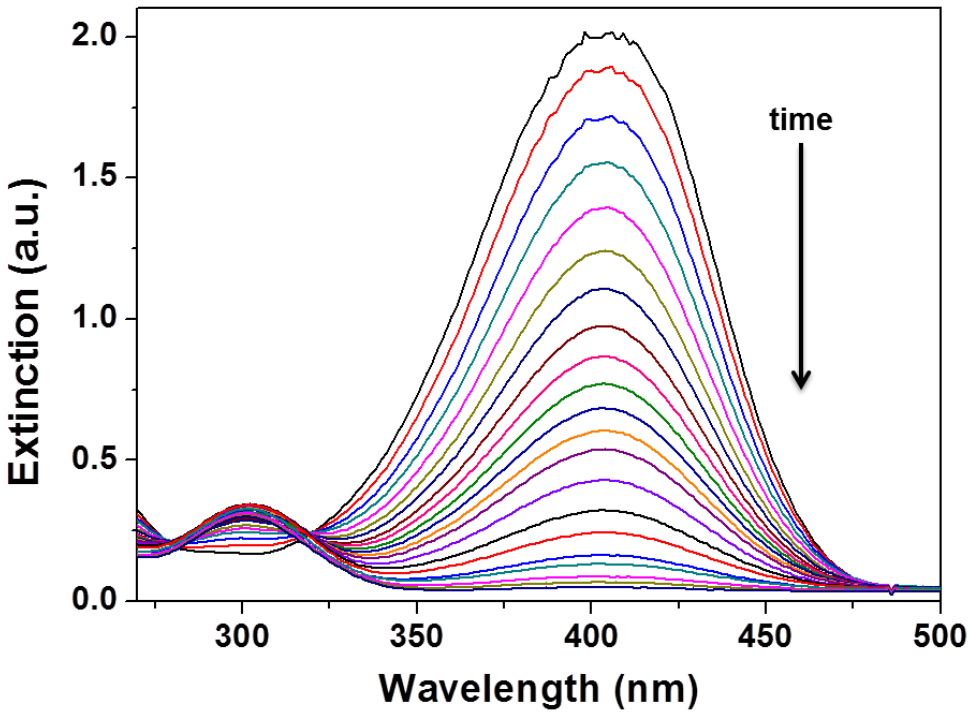

Figure 2.10. The time-dependent UV-Vis spectral changes of 4-NP in the presence of nanocatalysts. The natural extinction peak of 4-NP is strongly exhibited at λ = 317 nm, and shifts to λ = 400 nm after freshly prepared $NaBH_4$ solution is added, indicating the formation of 4-nitrophenolate ions. However, it gradually decreases in the presence of a nanocatalyst with a new extinction peak arising at λ = 300 nm, indicating conversion of 4-NP to 4-AP. During the successive decreases of the extinction peak at λ = 400 nm, two isosbestic points are visible at λ = 280 and 319 nm. These indicate that 4-NP was fully converted to 4-NP without side products in the catalytic reduction.

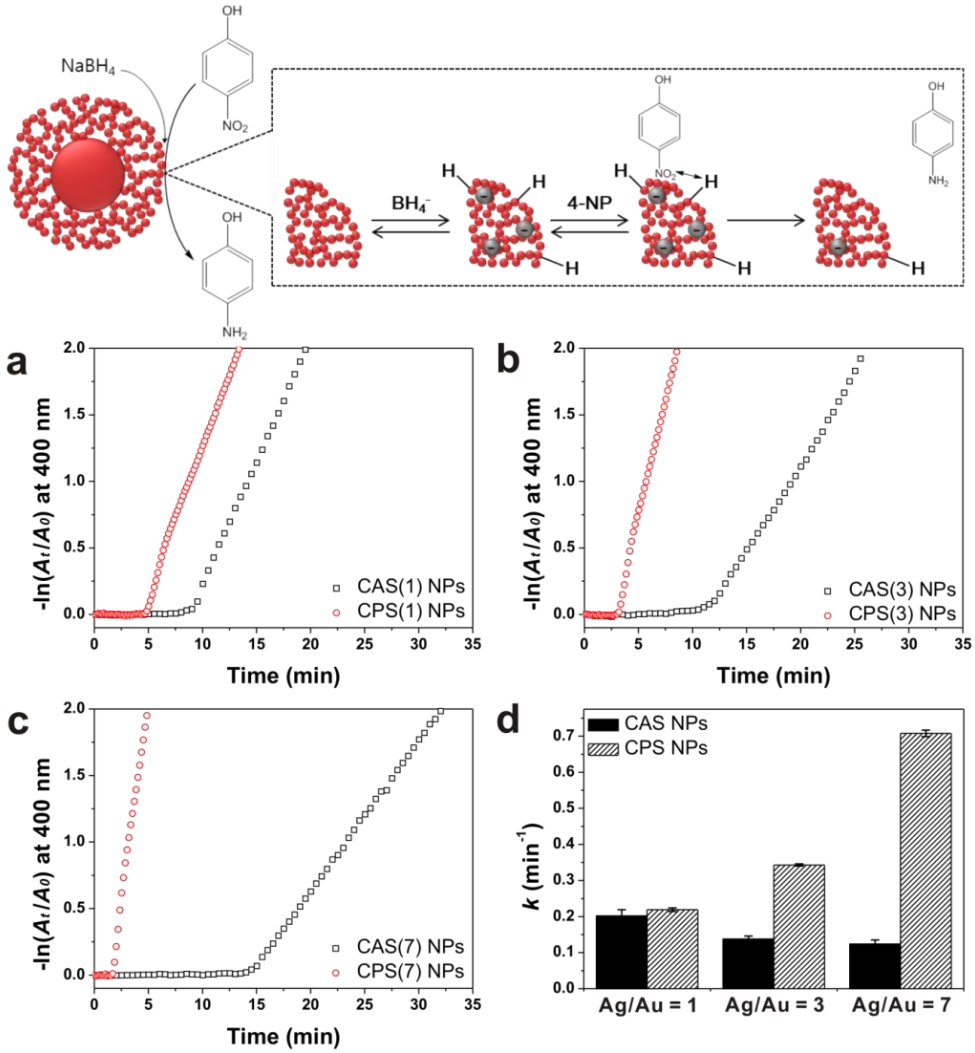

Figure 2.11. The schematic illustration of the Langmuir-Hinshelwood mechanism and the catalytic performances of Au/Au-Ag CAS NPs and Au CPS NPs. 4-NP is reduced by sodium borohydride in the presence of nanocatalysts according to the Langmuir-Hinshelwood mechanism (upper panel). This shows why the surface features and porosity of nanocatalysts are important for this reaction. (a-c) Plots of -ln($\boldsymbol{A_t}$/$\boldsymbol{A_0}$) at λ = 400 nm versus reaction time under pseudo-first-order kinetics for nanocatalysts according to the initial composition of Ag/Au in the shell region: (a) Ag/Au = 1, (b) Ag/Au = 3, (c) Ag/Au = 7. The conversion reaction was carried out at 26 °C. (d) The average ***k*** values of nanocatalysts obtained from plots (a)-(c). All

the CPS NPs showed higher ***k*** values than their alloy forms (CAS NPs), and the change in ***k*** values of CAS and CPS NPs increase as the Ag/Au ratio increases due to formation of higher porosity.

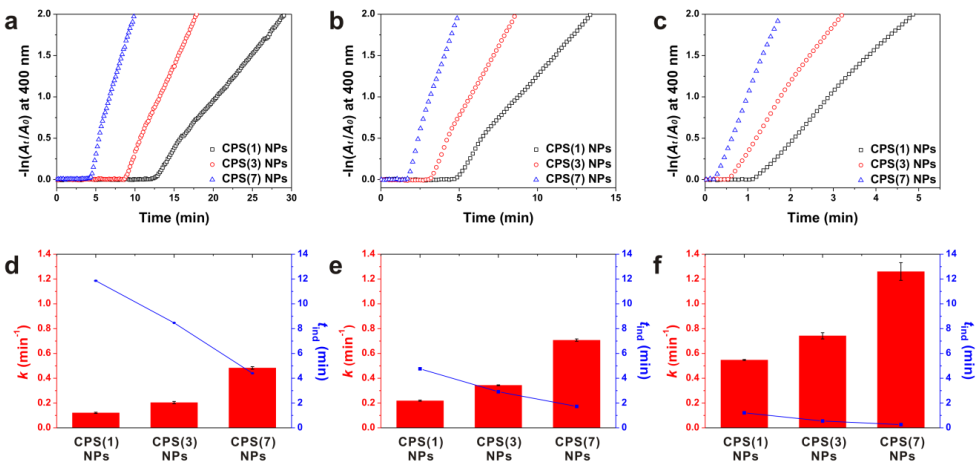

Figure 2.12. Porosity and temperature-dependent catalytic performances of Au CPS NPs. (a-c) Plots of -ln($\boldsymbol{A_t}/\boldsymbol{A_0}$) at λ = 400 nm versus reaction time under pseudo-first-order kinetics for CPS NPs at three different reaction temperatures: (a) 13.5 °C, (b) 26.0 °C, (c) 44.0 °C. (d-f) Average $\boldsymbol{k}$ (red bars) and $\boldsymbol{t_{ind}}$ (blue dots) values obtained from plots (a)-(c). As the porosity of the shell region increases, the reaction occurs earlier (short $\boldsymbol{t_{ind}}$) and faster (high $\boldsymbol{k}$). Increasing reaction temperature results in increased $\boldsymbol{k}$ and decreased $\boldsymbol{t_{ind}}$ values for all cases.

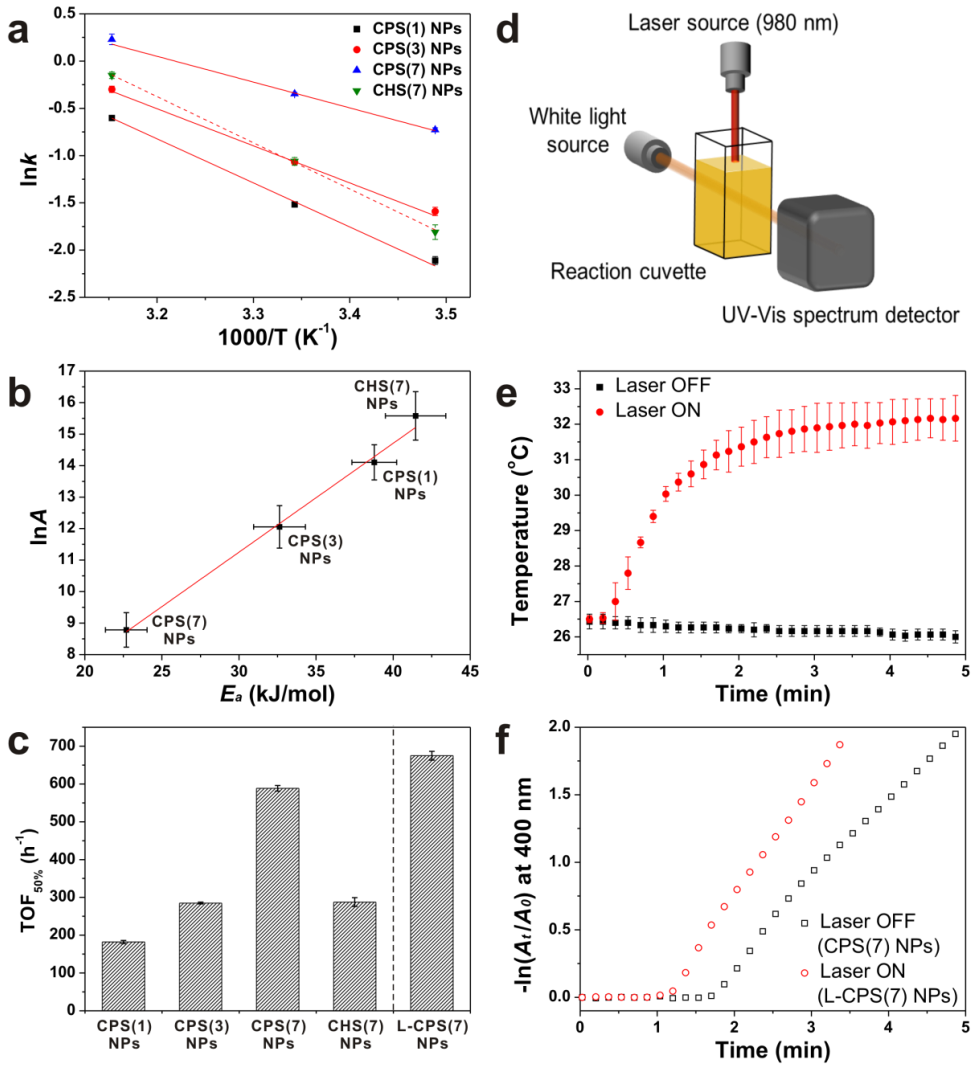

Figure 2.13. Nanocatalyst-dependent enhancements in activation energy, compensation effect, and turnover frequency ($TOF_{50\%}$) and the experimental measurement setup and results of plasmonic nanocatalyst-based photothermal effect. (a) The Arrhenius plots of the reaction catalyzed by CPS(1), CPS(3), CPS(7) and CHS(7) NPs. $\boldsymbol{E_a}$ and $\boldsymbol{A}$ were calculated from the slope and *y*-intercept. The CPS(7) NPs with the highest porosity exhibit the lowest activation energy. In particular, $\boldsymbol{E_a}$ of CPS(7) NPs is significantly lower than that of CHS(7) NPs with the same amount of metal precursors. (b) The plots of ln $\boldsymbol{A}$ versus $\boldsymbol{E_a}$ for nanocatalysts. A linear relationship between ln $\boldsymbol{A}$ and $\boldsymbol{E_a}$ indicates that our system

follows the Meyer–Neldel rule (compensation effect). (c) The $TOF_{50\%}$ values with different nanocatalysts. (d) The experimental setup for the measurement of the photothermal effect of nanocatalysts under laser irradiation. The wavelength and power of laser source are 980 nm and 1.3 W, respectively. (e) Change in solution temperature in the presence or absence of laser irradiation. (f) The plots of -ln($\boldsymbol{A_t}$/$\boldsymbol{A_0}$) at λ = 400 nm versus reaction time under pseudo-first-order kinetics for CPS(7) NPs in the presence or absence of laser irradiation.

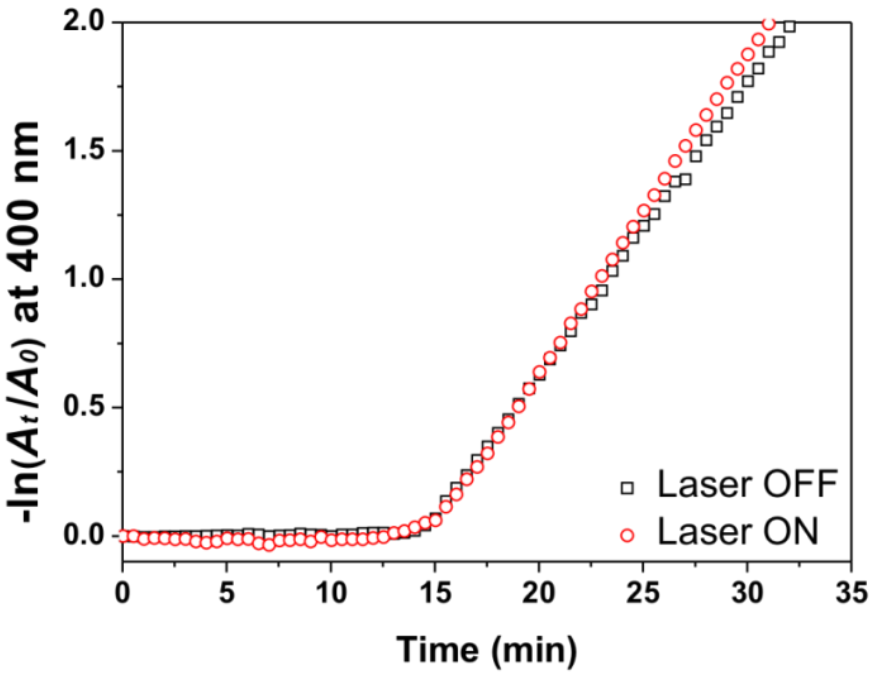

Figure 2.14. The plots of -ln($\boldsymbol{A_t}/\boldsymbol{A_0}$) at λ = 400 nm versus reaction time under the pseudo-first-order kinetics for CAS(7) NPs in the presence or absence of laser irradiation.

Table 2.1. The loaded amounts of rhodamine B per CPS NPs.

	Initial concentration of rhodamine B (μM)	Concentration of unattached rhodamine B (μM)	Concentration of rhodamine B loaded on NPs (μM)	Loading capacity (number/particle)
CPS(1) NPs	5.8	5.435 ± 0.013	0.365 ± 0.013	2434 ± 83
CPS(3) NPs	5.8	5.151 ± 0.015	0.649 ± 0.015	4326 ± 99
CPS(7) NPs	5.8	2.782 ± 0.015	3.018 ± 0.015	20119 ± 102

Table 2.2. The ***k*** and t_{ind} values for the catalytic reaction of CPS NPs and CHS(7) NPs performed at three different temperatures and that of CAS NPs and L-CHS(7) NPs† at 26.0 °C.

	13.5 ºC		26.0 ºC		44.0 ºC	
	k (min^{-1})	t_{ind} (min)	***k*** (min^{-1})	t_{ind} (min)	***k*** (min^{-1})	t_{ind} (min)
CPS(1) NPs	0.121 ± 0.005	11.86 ± 0.02	0.219 ± 0.005	4.77 ± 0.07	0.548 ± 0.004	1.21 ± 0.02
CAS(1) NPs			0.202 ± 0.017	8.21 ± 0.59		
CPS(3) NPs	0.204 ± 0.009	8.46 ± 0.01	0.343 ± 0.003	2.91 ± 0.03	0.742 ± 0.025	0.55 ± 0.03
CAS(3) NPs			0.138 ± 0.008	12.0 ± 0.75		
CPS(7) NPs	**0.483 ± 0.010**	**4.40 ± 0.01**	**0.708 ± 0.009**	**1.73 ± 0.01**	**1.261 ± 0.071**	**0.26 ± 0.03**
L-CPS(7) NPs†			**0.812 ± 0.014**	**1.11 ± 0.01**		
CAS(7) NPs			0.124 ± 0.011	13.8 ± 0.64		
CHS(7) NPs	0.152 ± 0.014	6.62 ± 0.25	0.346 ± 0.014	2.28 ± 0.08	0.861 ± 0.030	0.59 ± 0.03

† The L-CPS(7) NPs (laser-irradiated CPS(7) NPs) were examined their catalytic performance at 26.0 °C under laser irradiation, of which the wavelength and power of laser source are 980 nm and 1.3 W, respectively.

Table 2.3. Summary of the activation energy (***E_a***), pre-exponential factor (***A***), and turnover frequency ($TOF_{50\%}$) values for nanocatalysts.

	E_a (kJ/mol)	***A*** (min^{-1})	$TOF_{50\%}$ (h^{-1})
CPS(1) NPs	38.78 ± 1.46	7.6 – 23.3 (x 10^5)	182.0 ± 4.15
CPS(3) NPs	32.63 ± 1.68	8.8 – 33.8 (x 10^4)	285.0 ± 2.49
CPS(7) NPs	**22.69 ± 1.35**	**3.8 – 11.3 (x 10^3)**	**588.3 ± 7.48**
L-CPS(7) NPs	**-**	**-**	**674.8 ± 11.63**
CHS(7) NPs	41.45 ± 1.96	2.7 – 12.5 (x 10^6)	287.5 ± 11.63

Chapter 3

Synthesis and SERS Applications of Interlayer- and Polarisation-Free Plasmonic Nanoparticles with an Interior Nanogap

3.1. Introduction

Plasmonic nanostructures, particularly with plasmonically coupled nanogap, are of paramount importance and interest due to their strong, tunable optical properties and enormous potentials in various applications including catalysis, sensing, imaging, solar energy conversion.[1-5] Because optical properties are highly affected by structural features of plasmonic nanostructures (e.g., structure uniformity, nanogap size, and geometric configuration), thus the precise design and high-yielding synthesis of plasmonic structures are required to produce a robust, quantitative, and reproducible optical signal that can be used in practical applications. Along with the tremendous development of plasmonic nanostructures synthesis, surface–enhanced Raman scattering (SERS) has received a lot of attention because of its ultrahigh sensitivity, which can be extended to the single-molecule level.[6,7] In this regard, SERS-based techniques are being exploited widely in plasmonics and analytical applications, including for biosensing and the detection of chemical warfare agents and food contaminants.[8-11] In plasmonics, it is now well known that the excitation of localised surface plasmon resonances in nanoparticles (NPs) of noble metals (in particular, those of Au and Ag) can significantly enhance and localise the electromagnetic (EM) field at specific locations, which are called “hot spots”. This phenomenon plays a major role in signal enhancement in most SERS applications.[12-15] There have been numerous attempts to produce SERS-active structures by using morphology-controlled noble metal nanostructures, such as nanotips, nanopores, and nanoscale-roughened surfaces.[16-18] In particular, with respect to SERS, the EM field can also be enhanced significantly via plasmonic coupling at the gaps or junctions between metallic nanostructures.[19] However, plasmonic coupling at these gaps is affected by the interparticle distance, which, in turn, has a marked effect on the SERS signal.[20,21] This can induce irreproducibility and variability in the SERS signal. Consequently,

high-precision gap engineering in the case of reproducible and reliable SERS substrates, while a challenge, is essential.[1,22-24]

Among the plasmonic nanogap structures such as inter-nanogap, nanocrevice, and interior-nanogap,[1] the interior-nanogap structure is most promising structure in SERS because of its structural features; its uniformly confined nanogap between core and shell can contain the higher number density of the hot spots, resulting in strongly enhanced SERS signal. In addition, a stable SERS signal can be obtained regardless of the external environment, owing to the encapsulation of the Raman molecule within the interior nanogap. To facilitate the formation of SERS-active interior-nanogap structures, various synthetic strategies have been reported.[25-29] Halas's group synthesised interior nanogap by forming silica (SiO_2) layer between Au nanosphere and Au nanoshell, referred as plasmonic nanomatryushka.[25] The extinction spectra of Au/SiO_2/Au nanoparticles could be controlled by changing the interlayer and the shell thickness; however, interior-nanogap size formed by silica layer were relatively large (>10 nm) which deviates significantly from the regime of interest that affects signal enhancement in SERS. Other approaches, based on Raman-molecule-labelled polymers or small molecules, have also applied to synthesise interior nanogap.[26-29] These synthetic strategies could form nanometre-sized interior nanogap (1–2 nm), however, they resulted in the uncontrollable synthesis of non-uniform interior-nanogap structures. Recently, our group developed DNA-tailorable NPs with a uniformly confined 1-nm interior gap (named as Au nanobridged nanogap particles, Au-NNPs)[30,31] and elucidated the role of the surface roughness of the NPs in the enhancement of the EM field in the interior-nanogap region.[32] This DNA-based synthesis strategy is highly suited for forming structures with an interior nanogap in high yields. The Au-NNPs generate a strong, stable, and quantitatively reproducible SERS signal with a high EF and narrow EF distribution owing to the uniformly confined interior nanogap, thus preventing uncertainty of SERS signal. Therefore, such interior-nanogap-

containing nanostructures are ideal for use in practical SERS applications. Nevertheless, this synthesis approach has a few drawbacks when it comes to large-scale production and practical applicability, given that it is expensive and time consuming. Furthermore, the loading capacity of Raman-dye-modified DNA is limited because of the intrinsic repulsion force between the negatively charged phosphate/sugar backbones.[33] For this reason, the intensity of the SERS signal is less than the maximum possible, as the number of Raman dyes that can be loaded is low even when the EF value is high.

Notably, the plasmonic structures mentioned above need interlayer such as silica, polymers, or DNA to form interior nanogap. These interlayer-induced interior-nanogap formations usually require complex synthetic procedure, or are expensive and time-consuming in preparation, which are barely suitable for practical applications. More importantly, precise and reproducible nanometre-scaled control of interlayer to synthesise uniform interior-nanogap structure is extremely challenging. Because the optical properties caused by interior nanogap are sensitively altered and affected by the nanometre-scaled small variations in size, uncontrollable synthetic methods cannot ensure the uniformity and reproducibility in the optical signals, indicating incongruity to applications requiring reliable and quantitatively reproducible results. Therefore, the advanced synthetic strategy for high-yielding preparation of uniform and nanogap-controllable plasmonic nanoparticles in the absence of interlayers is urgent. The interlayer-free plasmonic nanoparticles with an interior nanogap can be synthesised by galvanic replacement reaction.[34] However, the precise and uniform formation of very thin sacrificial layer (< 3 nm) which is essential to form interior-nanogap structure is challenge. Thus, this strategy suffers from a non-uniform synthesis yield of the targeted interior-nanogap structure. In addition, an additional shell growth step is needed to form the thick shell structure. Furthermore, the temperature for the galvanic

replacement reaction must be high (~100 °C) to ensure a well-defined morphology.[35]

Here, for the first time, we present a synthetic strategy for forming Au/Ag dealloyed gap (DAG) NPs with an interlayer-free intra-nanogap from core-alloy shell (CAS) NPs in a high yield via asymmetric dealloying process at room temperature (Figure 3.1). As the highly controllable dealloying reaction progresses with the DAG NPs, nanometre-sized interior gap was formed on Au core surface via selective Ag-etching and inter-diffusion of Ag atoms, resulting in the formation of NPs with ~2-nm interior gap in a high yield (~95%). It should be noted that this dealloying process can spontaneously undergo at room temperature due to the nature of corrosion process occurred in the presence of etchants or oxidants such as oxygen, sulfur, and water, even at the low temperature. Remarkably, the interior nanogap was uniformly formed in a symmetric fashion, leading the polarisation-independent SERS signals from the Raman dyes in the interior gaps of these structures, and the SERS signal intensity linearly increases as particle concentration increases, allowing for highly reliable, quantitative SERS. Importantly, Au-gap-Au/Ag DAG NPs were modified with DNA or cell-targeting peptides for DNA sensing and targeted cell-imaging applications, and the assay results show that these DNA-modified DAG NPs generate highly quantitative and sensitive DNA detection results, ranging from aM to fM target concentrations. Finally, these DAG NPs were functionalized with cell-targeting peptides for cell imaging applications. The results suggest that the peptide-modified DAG NPs can selectively target integrin $\alpha_v\beta_3$ expression cells and allow for imaging intracellular regions with Raman signals.

3.2. Experimental Section

Reagents and materials

Gold nanoparticles (AuNPs, average diameter of 40 nm) and magnetic microparticles (MMPs, Dynabeads® MyOne™ Carboxylic Acid, average diameter of 1 μm) were purchased from Ted Pella, Inc. (Redding, CA, USA) and Invitrogen Dynal AS (Oslo, Norway), respectively. HPLC-purified oligonucleotides were purchased from Bioneer (Daejeon, South Korea) and carboxymethyl-PEG-thiol (CM-PEG-SH, M_w≈5,000) was purchased from Laysan Bio, Inc. (Arab, AL, USA). Cyclo(Arg-Gly-Asp-D-Phe-Lys) (c(RGDyK), cRGD) peptide was purchased from Peptides International, Inc. (Louisville, KY, USA). Gold(III) chloride trihydrate ($HAuCl_4 \cdot 3H_2O$, ≥99.9%), silver nitrate ($AgNO_3$, 99.9999%), 4-mercaptopyridine (4-MPy, 95%), polyvinylpyrrolidone (PVP, M_w≈40,000), ammonium hydroxide solution (NH_4OH, 28.0-30.0% NH_3 basis), L-ascorbic acid (AA, ≥99.0%), iron(III) nitrate nonahydrate ($Fe(NO_3)_3 \cdot 9H_2O$, ≥98.0%), 2-(*N*-morpholino)ethanesulfonic acid (MES, ≥99.0%), *N*-(3-dimethylaminopropyl)-*N'*-ethylcarbodiimide hydrochloride (EDC, commercial grade), *N*-hydroxysulfosuccinimide sodium salt (Sulfo-NHS, ≥98%), ethylenediaminetetraacetic acid (EDTA, 99.4-100.06%), DL-dithiothreitol (DTT, ≥99.0%), Tween®-20, and sodium dodecyl sulfate (SDS, ≥98.5%) were purchased from Sigma-Aldrich (St. Louis, MO, USA). Tris[hydroxymethyl]aminomethane (Tris, 99.8-100.1%) was purchased from USB Corporation (Cleveland, OH, USA). Ethyl alcohol (anhydrous, 99.9%) and sodium chloride (NaCl, ≥99.0%) were purchased from DAEJUNG Chemicals & Metals Co. (Siheung, Gyeonggi, Korea). All the chemical reagents were used as received without further purification. NANOpure water (Millipore, Milli-Q 18.2 MΩ·cm) was used throughout the experiments.

Preparation of 4-MPy-modified Au nanoparticles

To attach the Raman reporter molecules (4-mercaptopyridine, 4-MPy) onto the AuNPs, 10 μL of an ethanol solution of 4-MPy (1 mM) was injected into 1 mL of a solution (100 pM) of the Au NPs (average diameter of 40 nm). The resulting mixture was then shaken over 2 h. Next, the 4-MPy-modified AuNPs (MPy-AuNPs) were washed with distilled water by centrifugation at 6,000 rpm for 10 min and redispersed in distilled water for further use.

Synthesis of Au/Au-Ag core/alloy shell nanoparticles

The Au/Au-Ag core/alloy shell NPs (CAS NPs) were synthesised using a previously reported procedure with minor modifications.[40] Typically, 200 μL of the MPy-AuNPs solution (100 pM) and 200 μL of a polyvinylpyrrolidone (PVP, $M_w \approx$ 40,000) solution (1 wt%) were mixed gently. Then, 50 μL of a $AgNO_3$ solution (1 mM), 16 μL of a NH_4OH solution, and 150 μL of a $HAuCl_4$ solution (1 mM) were sequentially added to the mixture. Next, 200 μL of an L-ascorbic acid (AA) solution (20 mM) was immediately injected into the mixture under gentle shaking. The resulting mixture was shaken gently for 1 h at room temperature. Finally, the solution was washed twice with distilled water by centrifugation at 6,000 rpm for 10 min and redispersed in distilled water.

Synthesis of gap-less Au/Au core/shell nanoparticles

To synthesise the gap-less Au/Au core/shell NPs (gap-less AuNPs), we simply modified the procedure for synthesising the CAS NPs. Typically, 200 μL of the $HAuCl_4$ solution (1 mM) was added instead of 50 μL of the $AgNO_3$ (1 mM) solution and 150 μL of the $HAuCl_4$ solution (1 mM) during the synthesis process. The rest of the procedure was the same as that for the synthesis of the CAS NPs.

Synthesis of dealloyed gap nanoparticles

The dealloyed gap NPs (DAG NPs) were synthesised by introducing $Fe(NO_3)_3$ as a Ag etchant into the fabricated CAS NPs. Typically, 100 μL of a solution of the CAS NPs (100 pM) was mixed with 100 μL of a PVP solution (1 wt%). Next, 125 μL of an $Fe(NO_3)_3$ solution (20 mM) was injected into this mixture under gentle shaking. The resulting mixture was shaken mildly for 30 min at room temperature, washed twice with distilled water by centrifugation at 6,000 rpm for 10 min, and redispersed in distilled water.

Setup for micro-Raman spectroscopy

For the solution-state Raman analysis, a solution of the as-synthesised NPs (100 pM) was loaded into a capillary tube (soda lime glass; CAT. NO: 2502) obtained from Kimble Chase (Vineland, NJ, USA). All the Raman measurements were performed using a Renishaw inVia microscope equipped with 514 (5 mW), 633 (4 mW), and 785 nm (4 mW) excitation lasers, a 20× objective lens (NA = 0.40, Leica), and a standard charge-coupled device (CCD) array detector (576 × 384 pixels; Peltier; cooled to -70 °C). The SERS spectra were acquired using an acquisition period of 10 s and were recorded for wavenumbers of 800–1,800 cm^{-1}.

Setup for AFM-correlated nano-Raman spectroscopy

To obtain the SERS spectra from the individual NPs, we employed an AFM-correlated nano-Raman microscope (Ntegra, NT-MDT) equipped with an inverted optical microscope (IX 73, Olympus). We performed the AFM-based multistep tip-matching procedure based on previous studies, in order to accurately match the end of the AFM tip and the laser focal spot.[30,57] First, the laser beam was focused on the upper surface of a particle-loaded cover glass slip (poly-L-lysine-coated cover glass), and end of the AFM tip was positioned on the laser focal spot, which was

observed with micrometre-level accuracy using a video camera. Next, Rayleigh scattering images were recorded during the scanning of the tip along the x- and y-axes, and the AFM tip was subsequently moved to the region with the highest scattering intensity, such that the tip was located on the laser focal spot. Finally, the end of the AFM tip was moved with nanometre-level precision by observing the intensity of the Raman signal of the silicon (520 cm^{-1}) in the AFM tip. The highest Raman signal intensity was obtained when the end of the AFM tip was located exactly at the centre of the laser focal spot. In this tip-matching state, Rayleigh scattering images and AFM topographical images were obtained simultaneously using a piezoelectric x, y sample scanner. The SERS spectra of the individual NPs were obtained using a CCD detector (1024 × 256 pixels; Peltier; cooled to -70 °C, Andor) and a 633-nm excitation laser (He-Ne laser, Thorlabs). The exposure time was 20 s, and the laser power was 60 μW. An oil-immersed microscope objective (100×, NA = 1.4, Olympus) was used to focus the laser beam on a diffraction-limited spot (~ 250 nm when a 633-nm laser was used).

Characterisation

The morphological characteristics of the as-synthesised NPs and the target-DNA-induced sandwich hybridisation complexes were evaluated using a TEM system (JEM-2100, JEOL), a high-resolution TEM (HR-TEM) system (JEM-2100F, JEOL), and a field-emission SEM (FE-SEM) system (JSM-7800F Prime, JEOL). The elemental maps and line scan profiles of the NPs were obtained using a EDX system (INCA, Oxford Instruments) coupled with an HR-TEM system. The UV-Vis spectra were acquired using an UV-Vis spectrophotometer (HP 8453, Agilent Technologies).

Calculations of SERS enhancement factor

The SERS enhancement factor (EF) was calculated using the following equation (Equation 1):

$$\text{Enhancement factor (EF)} = \frac{I_{SERS}}{N_{SERS}} \Big/ \frac{I_{BULK}}{N_{BULK}} \quad (1)$$

where I_{SERS} and I_{BULK} are the intensities of the Raman peak at 1,003 cm^{-1} for the individual DAG NP and the pure 4-MPy solution (200 mM, 22.23 mg/mL), respectively; and N_{SERS} and N_{BULK} are the number of 4-MPy molecules on a single DAG NP and within solution, respectively. The number of 4-MPy molecules on a single DAG NP (N_{SERS}) was estimated by assuming that the maximum number of 4-MPy molecules were packed on the AuNPs (average diameter of 40 nm); the average monomolecular area of 4-MPy has been estimated to be 0.18 nm^2.[58,59] To estimate I_{BULK} and N_{BULK}, 12 μL of a 4-MPy solution (200 mM, 22.23 mg/mL) was introduced into a sticker chamber placed on a glass substrate and illuminated with a 633-nm laser for 30 s through an objective lens (20×, NA = 0.4). Assuming that the effective excitation volume (V_{BULK}) was a cylinder, the height (h) was calculated using the following equation (Equation 2):

$$\frac{h}{2r} = \frac{3.28\eta}{NA} \quad (2)$$

where η is the refractive index of the medium (water; 1.33) and r is the radius of the laser beam (5 μm). Further, N_{BULK} was calculated using the following equation (Equation 3):

$$N_{BULK} = (V_{BULK} \text{ x } D/M) \text{ x } N_A \quad (3)$$

where D is the density of 4-MPy (22.23 mg/mL), M is the molar mass of 4-MPy (111.16 g/mol), and N_A is Avogadro's constant (6.02×10^{23} mol^{-1}). Lastly, we measured and plotted the incident-laser-power-dependent Raman intensities of the 4-MPy solution to determine the value of I_{BULK} for calculating the SERS EF (Figure 3.17).

Preparation of DNA-modified magnetic microparticles

We prepared DNA-modified magnetic microparticles (DNA-MMPs) using a previously reported procedure with minor modifications.[60] Typically, 200 μL of a solution of the MMPs coated with the carboxyl functional group (10 mg/mL) was transferred to a tube and placed in a magnetic separator to remove the supernatant. After the supernatant had been discarded, the MMPs were washed twice with 200 μL of 100 mM MES buffer (pH 4.8) and redispersed in 20 μL of the MES buffer. Next, 10 μL of 5'-amine-modified oligonucleotides (1 mM, DNA sequence: 5'-NH_2-A_{10}-PEG_6-AGAAAGAGGAGTTAA-3') and 10 μL of a 1 M EDC solution in the MES buffer (100 mM, pH 4.8) were added to the washed MMPs, and the resulting mixture was shaken for 4 h at room temperature. Finally, the mixture was washed three times with 200 μL of a washing buffer (250 mM, Tris pH 8.0, 0.01% Tween®-20), and the DNA-modified MMPs were suspended in 200 μL of a storage buffer (10 mM, Tris pH 8.0, 1 mM EDTA).

Preparation of DNA-modified dealloyed gap Raman probes

To prepare the DNA-modified dealloyed gap Raman probes (DAG probes), thiolated oligonucleotides were attached onto the DAG NPs through Au-S bonding. First, disulfide-modified oligonucleotides were reduced in a 100 mM DTT solution for 2 h at room temperature and purified using an NAP-5 column (Sephadex™ G-25 DNA Grade, GE Healthcare, UK) to obtain thiolated oligonucleotides. Then, the

freshly DTT-reduced thiolated oligonucleotides (DNA sequence: 5'-TCCATGCAACTCTAA-A_{10}-SH-3') were added to a solution of the DAG NPs and allowed to incubation overnight at room temperature under mild shaking. The solution was then adjusted to obtain a final phosphate concentration of 10 mM (pH 7.4) and a SDS concentration of 0.1% (wt/vol). After incubation for 1 h, the mixture was brought to 0.3 M NaCl by the gradual addition of six aliquots of a 2 M NaCl solution at intervals of 1 h. The mixture was then kept overnight at room temperature under mild shaking. Next, the mixture was washed three times with an assay buffer (10 mM phosphate buffer, 0.3 M NaCl, 0.01% SDS, pH 7.4) by centrifugation at 6,000 rpm for 5 min and redispersed in the assay buffer for use as a DNA detection assay.

SERS-based DNA detection assay

The SERS-based DNA detection assays were performed using a typical sandwich-hybridisation assay. First, a solution of the target DNA (hepatitis A virus; HAV, DNA sequence: 5'-TTAGAGTTGCATGGATTAACTCCTCTTTCT-3') was serially diluted from 10 aM to 1 pM using an assay buffer (10 mM phosphate buffer, 0.3 M NaCl, 0.01% SDS, pH 7.4); non-complementary DNA (hepatitis B virus; HBV, DNA sequence: 5'-TTGGCTTTCAGTTATATGGATGATGTGGTA-3') was also used, in order to confirm the DNA targeting specificity of the probes. Next, 100 μL of the diluted target DNA solution was mixed with 1 μL of the DNA-MMP (10 mg/mL) solution, and the mixture was allowed to incubation for 1 h at room temperature under shaking. Then, 20 μL of the DAG probe solution (100 pM) was added to the target-DNA-capturing MMP solution, and the mixture was allowed to incubation for 30 min at room temperature under shaking. The target-captured DAG probe-MMP complexes were washed three times with an assay buffer and the final solution volume was adjusted to 10 μL. For the Raman

measurements, 5 μL of this concentrated solution was transferred onto a cover glass placed on a magnet. Owing to the applied magnetic force, the complexes were collected on the surface of the cover glass. The remaining solvent was wiped with tissue paper, and the collected complexes were dried under ambient conditions for use in the Raman measurements. For reducing the variance in the unevenness of the focal spot of the prepared sample, the dried cover glass was inverted (turned upside down), and the focus was adjusted on the backside of the sample. All the Raman measurements were performed using a Renishaw inVia microscopy system with a 785-nm excitation laser (2 mW). The SERS spectra were acquired using an acquisition time of 5 s. For clear identification, the SERS intensities were obtained by consecutive accumulation of five measurements.

Preparation of cRGD peptide-modified dealloyed gap imaging probes

To perform SERS-based target-specific cell imaging, the surfaces of the DAG NPs were functionalised with cRGD peptide, which has a high affinity for $\alpha_v\beta_3$ integrin. To prepare the PEGlyated DAG NPs, first, 50 μL of a 0.5 mM solution of CM-PEG-SH ($M_w \approx$ 5,000) was added to 500 μL of a dispersion of the DAG NPs (50 pM) in 0.01% SDS, and the mixture was allowed to rest overnight at room temperature under mild shaking. The mixture was then washed twice with a 50 mM MES buffer solution (pH 4.8) by centrifugation at 6,000 rpm for 5 min. Next, the carboxylic acid part of the PEG attached onto the DAG NPs was linked with the cRGD peptide through an EDC/Sulfo-NHS coupling reaction. Typically, 25 μL of freshly prepared 20 mM EDC and Sulfo-NHS solutions were sequentially added to 500 μL of the as-prepared PEGlyated DAG NPs (25 pM) and the reaction mixture was stirred for 20 min. The resulting mixture was then washed twice with a 10 mM phosphate buffer (pH 7.4) by centrifugation at 6,000 rpm for 5 min, and the

supernatant was discarded. To this concentrated solution, 125 μL of the cRGD peptide (1 mM) dissolved in a 10 mM phosphate buffer (pH 7.4) was added, and the reaction mixture was shaken for 6 h. It was then washed twice with a 10 mM phosphate buffer (pH 7.4) by centrifugation at 6,000 rpm for 5 min and suspended in phosphate buffered saline (10 mM phosphate buffer, 0.15 M NaCl, pH 7.4) for further use.

SERS-based target-specific cell imaging

The human malignant U87MG glioma cell line and human breast carcinoma MCF-7 cell line were obtained from American Type Culture Collection (ATCC) and were cultured in Minimum Essential Medium (MEM) and Dulbecco's Modified Eagle Medium (DMEM) along with 10% foetal bovine serum, 100 U/mL penicillin, and 100 μg/mL streptomycin at 37 °C under 5% CO_2. Both types of cells were cleaved by trypsin, loaded (5×10^3 cells/mL) onto poly-d-lysine-coated 50-mm glass-bottom dishes (MatTek Corporation, Ashland, MA, USA), and incubated overnight. Then, the cell-loaded dishes were rinsed with PBS buffer (10 mM phosphate buffer, 0.15 M NaCl, pH 7.4), filled with the cRGD-functionalised DAG NPs suspended in a medium (12.5 pM), and kept for 6 h at 37 °C under 5% CO_2. After incubation, the cell monolayer was washed with PBS buffer and fixed with 4% paraformaldehyde. To perform SERS-based target-specific cell imaging, the cells incubated with the cRGD-functionalised DAG NPs were scanned, and the SERS spectrum at each mapping pixel (2 μm × 2 μm) was recorded. All the Raman measurements were performed using a Renishaw inVia microscopy system with a 785-nm (4 mW) or 633-nm (400 μW) excitation laser, and the SERS signals were recorded for an acquisition time of 1 s for each mapping pixel. Finally, the integrated SERS intensities (from 983 cm^{-1} to 1,023 cm^{-1}) for each mapping pixel were colour-scaled for cell imaging.

Theoretical calculations

The extinction spectra of the NPs were calculated Mie theory.[42] An analytic model[61] was used for the dielectric functions of Au and Au-Ag alloy. The particles were considered as embedded in water ($\varepsilon = 1.33^2$). The average particle sizes, interior-nanogap sizes, shell thicknesses, and atomic compositions of the as-synthesised NPs are given in Figure 3.3 and Table 3.1. We used Smith's method[43] for effective dielectric function of the interior-nanogap region of DAG NP, and the interior-nanogap region was modelled as a mixture of gold and water. For metal-rich mixtures, an average unit within the interior nanogap was considered as spherical dielectric inclusion surrounded by spherical shell of the metal. The effective dielectric function is the value that does not alter the electric field under replacement the unit structure with homogeneous effective medium. This model mostly targets metal-rich mixtures but also applicable to dielectric-rich mixtures whose metallic parts are connected to each other and overall behaviour is conductive. Our structure is the case because the mixture within interior-nanogap is of thin shell form and squeezed between metallic core and shell and each inclusion can be conductive.

3.3. Results and Discussion

Dealloying-based synthesis of nanoparticles with interlayer-free interior nanogap

To synthesise the DAG NPs, we first formed CAS NPs through a co-reduction process involving the simultaneous reduction of $HAuCl_4$ and $AgNO_3$ on 4-MPy-modified AuNPs (MPy-AuNPs) (Figure 3.2a). The average size of CAS NPs, as measured from transmission electron microscopy (TEM) images, was ~87.0 nm (Figure 3.3), while the atomic composition of the shell region was estimated to be $Au_{77.2}Ag_{22.8}$ (Table 3.1). Interestingly, the reduced Au and Ag atoms were not evenly distributed throughout the entire shell region (Figure 3.2b and Figure 3.4a). An energy-dispersive X-ray spectroscopy (EDX) line scan performed across the centres of the CAS NPs showed that most of the Ag atoms were located near the Au core, with the number of Au atoms decreasing near the Au core (Figure 3.2c, the blue dotted box). In general, a higher standard reduction potential of the Au precursor results in faster reduction as compared to the case for the Ag precursor ($AuCl_4^-$/Au = 0.99 V and Ag^+/Ag = 0.8 V versus standard hydrogen electrode).[36] The strong affinity between Ag and the pyrrolidone groups of polyvinylpyrrolidone (PVP) help increase the reduction rate of the Ag precursor in the early stage,[37-39] which results in the accumulation of Ag atoms at a faster rate near the Au core. This result is in good agreement with previously reported results.[40] To examine this phenomenon in more detail, we monitored the changes in the extinction peak of the CAS NPs during the alloy shell formation process (Figure 3.5). In the early stage of the formation process, the extinction peak exhibited a rapid blue shift, suggesting the formation of Ag layers. As the reaction progressed, the extinction peak underwent a gradual red shift, with the intensity of the peak increasing; this was indicative of the formation of larger CAS NPs.

Next, we introduced ferric nitrate [$Fe(NO_3)_3$] into the CAS NPs to selectively dissolve the Ag atoms (Figure 3.1). It can be seen from Figure 3.2d that the Ag-etched CAS NPs have a nanogap present between the core and the shell via the dealloying process. The average size of the DAG NPs (~87.2 nm) was similar to that of the CAS NPs, with the interior nanogap and the shell size of the DAG NPs being ~2.1 and 20.1 nm, respectively (Figure 3.2j). The EDX elemental maps of the DAG NPs confirm the Ag atoms near the Au core were almost completely etched away (Figure 3.2e and Figure 3.4b), and the EDX line scan profile indicates that the number of Ag atoms near the Au core dramatically decreased after the dealloying reaction (Figure 3.2f, blue dotted box); the proportion of Ag atoms in the shell region was lower as compared to that in the CAS NPs (Table 3.1). Furthermore, the Au-Lα curve for the area near the Au core was valley-shaped, when the Ag-Lα peak disappeared (Figure 3.2f, blue dotted box), confirming that the interior nanogap is formed by the highly selective removal of Ag atoms near the Au core. In contrast to the case for the DAG NPs, an interior nanogap was not observed in the case of the gap-less Au/Au core/shell NPs (gap-less AuNPs), whose shell was composed only of Au and not a Au-Ag alloy (Figure 3.2g). The average size of the gap-less AuNPs was also similar to that of the CAS NPs (Figure 3.3), with the shell being composed entirely of Au atoms (Figure 3.2h, Figure 3.4c and Table 3.1). Further, a valley-like Au-Lα plot was not observed (Figure 3.2i, blue dotted box), confirming that the NPs had a nanogap-less structure. When $Fe(NO_3)_3$ was introduced into the as-synthesised gap-less AuNPs, there was no change in the morphology or the ultraviolet-visible (UV-Vis) and SERS spectra of the NPs, suggesting that the ferric nitrate-based dealloying reaction only dissolves Ag (Figure 3.6). This synthesis strategy led to the fabrication of DAG NPs in a yield of around 95% (Figure 3.2k). The *d*-spacing of the adjacent lattice fringes of the DAG NPs was 0.235 nm and their selected-area electron diffraction (SAED)

was ring-like; the former corresponded to the (111) planes of a face-centred cubic structure while the latter was indicative of polycrystallinity (Figure 3.2l).

To investigate the evolution of the interior nanogap, we monitored the structural changes as the CAS NPs transformed into DAG NPs through the dealloying reaction while increasing the amount of $Fe(NO_3)_3$ added (Figure 3.7). The mechanism proposed to explain the formation of the interior-nanogap structure is shown below (Figure 3.1, see the proposed mechanism in the black dotted box). Once the $Fe(NO_3)_3$ solution is injected into the CAS NPs, the Ag atoms near the shell surface start getting dissolved by the $Fe(NO_3)_3$ (green line in schematic of proposed mechanism), and $Fe(NO_3)_3$ penetrates the CAS NPs through the Ag-etched sites. As the dealloying reaction progresses, pinhole-like vacancies (the black dotted open circles in the proposed mechanism) generated at the Ag-etched sites diffuse inward (the blue lines in the proposed mechanism) while metal atoms (mainly Ag atoms) diffuse outward because of the nanometre-scale Kirkendall effect.[41] Because the diffusion of Ag in Au is faster than that of Au in Ag in the case of the Au-Au alloy system, the net flux of the metals (Au and Ag) is mainly dependent on the diffusion rate of Ag; this results in a net flux of vacancies from the shell surface to the Au core.[41] Thus, the diffused Ag atoms are continually removed by the $Fe(NO_3)_3$ (the green dotted lines in the proposed mechanism). Meanwhile, Au atoms diffuse to a smaller degree and interconnect with each other to minimise their surface energy. As this reaction continues, the accumulated vacancies near the Au core eventually result in the formation of a nanogap, while the interconnected Au atoms form a dense shell. In similar to the proposed mechanism, the Ag atoms were partially etched and formed an incomplete interior nanogap when a small amount of $Fe(NO_3)_3$ (5 mM) was used. However, the number of dissolved Ag atoms was higher (10 mM) and an interior nanogap was uniformly formed when a large amount of $Fe(NO_3)_3$ was used (>15 mM) (Figure 3.7).

Owing to the morphological differences between the structures with (DAG NPs) and without (CAS NPs and gap-less AuNPs) a nanogap, the UV-Vis spectra of these structures were also different (Figure 3.8a). Further, with formation of the shell structure, the colour of the particle solution changed from pink (MPy-AuNPs) to dark pink (CAS NPs), then to blue-violet (DAG NPs), and finally to red-violet (gap-less AuNPs), as shown in Figure 3.8a. Furthermore, the extinction peaks of the NPs with the shell structure were red-shifted compared to those of the shell-less NPs (λ = 528, 549, 554, and 571 nm for the MPy-Au, CAS, DAG, and gap-less AuNPs, respectively); however, a new extinction shoulder peak was observed at ~700 nm in the case of NPs with the interior nanogap (DAG NPs). To elucidate the origin of this plasmonic peak in the case of the DAG NPs and to identify the optical properties of the nanogap region, we performed a simulation based on the Mie theory.[42] In here, we assumed that metal residues are remained at the interior-nanogap region due to the incomplete etching or nature of dealloying reaction, and that metal residues may interconnect core and shell in the form of a randomly distributed web-like pattern at the atomic level. Thus, the interior-nanogap region can be modelled as a mixture of metal residues and water, and effective dielectric function of the gap region can be calculated followed by Smith's approach,[43] which can describe metallic behaviour of mixtures with low metallic volume fraction (see details in Experimental section). Generally, due to a new plasmonic mode generated in the nanogap, a new extinction peak appears at longer wavelength region (~950 nm) in case of interior-nanogap structure of which nanogap is filled with water (Figure 3.9).[29] However, in case of mixture of metal residues and water, the resonance peak was blue-shifted from longer wavelength region by changing the optical/physical state (e.g., effective dielectric function) of the nanogap. In addition, the resonance peaks were continuously red-shifted as metal composition within nanogap decreased (Figure 3.8b). This phenomenon was well-matched with changes in the UV-Vis spectra of DAG NPs obtained from

different degree of dealloying reaction (Figure 3.7). Since the degree of etching of individual DAG NP in solution might be slightly different from each other, we expect that the shoulder-shaped broad peak from experimental result came from superposition of UV-Vis spectra of DAG NPs containing different metal composition within nanogap.

Figure 3.8c shows a calculated near-field EM field distribution of the DAG NP containing 12.5 mol% of metal residues within nanogap. Unlike the DAG NP of which nanogap is filled with water (Figure 3.8d), DAG NP with metal residues generated highly enhanced EM field, indicating that the metal residues within interior nanogap as well as the structural feature (i.e., formation of interior nanogap) play an important role in EM field enhancement. It should be noted that the environment of the interior nanogap is different from that of Au-NNPs.[30] In the early stage of the synthesis of Au-NNPs, the extinction spectrum shows a new plasmonic resonance peak at ~680 nm, which is caused by the anisotropically branched budding structure. On the other hand, a new extinction peak was not observed during the synthesis of the CAS NPs (Figure 3.5). These results suggest that the proposed co-reduction synthesis process results in the shell structures filled with the mixture of Au and Ag atoms, and not forming relatively large clusters such as Au branched budding structures. Thus, the interior nanogap of dealloyed NPs (DAG NPs) consists of randomly distributed metal residues which can be described by single effective dielectric function, and may result in symmetrically distributed hot spots within the interior nanogap (Figure 3.10).

SERS analysis of DAG NPs

Next, we compared the solution-state SERS signals obtained from the as-synthesised NPs with respect to the fingerprint peak at 1,097 cm^{-1} (Figure 3.11a). As compared to the SERS signal intensity of the shell-less Au NPs (MPy-AuNPs),

those of the CAS NPs, gap-less AuNPs, and DAG NPs, were ~8.6, 7.7, and 50 times higher, respectively. In this case, Raman reporter molecules (4-MPy) were positioned in the interior-nanogap region. Both types of nanogap-less NPs (CAS NPs and gap-less AuNPs) showed similar increases in the SERS intensity. Thus, it can be concluded that it is the interior nanogap that ensures a highly enhanced SERS signal and that the composition of the metallic phase has only a minor effect on the SERS phenomenon. To examine the role of interior nanogap on SERS enhancement further, we placed the Raman reporter molecules (4-MPy) on the outmost shell surface instead of the Au core surface (Figure 3.11b). Irrespective of whether an interior nanogap was present or not, all similar-sized NPs (CAS NPs, gap-less AuNPs, and DAG NPs) showed a similar SERS signal, which was very weak. This result clearly suggests that the markedly stronger SERS enhancement was primarily attributable to the greater enhancement of the EM field in the interior nanogap.

Owing to the highly enhanced EM field and the uniformly confined hot spots in the interior nanogap, the SERS signal of the solution of the DAG NPs could be detected even at a very low concentration (500 fM), with there being a highly linear relationship (R^2 = 0.99) between the NP concentration and the SERS signal intensity (Figure 3.11c). In addition, we obtained stable SERS signals during time-course measurements performed under continuous laser exposure (Figure 3.11d). These experimental results indicate that the DAG NPs generated highly robust and sustainable SERS signals because of the Raman molecules stably encapsulated within highly SERS-active narrow interior nanogap. This property of the DAG NPs, wherein they produce uniform and quantitatively reproducible SERS signals with high sensitivity, can be exploited for biosensing/imaging. In addition, the DAG NPs were highly responsive under excitation at a wavelength of 785 nm; this suggests that they should be suitable for use for *in*/*ex vivo* and *in vitro* SERS imaging as well as photothermal therapeutic probes.[44] On the other hand, the

DAG NPs did not generate a detectable signal under excitation at a wavelength of 514 nm (Figure 3.12). Because the near-field enhancement of the SERS effect is determined by the plasmonic excitation mode near the resonance peak,[45] we believe that the 514-nm laser, whose wavelength is very different from that corresponding to the near-field resonance peak induced by the plasmonic excitation mode of the interior nanogap, could not generate a sufficiently strong EM field in the interior-nanogap region.

Single-particle-level SERS analysis of DAG NPs

To investigate the optical properties of the DAG NPs in more detail, we performed an analysis of the SERS spectrum of the DAG NPs at the single-particle level using an atomic force microscopy (AFM)-correlated nano-Raman instrument (Figure 3.13a). To acquire the SERS spectra of the individual DAG NPs, we first accurately matched the end of the AFM tip with the focal spot of the objective lens (see details in Experimental section). Then, we simultaneously obtained the AFM topographical image and the Rayleigh scattering image (Figure 3.13b). The representative tapping-mode AFM image (10×10 μm^2) indicated that the individual DAG NPs were well dispersed and did not overlap in the laser exposure focal spot (~ 250 nm); this allowed for the SERS spectra of the individual NPs to be measured with accuracy. Furthermore, high-magnification AFM images confirmed the spherical shape of the DAG NPs, with their height profile matching well with their overall size as determined from the TEM images (Figure 3.13c). We measured the SERS spectra of 110 individual DAG NPs and calculated the enhancement factor (EF) values for the fingerprint peak at 1,003 cm^{-1} (see details in Experimental section).

Figure 3.13d shows the distribution diagram of the EF values of the individual DAG NPs. It should be noted that the individual NPs exhibited

detectable high-intensity SERS signals and that the EF values of the DAG NPs showed a narrow distribution, ranging from 1.1×10^8 to 2.5×10^9 for 90.0% of the population. Further, the distribution ranged from 1.1×10^8 to 5.3×10^9 for 97.3% of the population. Moreover, the EF values were as high as 2.1×10^{10} in some of the cases. It is worth noting that the narrow distribution of the EF values arises from the uniformly confined interior nanogap. Thus, such structures with a nanogap can be exploited for use as reproducible and reliable SERS probes. Importantly, the EF values obtained from DAG NPs are as high and narrow as those of Au-NNPs, even though the EF values of DAG NPs were conservatively underestimated; we assumed that the maximum numbers of 4-MPy molecules are packed on the AuNPs core when calculating SERS EF values (see details in Experimental section). In addition, the strong SERS signals were generated in spite of the use of non-resonance Raman molecules (4-MPy) of which optical cross-section is very small, unlike the Au-NNPs. The EF values of the DAG NPs are two to three orders of magnitude higher than those reported previously for the same Raman reporter molecule (4-MPy).[46-50] It is now widely accepted that an EF of 10^6 to 10^8 may be sufficient for single-molecule detection.[22,30,51] In this respect, the as-synthesised DAG NPs, which generated very strong SERS signals with high sensitivity, would be promising as SERS probes for use in various analytical applications. Further, we investigated the incident-laser-polarisation-dependent SERS characteristics of the DAG NPs at the single-particle level (Figure 3.13e). In the case of anisotropic or assembled nanostructures, the optical properties are dependent of the geometric configuration.[52-55] In contrast, the DAG NPs exhibited stable and uniform SERS signals regardless of the polarisation of the incident laser, owing to the symmetrically distributed hot spots within the interior nanogap. This polarisation-independent property also makes the DAG NPs suitable for use as analytical probes at the single-particle level.

SERS-based ultrasensitive DNA detection

Given the enhanced SERS characteristics of the DAG NPs, we performed SERS-based ultrasensitive DNA detection assays using the NPs. In order to detect single-strand target DNA, we used DNA-modified magnetic microparticles (DNA-MMPs) and DAG Raman probes (DAG probes) to capture the target DNA strands (hepatitis A virus; HAV), based on a typical sandwich-hybridisation assay (Figure 3.14a, see details in Experimental section). To confirm the formation of the sandwich hybridisation complexes (target-captured DAG probe-MMP complexes) and its ability to undergo target-DNA-specific hybridisation, we performed hybridisation assays with complementary (HAV) and non-complementary (HBV) sequence DNA (Figure 3.14b and c). In the presence of the complementary DNA, the solution turned colourless when an external magnetic field was applied to it, indicating the formation of the sandwich hybridisation complexes (Figure 3.14b). In the presence of the non-complementary DNA, however, the solution remained coloured even after the MMPs were collected with a magnet, meaning that the DAG probes were not captured by the MMPs owing to the presence of the non-complementary DNA (Figure 3.14c). Moreover, the formation of the sandwich hybridisation complexes could be seen clearly in scanning electron microscopy (SEM) images according to the sequence of linker DNA. These results indicate that the proposed DNA detection method is suitable for use in sequence-specific DNA detection assays. Figure 3.14d shows the changes in the SERS intensity at 1,003 cm^{-1} for target DNA (HAV) solutions of different concentrations (10 aM to 1 pM, black squares). The SERS intensity quantitatively decreases with a decrease in the concentration of the target DNA over a wide range (100 aM to 1 pM). On the other hand, with the intensity of the SERS signal was very low during control experiments in which the target DNA was replaced with non-complementary DNA (HBV) strands (1 pM, red circular dot). The limit of detection (LOD) was

approximatively 100 aM, in contrast to the case for the control experiment. These results further confirm that the dealloying-based SERS-active plasmonic NPs fabricated in this study can be used as ultrasensitive DNA sensors in target-selective analytical SERS probes.

SERS-based target-specific cell imaging

Lastly, we performed SERS-based target-specific cell imaging using surface-functionalised DAG NPs (Figure 3.15a). To evaluate the integrin-targeting specificity of the DAG NPs, cyclo(Arg-Gly-Asp-D-Phe-Lys) (c(RGDyK); hereafter denoted as cRGD) peptide, which specifically binds to $\alpha_v\beta_3$ integrin (overexpressed in metastatic and endothelial tumour cells)[56] was attached onto the surfaces of the DAG NPs. Next, we introduced cRGD-functionalised DAG NPs into different cell lines, namely, U87MG (high integrin $\alpha_v\beta_3$ expression) and MCF-7 (integrin $\alpha_v\beta_3$ negative) (see details in Experimental section). Owing to the high expression of integrin $\alpha_v\beta_3$ in the U87MG cells and its preferential binding affinity with respect to cRGD peptide, a strong SERS signal was observed in the case of the integrin-$\alpha_v\beta_3$-positive U87MG cells, confirming the target-specific binding ability of the cRGD-functionalised DAG NPs (Figure 3.15b and d). On the other hand, a SERS signal was barely detected in the case of the integrin-$\alpha_v\beta_3$-negative MCF-7 cells, confirming that the cRGD-functionalised DAG NPs showed good target selectivity for SERS-based cell imaging (Figure 3.15c and d). These results suggest that the surfaces of the DAG NPs can be readily functionalised with targeting moieties, making the NPs suitable for use as SERS-based target-specific imaging agents. In addition, the cRGD-functionalised DAG NPs generated uniform SERS signals steadily even though they were continuously exposed by external laser for a long time (Figure 3.15e). Unlike fluorescence-based imaging probes, which are limited to generate stable signal over long periods of time due to the

photobleaching and photoblinking, this experimental result indicates that the DAG NPs are suitable for a long-term cell imaging. Owing to the enhanced SERS performance, DAG NPs generated stronger SERS signal enough to cell imaging compared to similar-sized conventional AuNPs (Figure 3.15f, g and Figure 3.16). It is worth noting that SERS-based cell imaging could be performed despite the use of low-power lasers (400 μW) and short exposure times (1 s for each pixel), suggesting a potential availability for diminishing cell damage during imaging.

3.4. Conclusions

We developed a dealloying-based strategy for synthesising highly SERS-active NPs (DAG NPs) containing a uniformly confined interior nanogap in high yields. This strategy is a very simple, cheap, and fast one for fabricating an interlayer-free interior nanogap without using additional materials, such as DNA or a polymer or silica shell. It was confirmed that the interior nanogap was formed by the selective removal of Ag atoms from the Au-Ag alloy shell. The NPs with the interior nanogap showed a highly enhanced SERS signal as compared to those of the shell-less and nanogap-less NPs, owing to the strong EM field generated in the interior nanogap by strong plasmonic coupling between the core and the shell. Furthermore, the DAG NPs, which emitted robust, stable, and quantitatively reproducible SERS signals and exhibited a highly enhanced and narrowly distributed EF, showed good performances during target-specific DNA detection (with the LOD being of the order of attomolar) and SERS-based cell imaging. It can therefore be concluded that the proposed method opens new avenues for the design and synthesis of highly SERS-active NPs that can be employed as reliable high-sensitivity SERS probes that yield quantitatively reproducible results for different analytical applications, including biosensing, *in*/*ex vivo* and *in vitro* SERS imaging, and photothermal therapeutics. The conventional DNA-based method for synthesising NPs with an interior nanogap can only produce structures with very thin nanogaps (~ 1 nm) and does not yield structures with thin shells, owing to the nature of the synthesis mechanism. In contrast, the dealloying-based synthesis strategy reported here allows for fine control of the width of the interior nanogap and the shell thickness of the Ag-etched products by adjusting the initial composition of Ag/Au in the alloy shell region. The effects of the nanogap width and the shell thickness on the SERS characteristics of the thus-synthesised NPs with an interior nanogap are being investigated.

3.5. References

1. Nam, J.-M.; Oh, J.-W.; Lee, H.; Suh, Y. D. *Acc. Chem. Res.* **2016**, *49*, 2746.
2. Huang, Y.-F.; Zhang, M.; Zhao, L.-B.; Feng, J.-M.; Wu, D.-Y.; Ren, B.; Tian, Z.-Q. *Angew. Chem.-Int. Edit.* **2014**, *53*, 2353.
3. Liu, N.; Tang, M. L.; Hentschel, M.; Giessen, H.; Alivisatos, A. P. *Nat. Mater.* **2011**, *10*, 631.
4. Bao, W.; Melli, M.; Caselli, N.; Riboli, F.; Wiersma, D. S.; Staffaroni, M.; Choo, H.; Ogletree, D. F.; Aloni, S.; Bokor, J.; Cabrini, S.; Intonti, F.; Salmeron, M. B.; Yablonovitch, E.; Schuck, P. J.; Weber-Bargioni, A. *Science* **2012**, *338*, 1317.
5. Li, J.; Cushing, S. K.; Meng, F.; Senty, T. R.; Bristow, A. D.; Wu, N. *Nat. Photonics* **2015**, *9*, 601.
6. Kneipp, J.; Kneipp, H.; Kneipp, K. *Chem. Soc. Rev.* **2008**, *37*, 1052.
7. Le Ru, E. C.; Etchegoin, P. G. *Annu. Rev. Phys. Chem.* **2012**, *63*, 65.
8. Tripp, R. A.; Dluhy, R. A.; Zhao, Y. *Nano Today* **2008**, *3*, 31.
9. Kumar, A.; Kim, S.; Nam, J.-M. *J. Am. Chem. Soc.* **2016**, *138*, 14509.
10. Zhang, X.; Young, M. A.; Lyandres, O.; Van Duyne, R. P. *J. Am. Chem. Soc.* **2005**, *127*, 4484.
11. Zheng, J.; He, L. *Compr. Rev. Food. Sci. Food Saf.* **2014**, *13*, 317.
12. Kleinman, S. L.; Frontiera, R. R.; Henry, A.-I.; Dieringer, J. A.; Van Duyne, R. P. *Phys. Chem. Chem. Phys.* **2013**, *15*, 21.
13. Talley, C. E.; Jackson, J. B.; Oubre, C.; Grady, N. K.; Hollars, C. W.; Lane, S. M.; Huser, T. R.; Nordlander, P.; Halas, N. J. *Nano. Lett.* **2005**, *5*, 1569.
14. Lal, S.; Grady, N. K.; Kundu, J.; Levin, C. S.; Lassiter, J. B.; Halas, N. J. *Chem. Soc. Rev.* **2008**, *37*, 898.
15. Wei, H.; Xu, H. *Nanoscale* **2013**, *5*, 10794.

16. Scarabelli, L.; Coronado-Puchau, M.; Giner-Casares, J. J.; Langer, J.; Liz-Marzan, L. M. *ACS Nano* **2014**, *8*, 5833.

17. Liu, K.; Bai, Y.; Zhang, L.; Yang, Z.; Fan, Q.; Zheng, H.; Yin, Y.; Gao, C. *Nano. Lett.* **2016**, *16*, 3675.

18. Lee, C.; Robertson, C. S.; Nguyen, A. H.; Kahraman, M.; Wachsmann-Hogiu, S. *Sci. Rep.* **2015**, *5*, 11644.

19. Yue, W.; Wang, Z.; Whittaker, J.; Lopez-royo, F.; Yang, Y.; Zayats, A. V. *J. Mater. Chem. C* **2017**, *5*, 4075.

20. Romero, I.; Aizpurua, J.; Bryant, G. W.; de Abajo, F. J. G. *Opt. Express* **2006**, *14*, 9988.

21. Shanthil, M.; Thomas, R.; Swathi, R. S.; Thomas, K. G. *J. Phys. Chem. Lett.* **2012**, *3*, 1459.

22. Lim, D.-K.; Jeon, K.-S.; Kim, H. M.; Nam, J.-M.; Suh, Y. D. *Nat. Mater.* **2010**, *9*, 60.

23. Zhao, B.; Shen, J.; Chen, S.; Wang, D.; Li, F.; Mathur, S.; Song, S.; Fan, C. *Chem. Sci.* **2014**, *5*, 4460.

24. Su, J.; Wang, D.; Nörbel, L.; Shen, J.; Zhao, Z.; Dou, Y.; Peng, T.; Shi, J.; Mathur, S.; Fan, C.; Song, S. *Anal. Chem.* **2017**, *89*, 2531.

25. Bardhan, R.; Mukherjee, S.; Mirin, N. A.; Levit, S. D.; Nordlander, P.; Halas, N. J. *J. Phys. Chem. C* **2010**, *114*, 7378.

26. Song, J.; Duan, B.; Wang, C.; Zhou, J.; Pu, L.; Fang, Z.; Wang, P.; Lim, T. T.; Duan, H. *J. Am. Chem. Soc.* **2014**, *136*, 6838.

27. Zhou, Y.; Lee, C.; Zhang, J.; Zhang, P. *J. Mater. Chem. C* **2013**, *1*, 3695.

28. Gandra, N.; Singamaneni, S. *Adv. Mater.* **2013**, *25*, 1022.

29. Lin, L.; Zapata, M.; Xiong, M.; Liu, Z.; Wang, S.; Xu, H.; Borisov, A. G.; Gu, H.; Nordlander, P.; Aizpurua, J.; Ye, J. *Nano. Lett.* **2015**, *15*, 6419.

30. Lim, D.-K.; Jeon, K.-S.; Hwang, J.-H.; Kim, H.; Kwon, S.; Suh, Y. D.; Nam, J.-M. *Nat. Nanotechnol.* **2011**, *6*, 452.

31. Oh, J.-W.; Lim, D.-K.; Kim, G.-H.; Suh, Y. D.; Nam, J.-M. *J. Am. Chem. Soc.* **2014**, *136*, 14052.

32. Lee, J.-H.; Oh, J.-W.; Nam, S. H.; Cha, Y. S.; Kim, G.-H.; Rhim, W.-K.; Kim, N. H.; Kim, J.; Han, S. W.; Suh, Y. D.; Nam, J.-M. *Small* **2016**, *12*, 4726.

33. Hurst, S. J.; Lytton-Jean, A. K. R.; Mirkin, C. A. *Anal. Chem.* **2006**, *78*, 8313.

34. Sun, Y.; Wiley, B.; Li, Z.-Y.; Xia, Y. *J. Am. Chem. Soc.* **2004**, *126*, 9399.

35. Sun, Y.; Xia, Y. *J. Am. Chem. Soc.* **2004**, *126*, 3892.

36. Sun, Y.; Mayers, B.; Xia, Y. *Adv. Mater.* **2003**, *15*, 641.

37. Zhang, Z.; Zhao, B.; Hu, L. *J. Solid State Chem.* **1996**, *121*, 105.

38. Silvert, P.-Y.; Herrera-Urbina, R.; Tekaia-Elhsissen, K. *J. Mater. Chem.* **1997**, *7*, 293.

39. Carotenuto, G.; Pepe, G. P.; Nicolais, L. *Eur. Phys. J. B* **2000**, *16*, 11.

40. Kim, M.; Ko, S. M.; Nam, J.-M. *Nanoscale* **2016**, *8*, 11707.

41. Gonzalez, E.; Arbiol, J.; Puntes, V. F. *Science* **2011**, *334*, 1377.

42. Bohren, C. F.; Huffman, D. R., *Absorption and Scattering of Light By Small Particles* (Wiley, New York, 1983).

43. Smith, G. B. *J. Phys. D-Appl. Phys.* **1977**, *10*, L39.

44. Xue, X.; Wang, F.; Liu, X. *J. Mater. Chem.* **2011**, *21*, 13107.

45. Lombardi, A.; Demetriadou, A.; Weller, L.; Andrae, P.; Benz, F.; Chikkaraddy, R.; Aizpurua, J.; Baumberg, J. J. *ACS Photonics* **2016**, *3*, 471.

46. Orendorff, C. J.; Gearheart, L.; Jana, N. R.; Murphy, C. J. *Phys. Chem. Chem. Phys.* **2006**, *8*, 165.

47. Lu, G.; Li, C.; Shi, G. *Chem. Mat.* **2007**, *19*, 3433.

48. Rodrigues, D. C.; Andrade, G. F. S.; Temperini, M. L. A. *Phys. Chem. Chem. Phys.* **2013**, *15*, 1169.

49. Liu, H.; Zhang, X.; Zhai, T.; Sander, T.; Chen, L.; Klar, P. J. *Nanoscale* **2014**, *6*, 5099.

50. Rodrigues, D. C.; de Souza, M. L.; Souza, K. S.; dos Santos, D. P.; Andrade, G. F. S.; Temperini, M. L. A. *Phys. Chem. Chem. Phys.* **2015**, *17*, 21294.

51. Park, W.-H.; Kim, Z. H. *Nano. Lett.* **2010**, *10*, 4040.

52. Ming, T.; Zhao, L.; Yang, Z.; Chen, H.; Sun, L.; Wang, J.; Yan, C. *Nano. Lett.* **2009**, *9*, 3896.

53. Yang, L.; Wang, H.; Fang, Y.; Li, Z. *ACS Nano* **2016**, *10*, 1580.

54. Lee, H.; Kim, G.-H.; Lee, J.-H.; Kim, N. H.; Nam, J.-M.; Suh, Y. D. *Nano. Lett.* **2015**, *15*, 4628.

55. Wei, H.; Hao, F.; Huang, Y.; Wang, W.; Nordlander, P.; Xu, H. *Nano. Lett.* **2008**, *8*, 2497.

56. Kim, Y.-H.; Jeon, J.; Hong, S. H.; Rhim, W.-K.; Lee, Y.-S.; Youn, H.; Chung, J.-K.; Lee, M. C.; Lee, D. S.; Kang, K. W.; Nam, J.-M. *Small* **2011**, *7*, 2052.

57. Lee, H.; Lee, J.-H.; Jin, S. M.; Suh, Y. D.; Nam, J.-M. *Nano. Lett.* **2013**, *13*, 6113.

58. Song, W.; Li, W.; Cheng, Y.; Jia, H.; Zhao, G.; Zhou, Y.; Yang, B.; Xu, W.; Tian, W.; Zhao, B. *J. Raman Spectrosc.* **2006**, *37*, 755.

59. Song, W.; Wang, Y.; Zhao, B. *J. Phys. Chem. C* **2007**, *111*, 12786.

60. Lee, H.; Park, J.-E.; Nam, J.-M. *Nat. Commun.* **2014**, *5*, 3367.

61. Rioux, D.; Vallières, S.; Besner, S.; Muñoz, P.; Mazur, E.; Meunier, M. *Adv. Opt. Mater*. **2014**, *2*, 176.

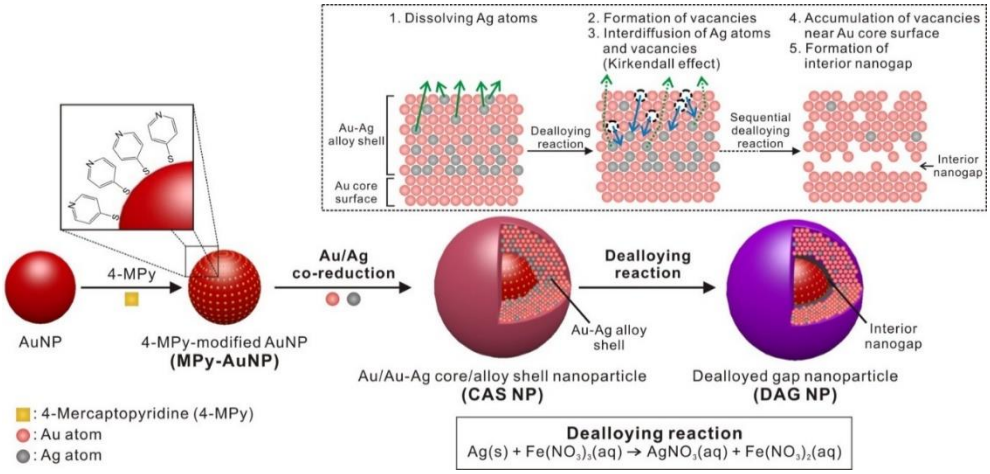

Figure 3.1. Schematic illustration of alloying/dealloying-based strategy for synthesis of Au/Au-Ag core/alloy shell nanoparticles (CAS NPs) and dealloyed gap nanoparticles (DAG NPs). The proposed mechanism of dealloying reaction is shown in black dotted box. CAS NPs are synthesised by co-reduction of Au and Ag into 4-mercaptopyridine-modified Au NPs (MPy-AuNPs) (alloying step). When Ag etchant solution ($Fe(NO_3)_3$) is added to CAS NPs, Ag atoms in Au-Ag alloy shell are selectively dissolved by Ag etching process (dealloying step). Meanwhile, Ag-etched sites (vacancies) and metal atoms (mainly Ag atoms) interdiffuse via nanometre-scale Kirkendall effect. As dealloying reaction progresses, nanometre-scaled vacancies accumulate near surfaces of MPy-AuNPs, eventually leading to formation of interior nanogap in DAG NPs.

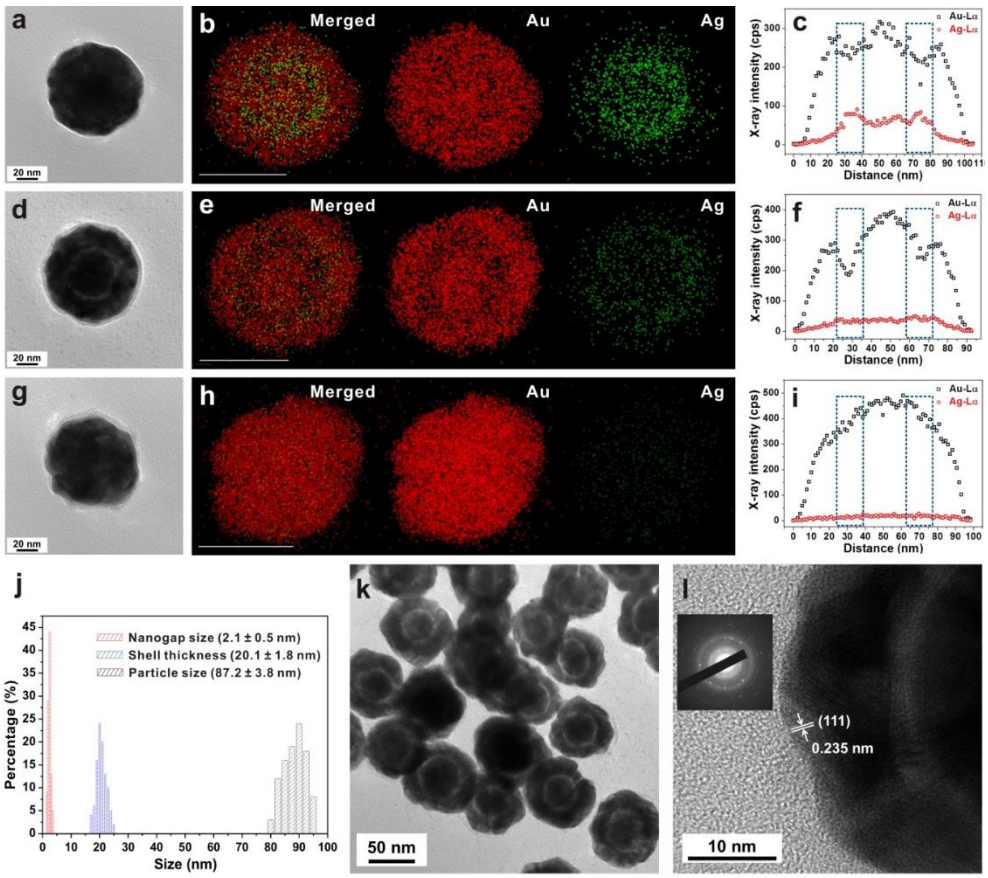

Figure 3.2. Syntheses and characterisation of CAS NPs, DAG NPs, and gap-less AuNPs. TEM and EDX elemental maps and EDX line scan profiles across centres of as-synthesised NPs: (a-c) CAS NPs, (d-f) DAG NPs, and (g-i) gap-less Au-Au core-shell NPs. Interior nanogap in DAG NPs because of dealloying reaction can be seen clearly. Ag atoms are primarily located near Au core in CAS NPs (blue dotted box in Figure 2c) and number of Ag atoms near Au core decreases after dealloying reaction (blue dotted box in Figure 2f), resulting in interior nanogap. In case of gap-less AuNPs, interior nanogap is not observed (blue dotted box in Figure 2i). The EDX maps of Ag in (h) are caused by noise-level signals. Scale bar in EDX maps is 50 nm. (j) Nanogap size, shell thickness, and particle size distribution of DAG NPs. Data were obtained from HR-TEM images of 100 individual particles. (k) TEM image of synthesised DAG NPs confirming that targeted structure was synthesised in high yield. (l) HR-TEM image of individual

DAG NP. Here, *d*-spacing of 0.235 nm for adjacent lattice fringes corresponds to (111) planes of a face-centred cubic structure. Inset shows ring-shaped SAED pattern of DAG NP, indicating that it has a polycrystalline structure.

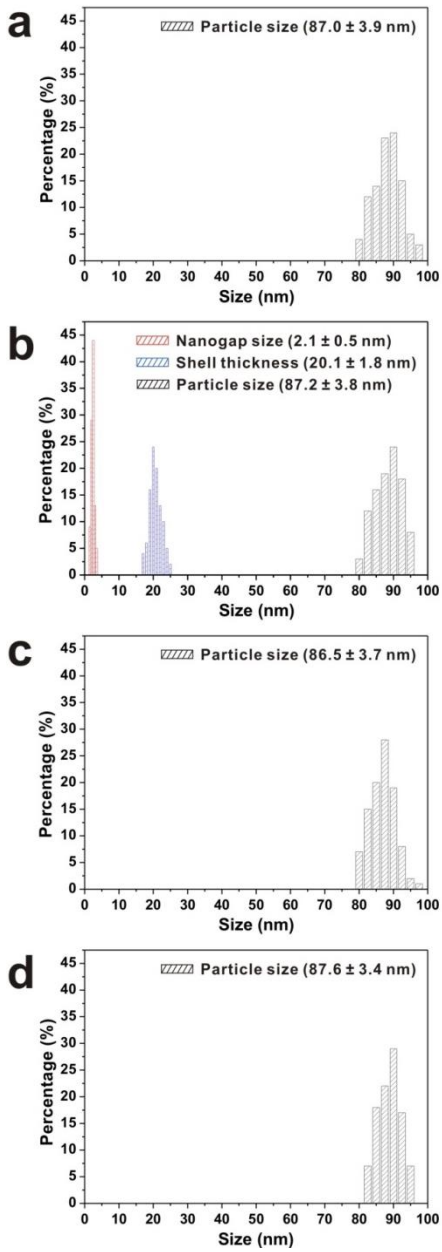

Figure 3.3. Interior nanogaps, shell thicknesses, and particle size distributions of as-synthesised NPs: (a) CAS NPs, (b) DAG NPs, (c) gap-less AuNPs before Ag etching, and (d) gap-less AuNPs after Ag etching. Data were obtained from HR-TEM images of 100 individual particles.

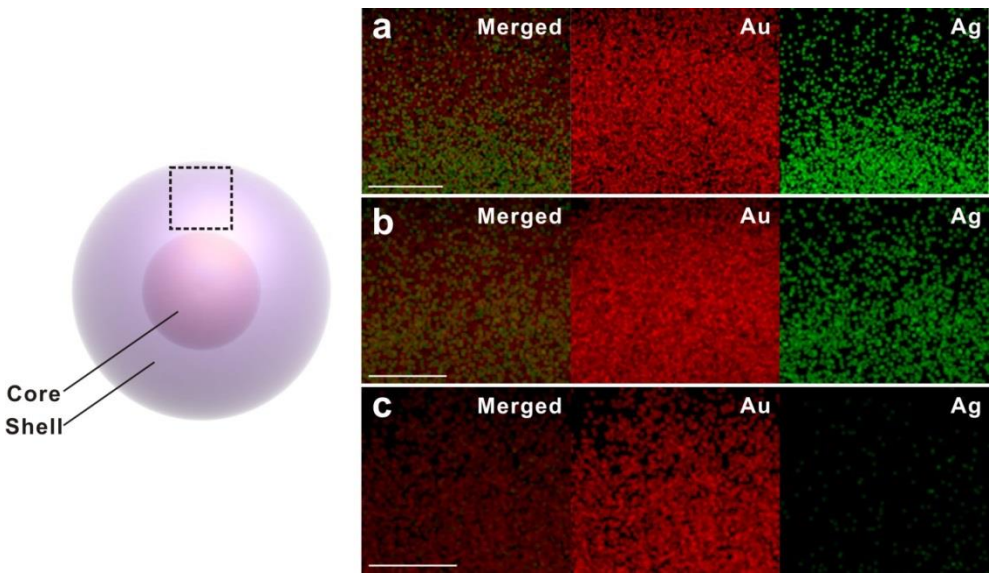

Figure 3.4. EDX elemental maps of as-synthesised NPs: (a) CAS NP, (b) DAG NP, and (c) gap-less AuNP. The maps show elemental distributions of Au and Ag in the shell region (black dotted box in left cartoon). Scale bar is 10 nm.

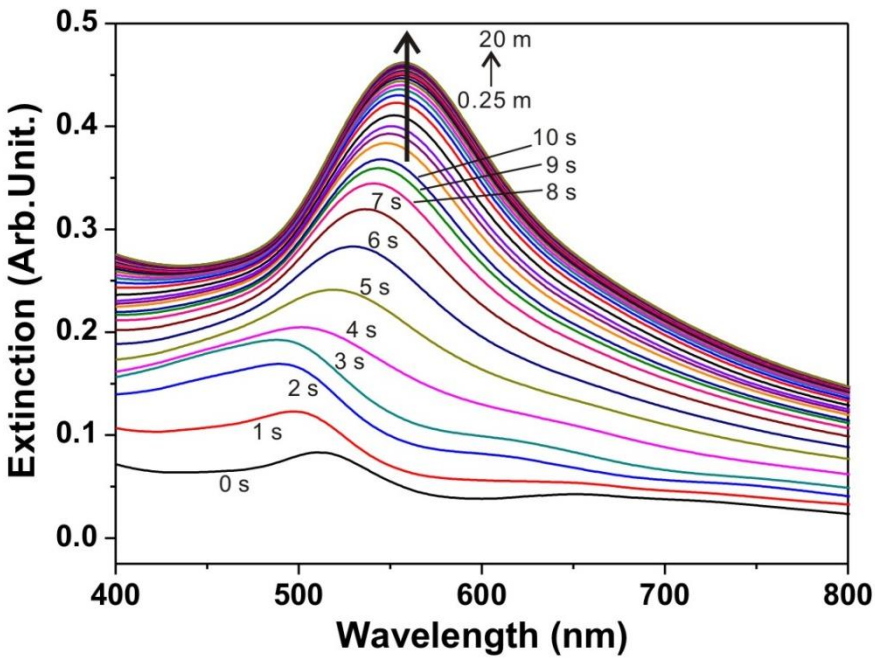

Figure 3.5. Changes in UV-Vis spectrum of Au/Au-Ag core/alloy shell NP (CAS NP) reaction mixture during alloy shell formation.

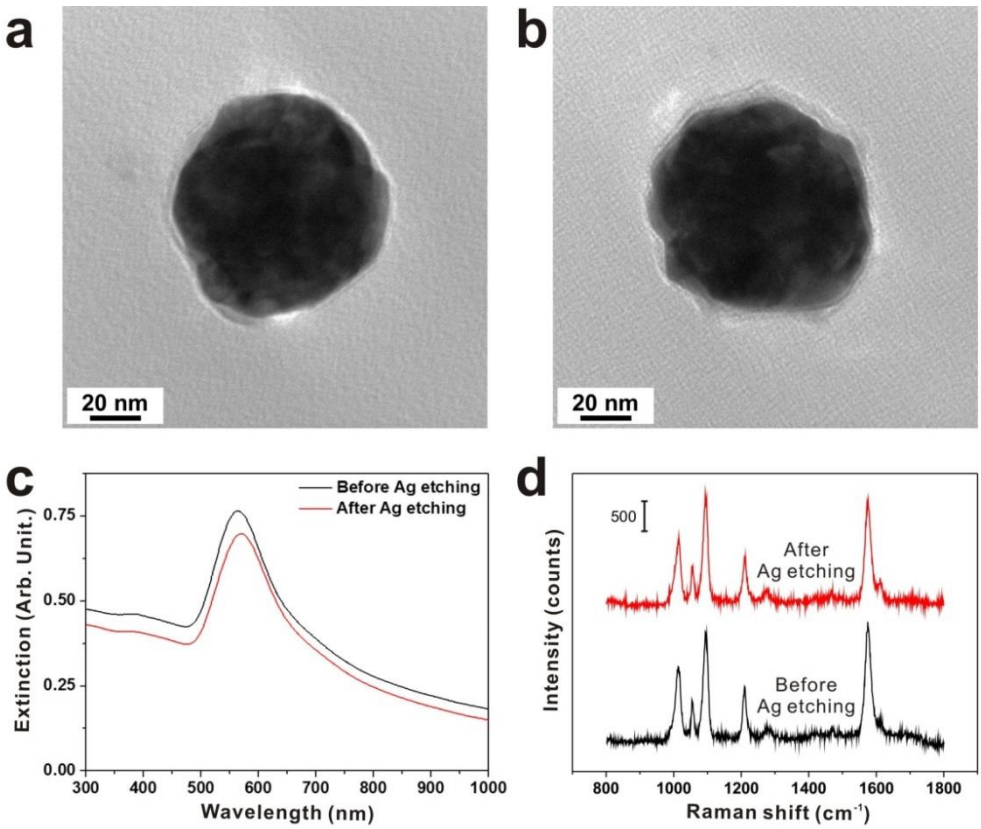

Figure 3.6. Structural changes and optical properties of gap-less AuNPs during Ag etching reaction. (a, b) TEM images of gap-less AuNPs: (a) before Ag etching and (b) after Ag etching. (c) UV-Vis spectra of gap-less AuNPs before and after Ag etching reaction. (d) Solution-based SERS spectra of gap-less AuNPs before and after Ag etching reaction. All spectra were acquired with 633-nm laser at laser power of 4 mW and exposure time of 10 s and using same particle concentration (100 pM). The morphology, UV-Vis spectra, and SERS spectra are similar, regardless of whether Ag etching reaction was performed or not, indicating that the ferric nitrate-based dealloying reaction is a Ag-specific/selective dissolution reaction.

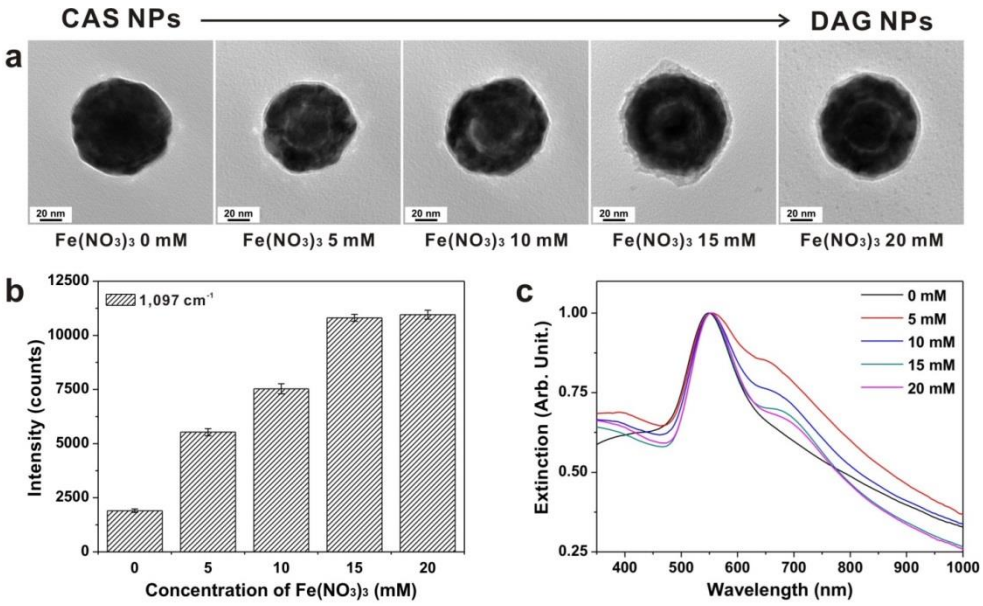

Figure 3.7. Changes in structure and optical properties of DAG NPs with dealloying reaction. (a) Structural changes in DAG NPs with increase in amount of $Fe(NO_3)_3$ added. The interior nanogap evolves gradually as the dealloying reaction progresses. (b) Interior-nanogap-formation-dependent changes in SERS intensity of DAG NPs. Solution-based SERS intensity increases with the formation of complete interior nanogap and is maximised at higher $Fe(NO_3)_3$ concentrations (more than 15 mM), indicating that the dealloying reaction is complete. SERS intensity of DAG NPs was nearly six times that of CAS NPs; this SERS enhancement is attributable to the strong and localised EM field generated in the interior nanogap. (c) Interior-nanogap-formation-dependent UV-Vis spectra of DAG NPs. The extinction peaks change slightly as the dealloying reaction progresses. By the dealloying reaction, a new extinction shoulder peak appears at ~660 nm (red line), indicating the formation of the interior nanogap; this peak is slightly red-shifted to ~700 nm and is gradually stabilised after the formation of a complete and symmetric interior nanogap (purple line).

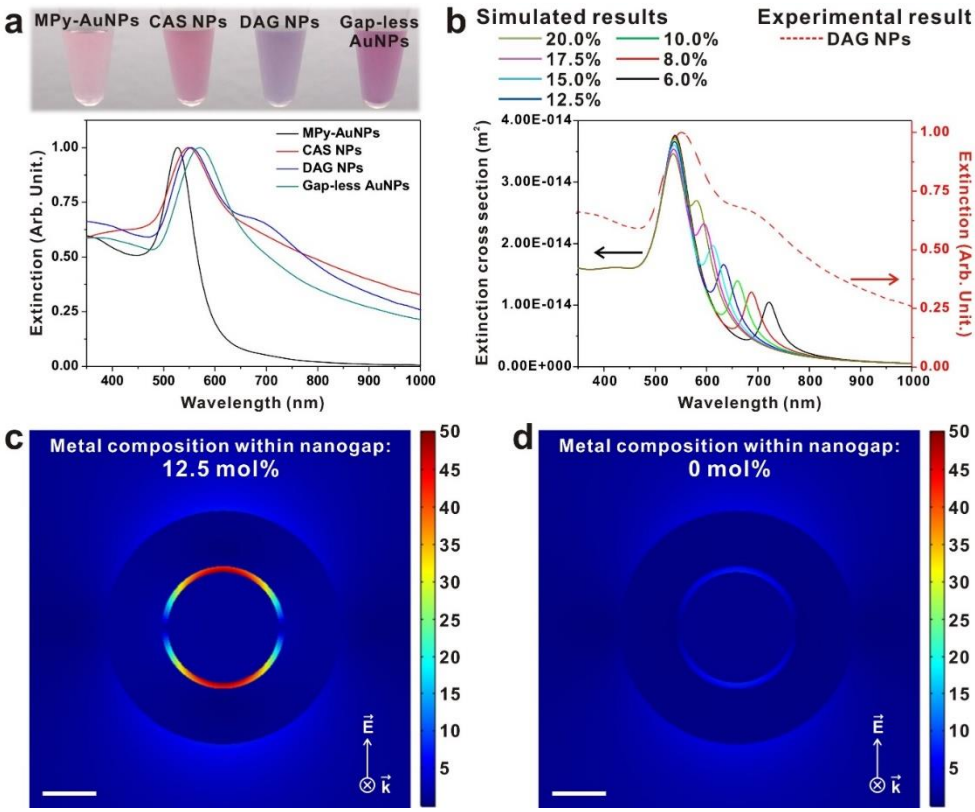

Figure 3.8. Experimental UV-Vis spectra of nanoparticles and theoretical calculation of DAG NP. (a) UV-Vis spectra of as-synthesised NPs. Inset: changes in colour of NP solutions. (b) Simulated extinction spectra of DAG NPs according to metal composition within interior-nanogap region. The interior-nanogap region are considered as a mixture of metal residues and water. (c, d) Calculated near-field EM field distribution of the DAG NP containing different composition of metal residues within interior-nanogap region: (c) 12.5 mol%, (d) 0 mol%. The excitation wavelength is 633 nm. Scale bar is 20 nm.

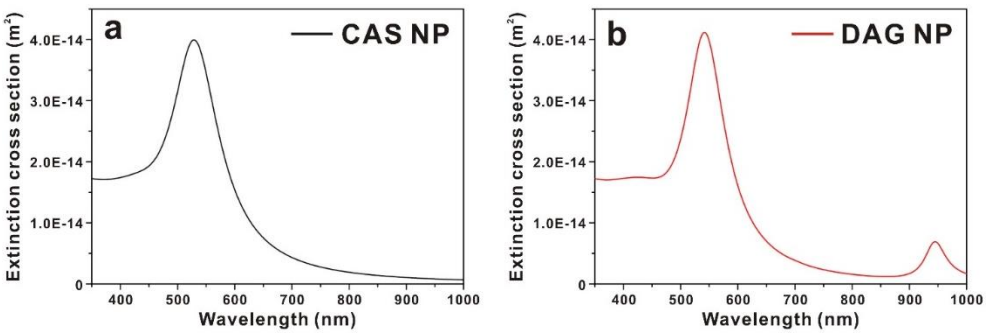

Figure 3.9. Simulated extinction spectra of as-synthesised NPs: (a) CAS NPs, (b) DAG NPs. The theoretical calculations were performed using Mie theory; the structural data used (average particle size, interior nanogap size, shell thickness, and atomic composition) for the as-synthesised NPs are listed in Figure S1 and Table S1. The background and interior-nanogap region were modelled as water with a refractive index of 1.33. It is worth noting that the new resonance peak at approximately 950 nm was observed only in the case of the DAG NPs, indicating the generation of a new plasmonic mode because of the interior nanogap.

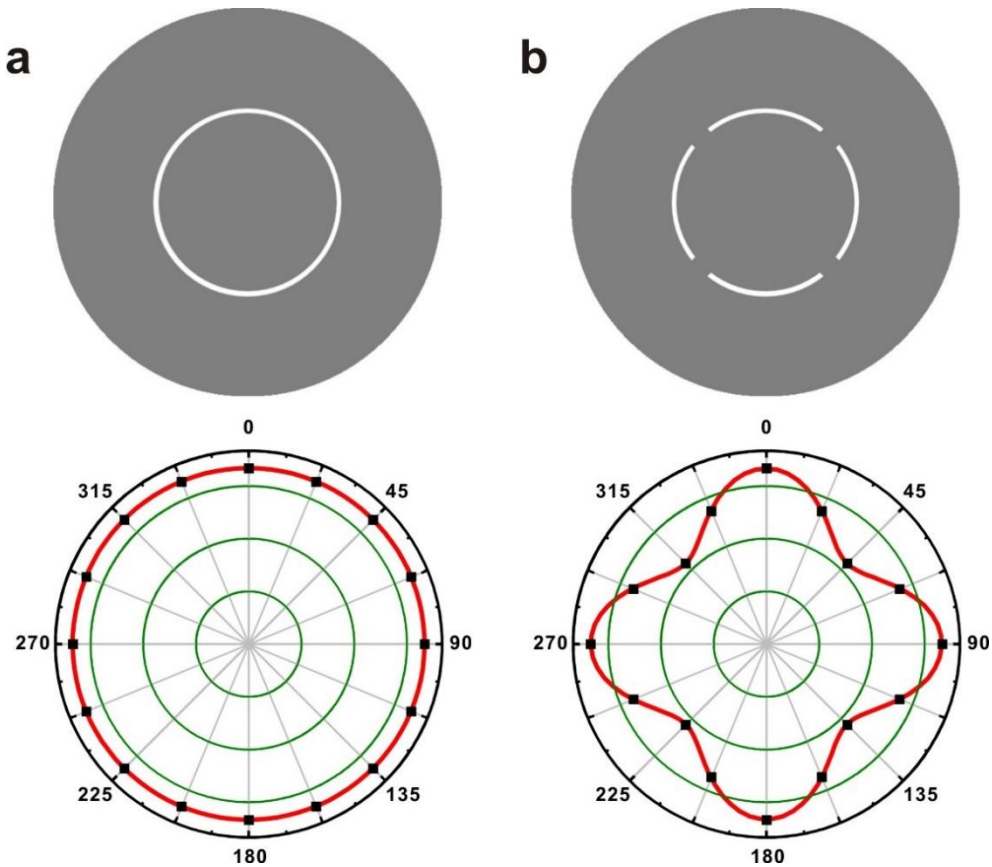

Figure 3.10. Polarisation-resolved plot of EM field at interior-nanogap region with respect to rotation angle: (a) DAG NP, (b) Au-NNP. The theoretical calculations were performed using finite element method with COMSOL, and the maximum values of EM field enhancement at each rotation angle were plotted. Analytical model for the theoretical calculations are shown (upper panel).

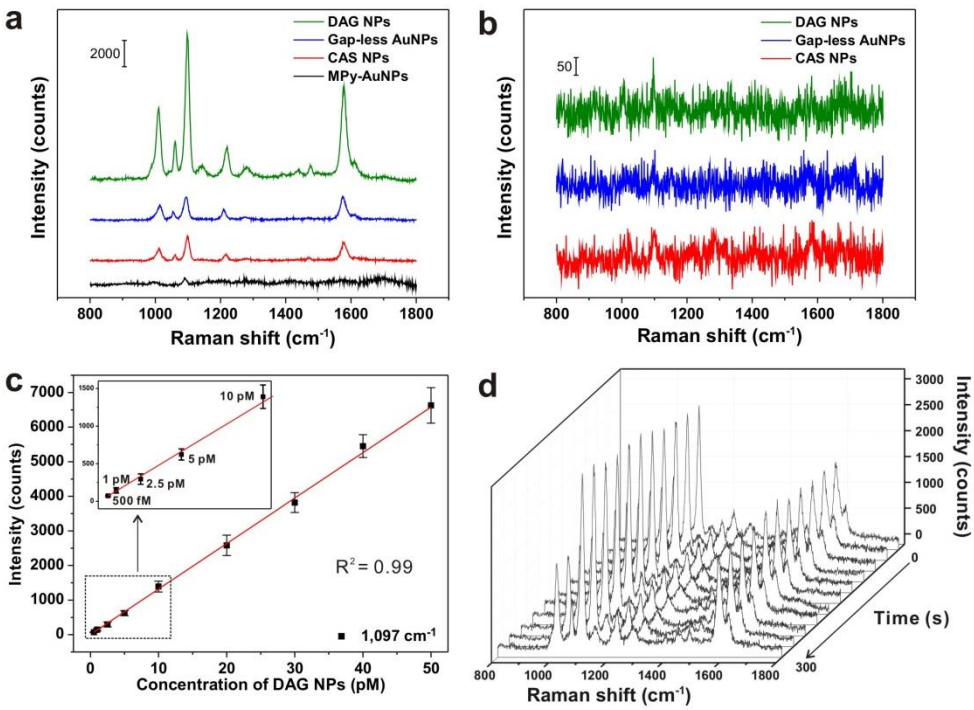

Figure 3.11. Structure, Raman molecule position, concentration, and time-dependent SERS properties of as-synthesised nanoparticles in solution. (a) SERS spectra of as-synthesised NPs in solution. Raman reporter molecules (4-MPy) were attached to surfaces of Au cores of NPs. (b) Solution-based SERS spectra of as-synthesised NPs whose outmost shell surface was modified with 4-MPy. (c) Changes in SERS signal intensity of solution of DAG NPs as function of NP concentration (500 fM to 50 pM). SERS intensity of fingerprint peak at 1,097 cm^{-1} is plotted in terms of particle concentration. (d) Time-dependent Raman profiles of DAG NPs. All spectra were acquired using 633-nm excitation laser at laser power of 4 mW and acquisition time of 10 s. Particle concentration was (a, b) 100 pM and (d) 20 pM.

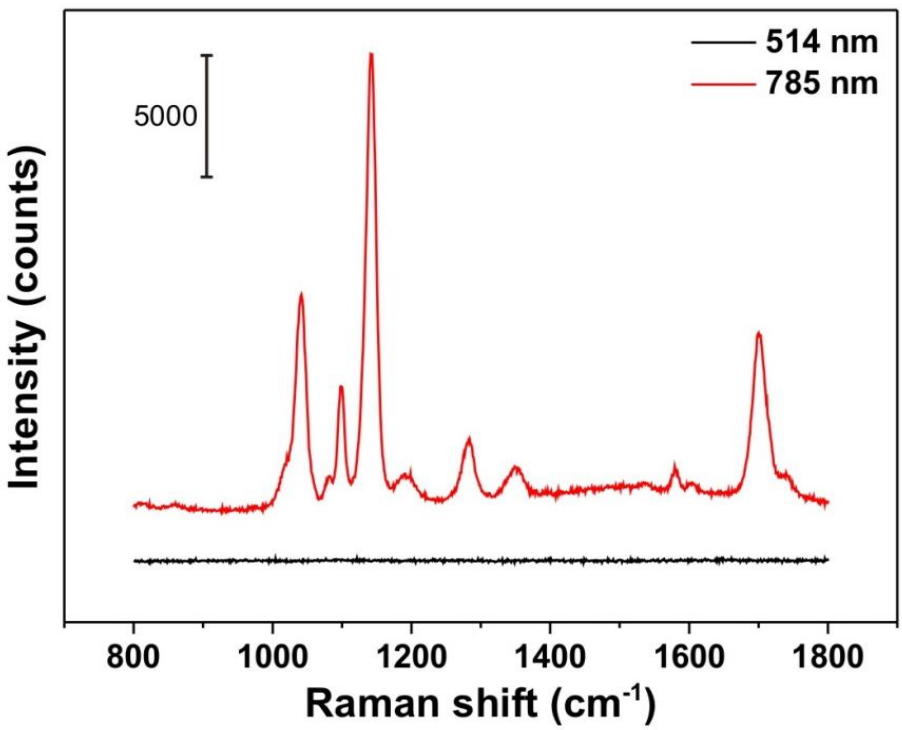

Figure 3.12. Excitation-wavelength-dependent SERS spectra of DAG NPs. The spectra were acquired using the same particle concentration (100 pM). Exposure time was 10 s and laser powers were 5 mW (514 nm) and 4 mW (785 nm).

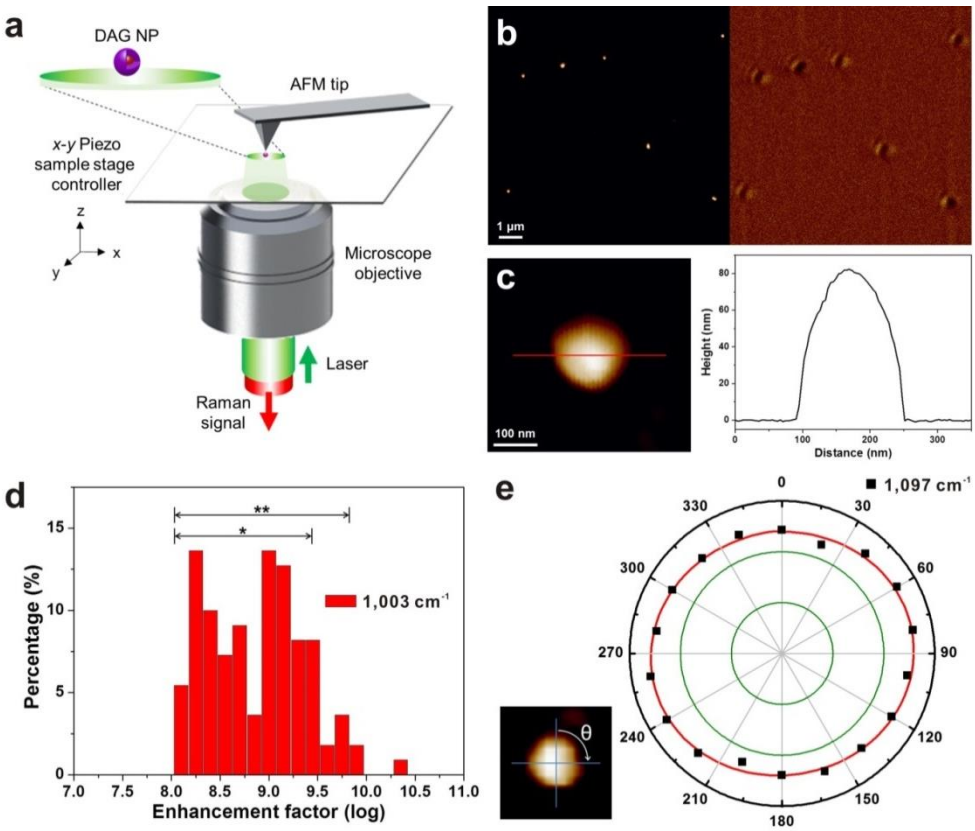

Figure 3.13. AFM-correlated nano-Raman spectroscopy-based mapping analysis, SERS enhancement factor (EF) distribution, and polarisation-resolved SERS plot of single DAG NP. (a) Instrumental setup used for AFM-correlated nano-Raman spectroscopy. (b) Topographical matching of AFM image (left) and Rayleigh scattering image (right). (c) Magnified AFM image of single DAG NP (left) and height profile across the NP (right, red line in AFM image). (d) Distribution of calculated EF values at 1,003 cm^{-1} as measured from individual DAG NPs. Asterisks indicate distribution of EF values for 90.0% (*) and 97.3% (**) of population; the EF values shows a narrow distribution and range from 1.1×10^8 to 2.5×10^9 and 5.3×10^9, respectively. (e) Polarisation-resolved plot of SERS intensity of fingerprint peak at 1,097 cm^{-1} with respect to rotation angle (θ).

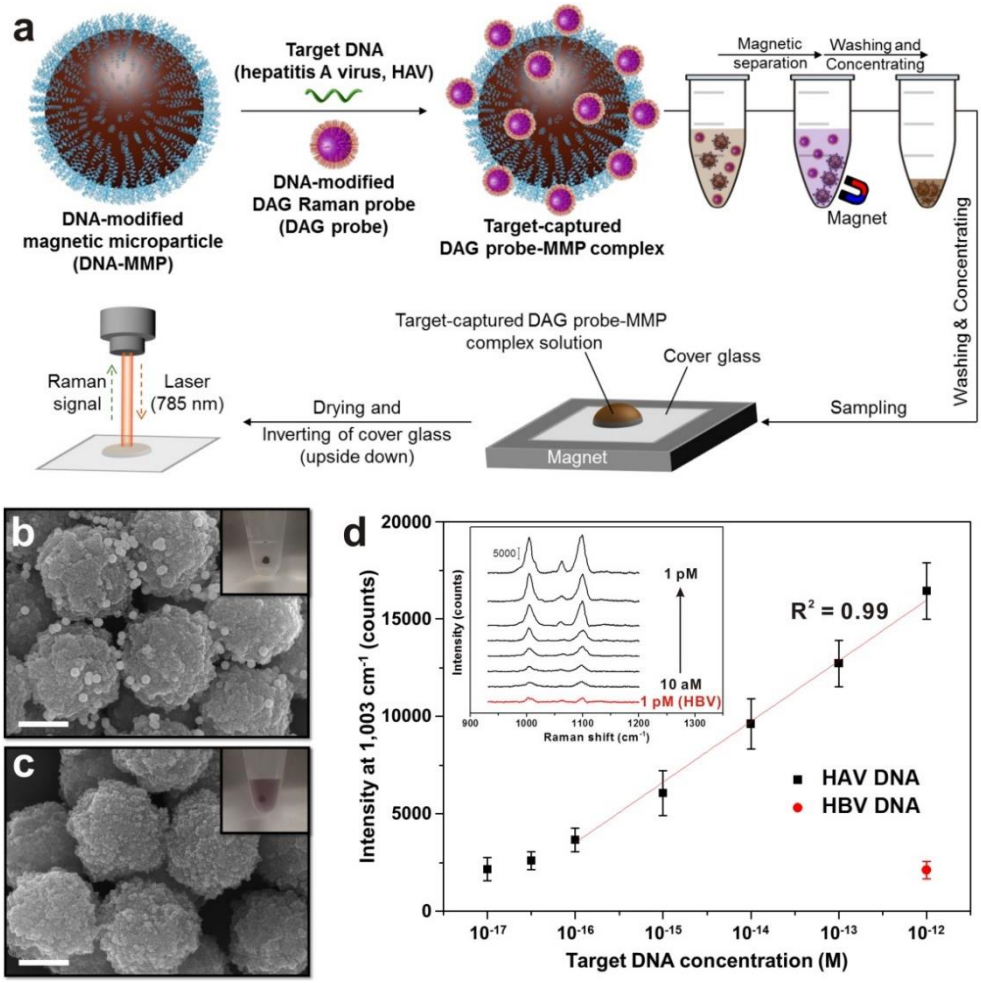

Figure 3.14. SERS-based ultrasensitive DNA detection assays using surface-functionalised DAG NPs. (a) Schematic illustration of mechanism of SERS-based ultrasensitive DNA detection assays. Complete procedure for detection of target DNA strands was conducted using typical sandwich-hybridisation assay. (b, c) SEM images of target-DNA-specific sandwich hybridisation complexes (target-captured DAG probe-MMP complexes) formed using different linker DNA: (b) complementary sequence DNA (HAV), (c) non-complementary sequence DNA (HBV). Inset: colour of assay solution under external magnetic field after DNA sandwich hybridisation. Scale bar is 500 nm. (d) Plot of SERS intensities at 1,003 cm^{-1} for different DNA concentrations of HAV (10 aM to 1 pM) and HBV (1 pM). Inset: Change in SERS spectra obtained using different concentrations of target

DNA strands. All spectra were obtained using 785-nm excitation laser at laser power of 2 mW and acquisition time of 5 s; SERS intensities were obtained by consecutive accumulation of five measurements.

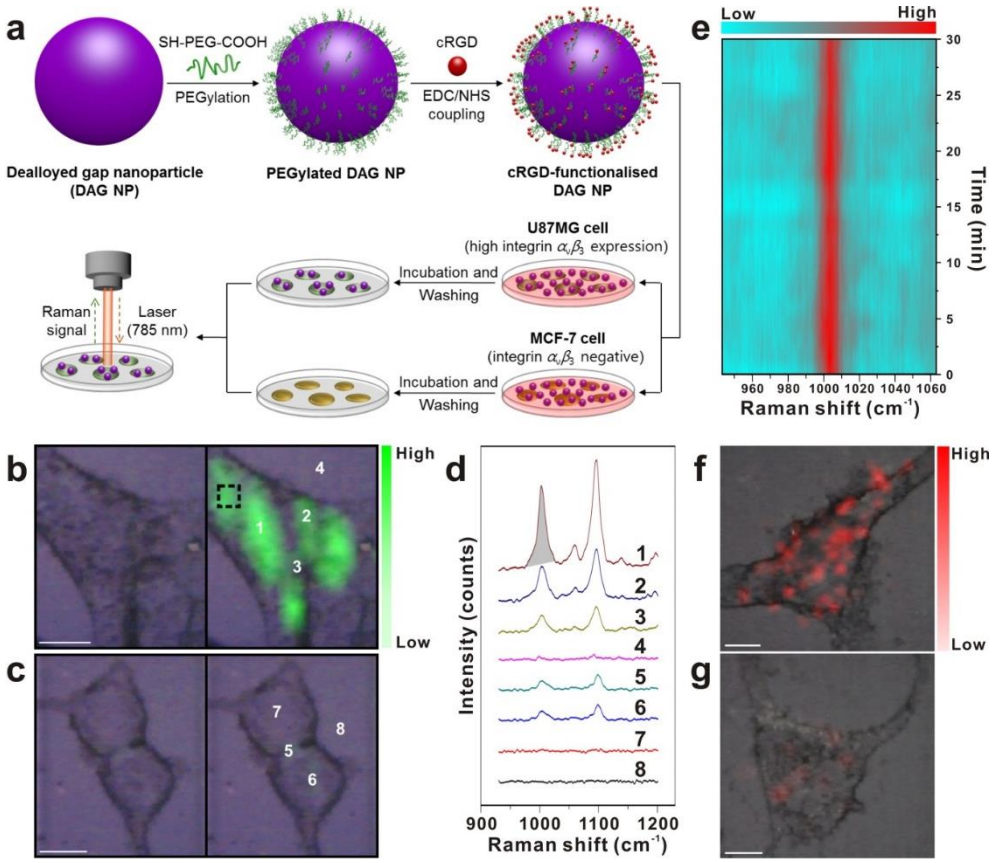

Figure 3.15. SERS-based target (integrin $\alpha_v\beta_3$)-specific cell imaging using surface-functionalised DAG NPs. (a) Schematic illustration of mechanism of SERS-based target-specific cell imaging. (b, c) Bright-field microscopy images (left) and SERS maps (right) of U87MG cells (b, high integrin $\alpha_v\beta_3$ expression) and MCF-7 cells (c, integrin $\alpha_v\beta_3$ negative) incubated with cRGD-functionalised DAG NPs. Scale bar is 10 μm. SERS intensity at each mapping pixel (2 μm × 2 μm) was integrated for SERS spectra ranging from 983 cm^{-1} to 1,023 cm^{-1} indicated by shaded region in (d) and colour-scaled for cell imaging. All spectra were obtained using 785-nm excitation laser at laser power of 4 mW and acquisition time of 1 s. (d) SERS spectra obtained from the positions marked in (b) and (c). (e) Time-dependent Raman profiles of cRGD-functionalised DAG NPs measured at the black dotted box in (b). (f, g) SERS maps of U87MG cells incubated with cRGD-functionalised different imaging probes: (f) DAG NPs, (g) AuNPs (average diameter of 80 nm).

Scale bar is 10 μm. SERS intensity at each mapping pixel (2 μm × 2 μm) was integrated for SERS spectra ranging from 983 cm^{-1} to 1,023 cm^{-1} and colour-scaled for cell imaging. All spectra were obtained using 633-nm excitation laser at laser power of 400 μW and acquisition time of 1 s.

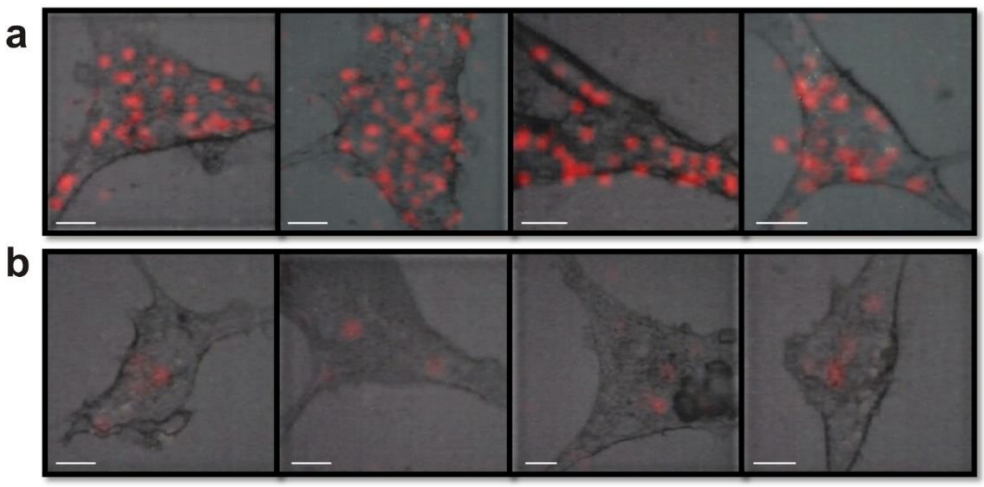

Figure 3.16. SERS maps of U87MG cells incubated with cRGD-functionalised different imaging probes: (a) DAG NPs, (b) AuNPs (average diameter of 80 nm). Scale bar is 10 μm. SERS intensity at each mapping pixel (2 μm × 2 μm) was integrated for SERS spectra ranging from 983 cm^{-1} to 1,023 cm^{-1} and colour-scaled for cell imaging. All spectra were obtained using 633-nm excitation laser at laser power of 400 μW and acquisition time of 1 s.

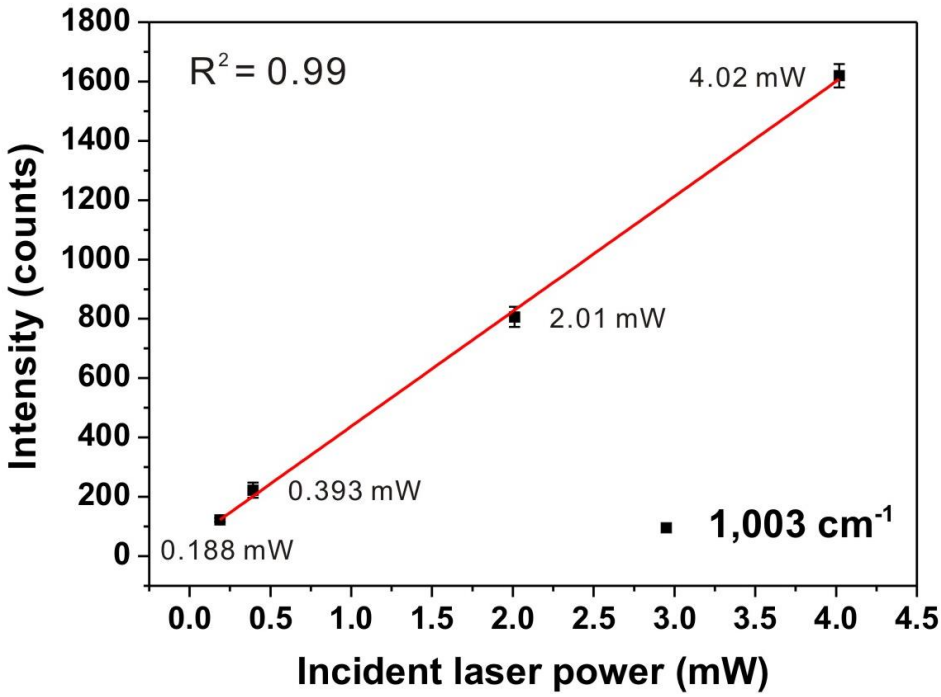

Figure 3.17. Incident-laser-power-dependent Raman intensities of 4-MPy (4-mercaptopyridine) solution. Raman intensity of fingerprint peak at 1,003 cm^{-1} is plotted as function of incident laser power. All Raman spectra were acquired with 633-nm laser through objective lens (20×, NA = 0.4) using exposure time of 30 s. The same 4-MPy concentration (200 mM) was used for all measurements.

Table 3.1. Atomic compositions of shell regions of as-synthesized nanoparticles (CAS, DAG, and gap-less AuNPs).

	Au (at%)†	Ag (at%)†
Amount of metal precursor added during synthesis‡	75.0	25.0
CAS NPs	77.2	22.8
DAG NPs	91.4	8.6
Gap-less AuNPs	100	0

†Atomic composition was estimated by EDX elemental mapping.

‡Different volumes of metal precursor (Au = 150 μL, Ag = 50 μL) were used for synthesis of alloy shell.

요약 (국문초록)

탈합금화 반응 기반의 다공성 나노입자 및 플라즈모닉 나노갭 나노입자 합성과 이의 촉매/광학 특성

나노미터 수준 크기(10–100 nm)의 인대(ligament) 구조가 3 차원으로 서로 연결된 다공성 금속 구조는 부피 대비 높은 표면적 및 뛰어난 표면 반응성에 의해 촉매, 센싱(sensing) 등으로의 응용에 있어서 매우 유망한 재료이다. 특히, 다공성 금 나노구조는 화학적/생물학적 안정성, 기계적 강도, 전기 전도성 및 높은 내부식성 등의 우수한 특성으로 인해 여러 산업 분야에서 많은 주목을 받고 있다. 기존에는, 상(phase) 분리 된 블록 공중합체(block copolymers), 콜로이드 결정(colloidal crystal), 자기 조립 계면 활성제(self-assembled surfactants) 및 생물학적으로 형성된 다공성 골격 구조(biologically formed porous skeletal structures) 등에 주조(casting)하는 방법으로 다공성 구조체를 제조하였다. 최근 나노기술이 발전함에 따라, 합금(alloy) 시스템으로부터 덜 안정한 금속 원소를 선택적으로 용해시키는 탈합금(dealloying) 반응이 금속 재료의 다공성 나노구조를 잘 제어 할 수 있는 제조 기술로 많이 사용되고 있다. 현재까지, 많은 이론적 및 실험적 연구를

통해 다공성 금속 구조는 여러 가지 변수에 의해 그 모양이 잘 제어되었으며, 구조 변화에 따른 특성의 변화 역시 많이 연구되었다.

고품질의 다공성 금속 구조를 제조하기 위해 다양한 연구와 기술이 최근까지도 꾸준하게 보고 및 개발되고 있지만, 대부분의 다공성 금속 구조는 주로 나노의학, 약물 전달, 바이오센싱(biosensing) 등의 응용에 제약이 있는 3 차원 및 2 차원 구조에 초점이 맞추어졌다. 반면, 나노입자 형태의 다공성 금속 구조는 많은 양의 약물 및 표적 분자를 부착(loading) 할 수 있는 넓은 표면 및 광학 센싱 신호를 증폭 시킬 수 있는 독특한 표면 플라즈몬 공명(surface plasmon resonance) 특성으로 인해 바이오의학(biomedicine) 및 센싱 분야에 있어서 유용하게 사용 가능하다. 또한, 다공성 금속 나노입자는 비교적 쉽고 빠르게 합성이 가능하고 대량 생산이 가능하기 때문에 실질적인 응용에 있어서 적합한 재료이다. 하지만, 합금을 형성하는 금속 재료들은 서로 상이한 화학적 특성을 가지고 있기 때문에 탈합금에 용이하도록 균일하게 합금 나노입자를 형성하는 것은 매우 어렵다. 물론, 다공성 금 나노입자를 합성하는 방법에 관한 소수의 연구가 보고되었지만, 해당 연구에서는 합금 금속 나노입자를 합성함에 있어서 복잡한 실험 단계가 필요하고, 합성 된 나노입자의 모양 및 크기가 불균일하여 재현성과 신뢰성이 요구되는 센싱 분야에 있어서 적합하지 않다. 이러한 측면에서, 다공성 금속 (특히, 금 재료) 나노입자를 균일한 크기로 재현성 있게 합성하는 기술은 여전히 풀어야 하는 과제이다.

본 학위논문에서는, 다공성 나노입자 및 플라즈모닉 나노갭 나노입자를 합성하는 탈합금 반응 기반의 합성 전략과 함께, 합성한 나노입자들의 촉매 활성도 및 광학 특성을 분석하였다. 합금 껍질 구조(alloy

shell structure)를 합성하는 과정에서, 금(Au) 과 은(Ag)의 양을 조절함에 따라 각 원자들의 분포를 다양하게 조절 할 수 있었으며, 서로 다른 조성의 합금 껍질 구조를 탈합금 함으로써 나노기공의 분포 및 내부 갭 구조를 다양하게 조절 할 수 있었다. 또한, 합성된 다공성 나노입자 및 플라즈모닉 나노갭 나노입자가 뛰어난 촉매 특성 및 광학 특성을 보이는 것을 실험적으로 확인하였으며, 핵산 검지 및 세포 이미징 등에 대한 응용성을 제시하였다. 탈합금 반응 기반의 나노구조의 변화와 이에 따른 촉매/광학 특성의 상관관계를 이해하는 것은, 목표하는 응용에 있어서 적합한 나노구조체를 디자인하고 합성하는데 크게 기여할 수 있을 것이다.

제 1 장에서는, 탈합금 반응을 통한 다공성 금속 나노구조체의 합성 및 응용에 관한 총론을 소개하였다. 금-은 합금 시스템으로부터 탈합금 반응을 통해 다공성 구조가 형성되는 과정을 소개하였으며, 탈합금 반응에 있어서 각종 변수들 (합금 조성, 탈합금 시간, 온도, 용액 및 금속 물질의 종류 등)이 다공성 나노구조체의 구조에 어떠한 영향을 미치는 지를 제시하였다. 또한, 여러 가지 형태의 다공성 금 나노구조체의 보고된 예시 및 다공성 금 나노구조체를 이용한 대표적인 응용에 관한 내용을 소개하고 분석하였다.

제 2 장에서는, 금/금-은 코어/쉘 나노입자(Au/Au-Ag core/alloy shell nanoparticle)에서 탈합금 반응을 통하여 선택적으로 은을 제거함으로써 금 코어/다공성 쉘 나노입자(Au core/porous shell nanoparticle)를 합성하는 전략을 제시하였다. 금 코어/다공성 쉘 나노입자에서 다공성 쉘 구조는 화학적 반응성이 높은 표면 결함(defect)을 가지는 얇은 금속 인대 구조로 구성되어 있었으며, 다량의 나노기공이 나노입자에 존재하였다. 금 코어/다공성 쉘 나노입자를 이용하여 촉매 활성도를 확인해 본 바, 금 코어/다공성 쉘

나노입자는 표면 반응성이 아주 높은 얇은 인대 구조로 인해 우수한 촉매 활성도를 보였으며, 플라즈모닉 구조체의 광열효과(photothermal effect)에 의해 촉매 활성도를 추가적으로 향상 시킬 수 있었다.

제 3 장에서는, 금/금-은 코어/쉘 나노입자(Au/Au-Ag core/alloy shell nanoparticle)에서 탈합금 반응을 통하여 선택적으로 은을 제거함으로써 탈합금 된 나노갭 나노입자(dealloyed nanogap nanoparticle)를 합성하는 전략을 제시하였다. 탈합금 반응에 의해 나노입자 내부에 형성된, 약 2 나노미터 크기의 나노갭 구조는 핵산, 실리카(silica) 및 고분자(polymer) 층이 없더라도 고수율로 합성되었다. 또한, 내부갭(interior nanogap)에서 발생하는 강한 전자기장 증폭 효과로 인하여 내부갭 나노입자는 강하면서도 정량성 및 재현성 있는 표면증강라만산란 신호를 발생 시킬 수 있었다. 특히, 단일 입자 수준에서 내부갭 나노입자의 표면증강라만산란 신호를 분석함으로써, 레이저의 폴라리제이션(polarization)과 무관하게 균일한 신호를 발생 시키는 것을 확인하였다. 아울러, 내부갭 나노입자 표면에 핵산 검지용 올리고뉴클레오타이드(oligonucleotide)를 도입함으로써 타겟 핵산(hepatitis A virus)을 초고감도로 정량적으로 검지하였으며, 또한 인테그린($\alpha_v\beta_3$ integrin)과 특이적으로 결합하는 단백질(cyclo(Arg-Gly-Asp-D-Phe-Lys))을 내부갭 나노입자 표면에 도입하여 선택적으로 타겟 세포(U87MG)를 이미징 하였다.

주요어: 탈합금, 다공성 금 나노 구조, 촉매 반응, 플라즈모닉 내부 갭 구조, 표면증강라만산란, 핵산 검지, 세포 이미징.

학번: 2011-30099